NEW INSIGHTS INTO THE BASIS OF NEUROGENESIS DEFECTS IN KABUKI SYNDROME

by

Giovanni A. Carosso

A dissertation submitted to Johns Hopkins University in conformity with the requirements for the degree of Doctor of Philosophy

Baltimore, Maryland

November 2019

ABSTRACT

Chromatin modifiers act to coordinate gene expression critical to neuronal differentiation from neural stem/progenitor cells (NSPCs). Loss-of-function variants in genes encoding two such enzymes, lysine-specific methyltransferase 2D (KMT2D) and lysine-specific demethylase 6A (KDM6A/UTX) cause the congenital, multisystem intellectual disability (ID) disorder Kabuki syndrome (KS1 and KS2, respectively). A mouse model of KS1, *Kmt2d*$^{+/\beta geo}$, demonstrated visuospatial memory impairments and decreased adult hippocampal neurogenesis in the dentate gyrus (DG). These were reversible upon post-natal treatment by histone deacetylase inhibition (HDACi), but underlying cellular and molecular mechanisms are poorly understood. Here, we moved forward with 3 hypotheses: (1) a dietary alternative may provide a more tolerable therapeutic avenue for chromatin opening in KS, (2) gene expression studies in KMT2D-deficient neuronal cells would yield novel insights into the pathogenesis of KS, and (3) comparison of phenotypes and gene expression abnormalities in KS1 and KS2 could yield a deeper understanding of the molecular mechanisms causing KS-associated ID. We describe the generation and characterization of multiple novel models of KS1 in human and mouse systems. Specifically, I report cell-autonomous defects in proliferation, cell cycle, and survival, accompanied by precocious NSPC maturation in several KMT2D-deficient model systems. Transcriptional suppression in KMT2D-deficient cells produced strong perturbation of hypoxia-responsive metabolism pathways. Functional experiments confirmed abnormalities of cellular hypoxia responses in KMT2D-deficient neural cells, and accelerated NSPC maturation in vivo. These findings support a model in which loss of KMT2D function suppresses expression of oxygen-responsive gene programs that are important to neural progenitor maintenance; this causes precocious neuronal differentiation in a mouse model of KS1. Then characterizing a KS2 mouse model, *Kdm6a*^{tm1d}, I found defects of adult hippocampal neurogenesis, cell cycle, and other phenotypes, that suggest shared etiologic mechanisms in KS2 and KS1.

This work is the first to identify the specific cellular and molecular defects that occur with loss-of-function of *KMT2D* and *KDM6A* in neural model systems. Furthermore, we identify cellular energy metabolism pathways as a critical molecular target in KS-related gene expression alterations, providing novel insights that could inform the treatment of KS.

READERS

Hans Tomas Bjornsson, M.D., Ph.D., Barbara Migeon, M.D.

THESIS ADVISOR

Hans Tomas Bjornsson, M.D., Ph.D.

THESIS COMMITTEE

Hal Dietz, M.D. (Chair), Hans Tomas Bjornsson M.D., Ph.D., David Valle, M.D., Loyal Goff, Ph.D., Winston Timp, Ph.D., Hongjun Song, Ph.D.

PREFACE

Acknowledgements

To begin, I thank my Ph.D. advisor, Hans Bjornsson. It has been a privilege to be entrusted with an exceptional degree of intellectual independence, and to benefit from the helpful guidance Hans encouragingly offers. All members of the Bjornsson Lab and our collaborators have been key to the progress of this work, especially Kasper Hansen, Leandros Boukas, Li Zhang, Joel Benjamin, Genay Pilarowski, Teresa Luperchio, and Jill Fahrner.

The opportunity to complete scientific training at the Johns Hopkins School of Medicine is an asset for which I will be forever grateful. I thank the Predoctoral Training Program in Human Genetics and Molecular Biology, its director David Valle, Sandy Muscelli, and especially Kirby Smith and Barbara Migeon for their generous leadership, advice, and support. The continued advice of my thesis committee members has been pivotal to my learning, and I deeply thank Loyal Goff, Winston Timp, David Valle, and in particular my thesis committee chair, Hal Dietz, whose exceedingly generous time was indispensable in shaping my thinking. Additionally, I thank Andy Feinberg for allowing me an early rotation in the Center for Epigenetics and his valuable mentorship with regard to grant writing. Finally, I thank my classmates in Human Genetics whose friendship brought welcome encouragement throughout this time.

Above all, I am most grateful and fortunate to count on the unconditional love and support of my family and friends, near and far, who have been integral to getting me on, and back on, my feet to where I am today. You know who you are.

TABLE OF CONTENTS

FIGURES

Chapter 2

Chapter 4

Chapter 5

CHAPTER 1: INTRODUCTION

Introduction

Kabuki syndrome and the Mendelian disorders of epigenetic machinery

Intellectual disability (ID) affects an estimated 1.5-2% of the world population (Vissers et al. 2016; Ervin and Merrick 2014; Leonard and Wen 2002), manifesting clinically as deficits in social, academic, and occupational functioning that collectively represent a substantial personal and economic burden across the globe (Ervin and Merrick 2014). Because ID is thought to result from developmental perturbations in the central nervous system, it has largely been considered an incurable condition not amenable to postnatal therapies. In addition to environmental exposures, genetic perturbations are increasingly recognized as causative factors in a substantial portion of intellectual disability. Indeed, the advent of genomic microarrays and high-throughput sequencing has increased the diagnosis of moderate to severe ID from 9-16.5% in the 1990s, to well above 55% in 2014 (Vissers et al. 2016). Among the ID genes implicated from gene identification studies, the genes for the epigenetic machinery (EM) are noteworthy because their functions are ongoing throughout life and therefore any perturbations may be reversible. Furthermore, this implicates dynamic mechanisms that control epigenetic states including histone modifications, chromatin remodeling, and DNA methylation in the etiology of ID. The Mendelian disorders of epigenetic machinery (MDEM) are caused by variants in genes encoding so-called writers, readers, erasers, and remodelers of chromatin-associated epigenetic marks (Bjornsson 2015). The inevitable intellectual disability caused by EM gene variants suggests that the correct placement and maintenance of these marks is critical to proper development and maintenance of cellular identities. The reversible, and sometimes redundant, nature of EM functions raises the possibility that certain forms of genetically caused ID may indeed be treatable postnatally, yet the therapeutic targets remains elusive due to the genetic heterogeneity in ID-associated MDEMs, Furthermore, that these disorders uniformly lead to intellectual disability suggests that the study of this rapidly emerging cause of intellectual disability

could tell us about the role of epigenetics in maintaining normal intellect. Thus, the study of the Mendelian disorders of the epigenetic machinery offers a unique opportunity to develop therapeutic strategies for intellectual disability.

Variants in genes encoding two chromatin modifiers, lysine-specific methyltransferase 2D (KMT2D) and lysine-specific demethylase 6A (KDM6A/UTX), cause the congenital, multi-system ID disorder Kabuki syndrome (KS1 and KS2, respectively) (Ng et al. 2010; Miyake et al. 2013; Lederer et al. 2012). KMT2D, a major H3K4 methyltransferase, works by catalyzing the deposition of open chromatin marks (H3K4me1/2/3), while KDM6A works by removing closed the chromatin mark (H3K27me3). Thus, we predict that phenotypes arising from the loss of either KMT2D (KS1) or KDM6A (KS2) are caused by promoting a closed chromatin state, thereby inhibiting the expression of critical genes. Indeed, KS1 and KS2 are clinically indistinguishable. Disruptions of *Kmt2d* or *Kdm6a* induced in mouse models reflect the cognitive deficits seen clinically in KS patients (Bjornsson et al. 2014; Tang et al. 2017). However, how these genetically dissimilar mechanisms lead to similar cognitive phenotypes remains obscure.

Previously, our laboratory identified defects of visuospatial memory and adult neurogenesis in a mouse model of KS1, $Kmt2d^{+/\beta_{geo}}$, and demonstrated rescue of these phenotypes via histone deacetylase inhibition (HDACi) using small molecule interventions (Bjornsson et al. 2014). That neurogenesis still occurs in the adult suggests that it may be a lifelong process, capable of regeneration. This supports the possibility of postnatal therapies in KS, but due to the correlative nature of earlier studies, it is clear that the cellular and molecular mechanisms driving KS-associated ID in neural contexts need further interrogation.

Adult neurogenesis in the hippocampus

The continual generation of adult-born neurons from neural stem/progenitor cells (NSPCs), and their integration into existing neural circuitry, is evidence that the most potent force in lifelong plasticity in the mammalian brain is adult neurogenesis, which occurs selectively in two major neurogenic niches: 1) Adult NSPCs in the subventricular zone (SVZ) migrate along the rostral migratory stream (RMS) toward the olfactory bulb (OB) as they mature into neurons, supporting adaptive olfactory learning throughout life (Doetsch et al. 1999), and 2) Adult NSPCs in the subgranular zone (SGZ) of the hippocampal dentate gyrus (DG) migrate only a short distance as they mature into granule cell (GC) neurons and join existing circuits in the DG granule cell layer (GCL), where they serve to promote the acquisition of visuospatial memory and adaptive learning via the process of pattern separation (Gonçalves et al. 2016). Although some studies disagree on the extent of adult hippocampal neurogenesis (AHN) in humans (Sorrells et al. 2018), recent studies firmly establish human AHN as an important component of healthy cognitive functions, that lessens in rate during aging and is aberrantly reduced in mild cognitive impairment and Alzheimer's disease (Moreno-Jiménez et al. 2019; Tobin et al. 2019). Of particular interest to our group, given the findings of disrupted adult neurogenesis, was a recent study showing decreases in the volume of grey matter in the DG of KS patients (Boisgontier et al. 2018), bolstering the findings of DG defects in KS models (Bjornsson et al. 2014). Similarly, neurobehavioral testing of KS1 patients identifies impairments of visuospatial discrimination, which function was previously linked to the DG (Garthe and Kempermann 2013). Together, these studies suggest the need for deep phenotyping of neurodevelopmental models to identify KMT2D- and KDM6A-dependent functions, including the use of human cell models to determine the translational potential of our findings.

In the adult SGZ, quiescent radial glia-like cells (qRGLs) can be activated (aRGLs) by mitotic entry, giving rise first to intermediate progenitor cells (IPCs), then to neuroblasts (NBs) that mature into dentate granule cell (DGC) neurons. Recently born adult DGCs show heightened

synaptic connectivity and hyper-excitability (Ge et al. 2007) that are critical to context encoding and pattern separation (Sahay et al. 2011; Danielson et al. 2016; Zhuo et al. 2016), and can be targeted to enhance memory precision through rejuvenation of the DGC population (McAvoy et al. 2016). Thus, the length of time spent by adult-born DGCs in immature stages may directly impact DG memory functions. Proper adult hippocampal neurogenesis (AHN) requires a delicate balance between NSPC self-renewal, proliferation, and neuronal differentiation, to ensure it can support DG functions while maintaining an adequate supply of quiescent NSPCs in the SGZ. An array of cell-intrinsic and extrinsic niche factors influences this balance throughout life. Mounting evidence links chromatin dynamics in NSPCs, as well as metabolic rewiring of carbon metabolism (Zheng et al. 2016) and hypoxic states in the DG (Mazumdar et al. 2010; Chatzi et al. 2015), to cell-intrinsic regulation of NSPC maintenance, but causal relationships among epigenetic machinery, metabolic states, and neuronal development require further investigation.

Strategy

To understand whether KS is a clinically treatable form of ID, we first evaluate the possibility of phenotypic rescue by dietary intervention (Chapter 2). We demonstrate rescue of behavioral and functional defects associated with AHN. Next, we perform in-depth analysis of gene expression and developmental phenotypes in several models of KS1 (Chapter 3), finding mechanistic links between cell-autonomous defects and transcriptional abnormalities in KMT2D-deficient cells. Importantly, we describe the phenotypic concordance between mouse and human-derived neuronal models. We then characterize a KS2 mouse model to compare neurogenesis in KS1 and KS2 (Chapter 4). Finally, we suggest promising avenues in KS neurodevelopment research (Chapter 5), and conclude with the relevance to and potential impact of these studies for bettering the lives of KS patients (Chapter 6).

CHAPTER 2: A KETOGENIC DIET RESCUES HIPPOCAMPAL MEMORY DEFECTS IN A MOUSE MODEL OF KABUKI SYNDROME

Adapted from:

Benjamin, J.S., Pilarowski, G.O., **Carosso, G.A.**, Zhang, L., Huso, D.L., Goff, L.A., Vernon, H.J., Hansen, K.D. and Bjornsson, H.T., 2017. A ketogenic diet rescues hippocampal memory defects in a mouse model of Kabuki syndrome. *Proceedings of the National Academy of Sciences*, *114*(1), pp.125-130.

Abstract

Kabuki syndrome is a Mendelian intellectual disability syndrome caused by mutations in either of two genes (*KMT2D* and *KDM6A*) involved in chromatin accessibility. We previously showed that an agent that promotes chromatin opening, the histone deacetylase inhibitor (HDACi) AR-42, ameliorates the deficiency of adult neurogenesis in the granule cell layer of the dentate gyrus and rescues hippocampal memory defects in a mouse model of Kabuki syndrome (*Kmt2d*$^{+/\beta Geo}$). Unlike a drug, a dietary intervention could be quickly transitioned to the clinic. Therefore, we have explored whether treatment with a ketogenic diet could lead to a similar rescue through increased amounts of beta-hydroxybutyrate, an endogenous HDACi. Here, we report that a ketogenic diet in *Kmt2d*$^{+/\beta Geo}$ mice modulates H3ac and H3K4me3 in the granule cell layer, with concomitant rescue of both the neurogenesis defect and hippocampal memory abnormalities seen in *Kmt2d*$^{+/\beta Geo}$ mice; similar effects on neurogenesis were observed on exogenous administration of beta-hydroxybutyrate. These data suggest that dietary modulation of epigenetic modifications through elevation of beta-hydroxybutyrate may provide a feasible strategy to treat the intellectual disability seen in Kabuki syndrome and related disorders.

Introduction

Kabuki syndrome [KS; Mendelian Inheritance in Man (MIM) 147920, 300867] is a monogenic disorder, the manifestations of which include intellectual disability, postnatal growth retardation, immunological dysfunction, and characteristic facial features. Mutations in either lysine (K)-specific methyltransferase 2D (*KMT2D*) or lysine (K)-specific demethylase 6A (*KDM6A*) are known to lead to KS (Ng et al. 2010; Lederer et al. 2012; Miyake et al. 2013). Interestingly, each of these genes plays an independent role in chromatin opening, a process essential for transcription, as *KMT2D* encodes a lysine methyltransferase that adds a mark associated with open chromatin

(histone 3, lysine 4 trimethylation; H3K4me3), whereas *KDM6A* encodes a histone demethylase that removes a mark associated with closed chromatin (histone 3, lysine 27 trimethylation; H3K27me3). If a deficiency of chromatin opening plays a role in KS pathogenesis, agents that promote open chromatin states, such as histone deacetylase inhibitors (HDACis), could ameliorate ongoing disease progression.

Previously, in a mouse model of KS (*Kmt2d*$^{+/\beta Geo}$), we observed a deficiency of adult neurogenesis, a dynamic process during adult life (Ming and Song 2011), in association with hippocampal memory deficits (Bjornsson et al. 2014). After 2 wk of treatment with the HDACi AR-42, an antineoplastic agent, we observed normalization of these phenotypes (Bjornsson et al. 2014) (Fig. S1). However, transitioning an antineoplastic drug to patients with a nonlethal intellectual disability disorder may prove problematic. Recently, beta-hydroxybutyrate (BHB), a ketone body that is the natural end product of hepatic fatty acid beta oxidation, has been shown to have HDACi activity (Shimazu et al. 2013). Because BHB is actively transported into the central nervous system during ketosis (Hasselbalch et al. 1995), and furthermore has been shown to directly enter the hippocampus (Sleiman et al. 2016), it should be readily available to modulate histone modifications in relevant cells (neurons); this would be expected to ameliorate the deficiency of adult neurogenesis in *Kmt2d*$^{+/\beta Geo}$ mice. A dietary intervention could be quickly transitioned to the clinic and is unlikely to have major adverse effects.

Here, we demonstrate that treatment with a ketogenic diet (KD) for 2 wk normalizes the global histone modification state and corrects the deficiency of neurogenesis seen in the granule cell layer (GCL) of the dentate gyrus (DG). This dietary change also rescues the hippocampal memory defects in *Kmt2d*$^{+/\beta Geo}$ mice. Furthermore, administration of exogenous BHB also rescues the neurogenesis defect in *Kmt2d*$^{+/\beta Geo}$ mice, suggesting that the increased levels of BHB play a major role in the observed therapeutic effect of the KD. Our data show that some of the neurological effects of

a debilitating germline mutation can be offset by dietary modification of the epigenome and suggest a mechanistic basis of the KD, a widely used therapeutic strategy in clinical medicine.

Results

Phenotype of the *Kmt2d*$^{+/\beta Geo}$ Mice.

Our mouse model of KS (*Kmt2d*$^{+/\beta Geo}$) demonstrates many features seen in patients with this disorder, including similar craniofacial abnormalities (Bjornsson et al. 2014) and postnatal growth retardation (Fig. 1*A*). In addition, *Kmt2d*$^{+/\beta Geo}$ mice demonstrate a deficiency of adult neurogenesis (Fig. 1*B*), as well as hippocampal memory defects (Fig. 1*C*). All these features are observed in both mixed and congenic C57BL/6J (Fig. 1 *A*–*C*) backgrounds (>10 generations). Hippocampal gene expression profiling in *Kmt2d*$^{+/\beta Geo}$ and *Kmt2d*$^{+/+}$ littermates using microarrays reveals that differentially expressed genes tend to be down-regulated in *Kmt2d*$^{+/\beta Geo}$ compared with in *Kmt2d*$^{+/+}$ littermates, as would be expected, as the Kmt2d enzyme promotes transcriptional expression. Specifically, we find that 18 of 24 significantly differentially expressed probe-sets [false discovery rate (FDR) < 10%; n = 6–7 mice per group] are down-regulated in *Kmt2d*$^{+/\beta Geo}$ mice (Fig. 1*D*). This shift toward down-regulation in *Kmt2d*$^{+/\beta Geo}$ mice is also present in the top 1,000 genes ranked by fold change (FC) (64% are down-regulated; $P < 2.2e{-}16$; Fig. S2). However, gene-specific changes in *Kmt2d*$^{+/\beta Geo}$ mice are relatively subtle: Only 52 genes have an absolute $\log_2$ FC larger than 0.5. Note that *Kmt2d* itself shows the most highly significantly differentially expressed probe-set (Fig. 1*D*). As expected, the site of hybridization for the particular *Kmt2d* probe-set that shows differential expression between genotypes covers the mRNA that is missing in the *Kmt2d*$^{+/\beta Geo}$ mice (Fig. S3).

In Vitro and in Vivo Elevation of BHB.

According to the reported histone deacetylase inhibitory activity of BHB (Shimazu et al. 2013), we hypothesized that BHB could be used as a therapy for KS (Fig. S4), given the interdependence of histone acetylation and H3K4me3 (Lee et al. 2006). First, we confirmed that BHB had HDACi activity. Using an in vitro epigenetic reporter allele assay to quantify the activity of the H3K4me3 and H4ac machinery in HEK293 cells (Bjornsson et al. 2014), we observed a dose-dependent increase of reporter activity with increasing amounts of BHB (Fig. 2*A*). To increase BHB levels in vivo, we placed *Kmt2d*$^{+/\beta Geo}$ and *Kmt2d*$^{+/+}$ mice on a KD, using a regimen frequently used in human treatment (4:1 fat to protein ratio) (Freeman et al. 1998). We observed a significant increase in urine BHB from KD-treated mice compared with their regular diet-treated counterparts (Fig. 2*B*); this effect was greatly accentuated in *Kmt2d*$^{+/\beta Geo}$ animals compared to *Kmt2d*$^{+/+}$ littermates (Fig. 2*C*). Elevation of BHB was also observed in serum and brain tissue of *Kmt2d*$^{+/\beta Geo}$ mice in response to the KD (Fig. S5). Although structural renal abnormalities are common in patients with KS, renal function is usually normal (Courcet et al. 2013), and *Kmt2d*$^{+/\beta Geo}$ mice also have normal renal function (Fig. S6). In contrast, levels of acetoacetate (AcAc) did not show a corresponding elevation, leading to an increased BHB/AcAc ratio in the KD-treated *Kmt2d*$^{+/\beta Geo}$ mice, indicating a disproportionate increase in BHB compared with KD-treated *Kmt2d*$^{+/+}$ littermates (Fig. 2*D*). This increase in the BHB/AcAc ratio was not observed in a mouse model of Rubinstein-Taybi syndrome (CREB-binding protein, *Crebbp*$^{+/-}$; (Kung et al. 2000) (MIM 180849, 613684; Fig. 2*D* and Fig. S7), another genetically imposed deficiency of open chromatin marks (Alarcón et al. 2004), suggesting that the metabolic alterations in our *Kmt2d*$^{+/\beta Geo}$ mice are unlikely to be secondary to a general loss of open chromatin modifications (Kurdistani 2014; Castonguay et al. 2014). The ratio of BHB to AcAc is governed by the cellular NADH/NAD$^+$ ratio (Fig. 2*E*). Serum lactate/pyruvate ratio is also sensitive to the NADH/NAD$^+$ ratio (Fig. S8*A*), and is concordantly skewed in *Kmt2d*$^{+/\beta Geo}$ mice on a KD (Fig. 2*E* and Fig. S8*B*). Taken together, our data suggest that an underlying alteration in the

NADH/NAD^+ ratio may potentiate a therapeutic strategy for KS based on enhanced BHB production in response to a KD.

In Vivo Rescue of Global Histone and Gene Expression Abnormalities.

We next explored the effects of in vivo treatment on global chromatin states in the GCL of the DG after 2 wk of a KD. *Kmt2d*$^{+/\beta Geo}$ mice on the KD for 2 wk had increased levels of H3K4me3 compared to *Kmt2d*$^{+/\beta Geo}$ mice on a standard diet (Fig. 3 *A* and *B*). In addition, *Kmt2d*$^{+/\beta Geo}$ mice on the KD for 2 wk also showed global normalization of H3ac levels in the GCL of the DG (Fig. 3 *C* and *D*). Because of the ability of KD treatment to increase marks of open chromatin in vivo, we next assessed the effects of treatment on the 5 genes that showed the most significant down-regulation in the hippocampus of *Kmt2d*$^{+/\beta Geo}$ mice. As expected, the mRNA encoding *Kmt2d* did not increase in *Kmt2d*$^{+/\beta Geo}$ mice on a KD, as the low expression was based on structural allele disruption (Fig. 3*E*). In contrast, 3 of the 4 other genes we assayed showed a significant increase in transcript expression in response to a KD, with 2 showing full normalization (Fig. 3*F*). One of these, Glucagon-like peptide-1 receptor (*Glp1r*), encodes a protein localized to neuronal synapses. As in the *Kmt2d*$^{+/\beta Geo}$ mice, *Glp1r*-targeted animals show reversible hippocampal memory defects (During et al. 2003).

The KD Rescues Neurogenesis Defects in *Kmt2d*$^{+/\beta Geo}$ Mice.

We next assessed the effect of the KD on neurogenesis by two independent markers: quantification of either 5-ethynyl-2'-deoxyuridine–positive (EdU^+) or doublecortin-positive (DCX^+) cells in the GCL of the DG. Counting EdU^+ cells directly after injection is informative regarding any proliferative defects of this cellular niche. In contrast, this metric reflects abnormalities in neuronal survival when estimated after a 30-d delay. We counted the number of EdU^+ cells in the GCL both

immediately after a course of EdU injections or 30 d later; both measures showed a significant increase in *Kmt2d*$^{+/\beta Geo}$ mice on the KD compared with *Kmt2d*$^{+/\beta Geo}$ mice on a regular diet (Fig. 4*A*). Upon quantification of the DCX^{+} fraction of the GCL (a marker of adult neurogenesis we had previously shown was decreased in *Kmt2d*$^{+/\beta Geo}$ mice), we found a significant increase in *Kmt2d*$^{+/\beta Geo}$ mice on the KD compared with mice on a standard diet, with no significant difference compared with KD-treated wild-type (*Kmt2d*$^{+/+}$) littermates (Fig. 4 *B* and *C*).

Exogenous BHB Rescues the Neurogenesis Defect in *Kmt2d*$^{+/\beta Geo}$ Mice.

To determine the sufficiency of BHB to rescue the neurogenesis defect in *Kmt2d*$^{+/\beta Geo}$ mice, we treated mice with exogenous BHB. A once-daily i.p. injection of 5 mM/kg/d BHB for 2 wk led to peak urine levels of BHB comparable to levels seen in mice on the KD (Fig. S9*A*); however, given the short half-life of BHB (1–2 h) (Clarke et al. 2012), the overall daily exposure to BHB after a single injection was much less than with the KD (Fig. S9*B*). Despite this, BHB injections led to a significant increase in EdU^{+} cells in the GCL of the DG (Fig. S9*C*), although not to the same magnitude as in the mice on a KD for 2 wk (Fig. 4*A*). As a consequence, to approximate the BHB exposure during a KD, we used a combination strategy with delivery of BHB by osmotic pump (Fig. S9*D*) plus three daily IP injections (5 mM/kg BHB) for 2 wk; this strategy achieved daily BHB exposure comparable to KD treatment (Fig. S9*E*) and resulted in a significant increase in neurogenesis, as measured by the number of EdU^{+} cells in the GCL of the DG in *Kmt2d*$^{+/\beta Geo}$ compared with vehicle-treated *Kmt2d*$^{+/\beta Geo}$ mice (Fig. S9*F*), which closely mirrored the neurogenesis proliferation rescue seen after treatment with the KD (Fig. 4*A*). Similarly, a quantification of DCX^{+} cells in the GCL showed a dose-dependent normalization with full recovery at the higher dose level (Fig. S9 *G* and *H*).

A KD Rescues Hippocampal Memory Defects in *Kmt2d*$^{+/\beta Geo}$ Mice.

Finally, we asked whether KD treatment would rescue the hippocampal memory defects seen in *Kmt2d*$^{+/\beta Geo}$ mice. The probe trial of a Morris water maze (MWM) assay is a measure previously shown to be particularly sensitive for detecting a disruption of adult neurogenesis (Garthe and Kempermann 2013). We previously demonstrated deficiencies in MWM performance for *Kmt2d*$^{+/\beta Geo}$ mice (Fig. 1*C*). After 2 wk of KD treatment, *Kmt2d*$^{+/\beta Geo}$ mice showed a significant increase in the number of platform zone crossings (Fig. 4*D*) compared with untreated *Kmt2d*$^{+/\beta Geo}$ mice.

Discussion

Although BHB has previously been shown to have HDACi activity (Shimazu et al. 2013; Lim et al. 2011), the potential for therapeutic application remains speculative. Here, we show that therapeutically relevant levels of BHB are achieved with a KD modeled on protocols that are used and sustainable in humans. In addition, we demonstrate a therapeutic rescue of disease markers in a genetic disorder by taking advantage of the BHB elevation that accompanies the KD.

Our findings that exogenous BHB treatment lead to similar effects on neurogenesis as the KD support the hypothesis that BHB contributes significantly to the therapeutic effect. In our previous study (Bjornsson et al. 2014), the HDACi AR-42 led to improved performance in the probe trial of the MWM for both *Kmt2d*$^{+/\beta Geo}$ and *Kmt2d*$^{+/+}$ mice (genotype-independent improvement). In contrast, KD treatment only led to improvement in *Kmt2d*$^{+/\beta Geo}$ mice (genotype-dependent improvement). This discrepancy may relate to the fact that AR-42 acts as an HDACi but also affects the expression of histone demethylases (Huang et al. 2011), resulting in increased potency but less specificity. Alternatively, because the levels of BHB appear to be higher in *Kmt2d*$^{+/\beta Geo}$ mice on the

KD, the physiological levels of BHB might be unable to reach levels in *Kmt2d*$^{+/+}$ mice high enough to make drastic changes on chromatin.

Although we cannot exclude a contribution from other biochemical actions of BHB such as direct butyrylation of histone tails (Chen et al. 2007) or the effects of BHB on mitochondrial respiration, synaptic physiology (Kim et al. 2010), or cellular oxidative stress (Shimazu et al. 2013), the concordance of therapeutic effects with those observed on administration of an HDACi (Bjornsson et al. 2014) provides strong, albeit correlative, evidence that the BHB acts, at least in part, through modulation of histone marks. The global epigenetic abnormalities seen in *Kmt2d*$^{+/\beta Geo}$ mice occur in association with altered expression of genes, some of which (such as *Glp1r*) lead to overlapping neurodevelopmental abnormalities when targeted in mice (During et al. 2003). Interestingly, *Glp1r* and several of the genes most highly differentially expressed demonstrate normalization on the KD. As with other disorders associated with primary perturbation of epigenetic factors, it is not possible to attribute specific aspects of the disease phenotype to specific genes or pathways; rather, it is likely that phenotypic consequences integrate the combined action of many genes that are dysregulated on attenuation of KMT2D function.

In addition to the effects seen on hippocampal function and morphology, we also uncovered a metabolic phenotype in *Kmt2d*$^{+/\beta Geo}$ mice, which leads to both increased BHB/AcAc and lactate/pyruvate ratios during ketosis; an increased NADH/NAD$^+$ ratio could explain both observations. This increased NADH/NAD$^+$ ratio may relate to a previously described propensity of *Kmt2d*$^{+/\beta Geo}$ mice toward biochemical processes predicted to produce NADH, including beta-oxidation, and a resistance to high-fat-diet–induced obesity (D.-H. Kim et al. 2015). If this exaggerated BHB elevation holds true in patients with KS, the KD may be a particularly effective treatment strategy for this patient population; however, this remains to be demonstrated. Alterations of the NADH/NAD$^+$ ratio could also affect chromatin structure through the action of sirtuins, a

class of HDACs that are known to be NAD^+ dependent. Advocates of individualized medicine have predicted therapeutic benefit of targeted dietary interventions, although currently there are few robust examples. This work serves as a proof-of-principle that dietary manipulation may be a feasible strategy for KS and suggests a possible mechanism of action of the previously observed therapeutic benefits of the KD for intractable seizure disorder.

Methods

Study Design.

The purpose of this study was to test the hypothesis that the KD could be used as a therapeutic strategy in a mouse model of KS. At least four biological replicates were used for each biochemical analysis. Data collection was performed for a predetermined period, as dictated by literature-based or core facility-based standards, and no exclusion criteria were applied. All analyses were performed by examiners blinded to genotype and/or treatment group. For drug treatments, mice were randomly assigned to treatment groups with approximately equivalent numbers in each group. In box and whisker plots, whiskers extend 1.5 times the interquartile range, as is the default in the R programming language; circles indicate data points outside this range. All data points were used in statistical analysis.

Mice and Dietary Manipulations.

Our mouse model, *Kmt2d*$^{+/\beta Geo}$, also known as *Mll2Gt*$^{(RRt024)Byg}$, was generated by BayGenomics through the insertion of a gene trap vector. The KD [4:1 (fat:protein) ratio, F6689 Rodent Diet, Ketogenic, Fat:Paste] paste was acquired from Bio-Serv. Mice were given 2 wk free (ad libitum) access to KD paste as a sole food source. Paste was replaced several times per week. During MWM testing, given the length of testing (more than a week), we treated for 3 wk. *Crebbp*$^{+/-}$, also known

as *Crebbp*^{tm1Dli} (Kung et al. 2000), mice were acquired from the Jackson laboratories. All mice used in these studies were between 1 and 2 mo of age unless otherwise noted. All experiments were performed on mice fully backcrossed to C57BL/6J background unless otherwise noted. All mouse experiments were performed in accordance with the NIH Guide for the Care and Use of Laboratory Animals and were approved by the Animal Care and Use Committee of Johns Hopkins University.

Serum and Brain BHB Analysis.

Serum and homogenized brain tissue from *Kmt2d*$^{+/\beta Geo}$ and *Kmt2d*$^{+/+}$ mice that had been treated with both standard diet and a KD for 2 wk was assayed for BHB levels using a BHB assay kit (MAK041; Sigma).

Serum Creatinine and Blood Urea Nitrogen Analysis.

Serum creatinine and blood urea nitrogen are commonly used markers of kidney function. Both creatinine and blood urea nitrogen levels were measured from serum from *Kmt2d*$^{+/\beta Geo}$ and *Kmt2d*$^{+/+}$ mice, using standard clinical assays run at the Johns Hopkins comparative medicine analysis core.

BHB Injection and Urine Assay.

Either 5 mM/kg (R)-(−)-3-hydroxybutyric acid sodium salt (Santa Cruz Biotechnology) or saline was injected (100 μL) intraperitoneally once or three times a day. (R)-(−)-3-Hydroxybutyric acid sodium salt becomes (R)-(−)-3-hydroxybutyric acid in the blood and can interconvert into BHB, the form measured by ketone assays. Therefore, in text and legends, we used BHB as the label for simplicity. Urine BHB was quantified by the β-hydroxybutyrate (Ketone Body) Colorimetric Assay Kit (Cayman Chemical Company). Urine from injected mice was collected ∼1.5–2 h after

injection. Urine from mice on the KD was taken in the early afternoon unless otherwise stated in the text.

Osmotic Pumps.

An Alzet (Durect Co.) microosmotic pump (model 1002) made to allow for 14 d of diffusion was filled (84-μL reservoir) with either 2.5 mg/mL (R)-(−)-3-hydroxybutyric acid sodium salt (Santa Cruz Biotechnology) in saline vehicle or saline vehicle alone. Mice were anesthetized, after which a small incision was made on the skin of the lower back and the pump was placed directly under the skin.

Reporter Alleles.

HEK 293 cells were transfected with lipofectamine LTX (Thermo Fisher) with either our H3K4me3 or H4ac reporter alleles that have been previously described (Bjornsson et al. 2014). We selected for and maintained stably transfected cells through positive selection with blasticidin at a dose of 10 mg/mL (Life Technologies). Blasticidin selection was stopped 24 h before exposure to BHB. For BHB treatment, (R)-(−)-3-hydroxybutyric acid sodium salt (Santa Cruz Biotechnology) was added to the medium 24 h before FACSVerse flow sorting (BD Sciences). Data were analyzed using FlowJo (Tree Star Inc.).

Serum Lactate and Pyruvate Analysis.

Serum was extracted from whole blood by centrifugation at 3,500 × *g* for 10 min after 1 h incubation at room temperature. Subsequently, the supernatant was removed and stored at −20 °C. Serum samples were then assayed for levels of lactate and pyruvate with the Lactate Assay Kit (Sigma Aldrich) and Pyruvate Assay Kit (Sigma Aldrich).

Mass Spectrometry for AcAc and BHB.

AcAc and BHB were prepared via acid extraction and BSTFA [*N*,*O*-bis(trimethylsilyl)trifluoroacetamide)] derivatization, and detected via gas chromatography–mass spectrometry. The mass spectrometer was set in SCAN mode to detect all mass fragments in a range of m/z 50–600. Compounds were identified on the basis of their characteristic retention time and ion peaks. Results were reported as a ratio of AcAc to BHB.

Microarray Experiment.

Microarray results are based on a joint analysis of two different experiments. Hippocampi were dissected from wild-type and *Kmt2d*$^{+/\beta Geo}$ mice on a standard diet. In the first experiment, four wild-type and three *Kmt2d*$^{+/\beta Geo}$ mice were profiled, and in the second experiment, three wild-type and three *Kmt2d*$^{+/\beta Geo}$ mice were profiled. RNA was extracted from whole hippocampi, using the Qiagen RNeasy kit or TRIzol reagents (Ambion Life Technologies), followed with DNase I treatment (Qiagen). For microarray, cDNA was synthesized by the JHMI High Throughput Biology Center, using the SuperScript II RT assay (Thermo Fisher) following recommended conditions, and hybridized to Affymetrix Mouse Gene 1.0 microarrays.

Analysis of Microarray Data.

The microarray data were preprocessed using the robust multi-array analysis method (Irizarry et al. 2003), as implemented in the oligo package (Carvahlo et al., 2010) from Bioconductor (Huber et al. 2015; Gentleman et al. 2004). Unwanted noise was removed using surrogate variable analysis (Leek and Storey 2007; Leek et al. 2012) with five surrogate variables. Only probe-sets of the "core" category were analyzed. After surrogate variable analysis, data were analyzed using the limma

package (Ritchie et al. 2015) with an empirical Bayes variance estimator method (Smyth), and *P* values were corrected for multiple testing, using the Benjamini-Hochberg procedure.

RT-qPCR Validation.

For RT-qPCR validation cDNA was synthesized using the Applied Biosciences High-Capacity cDNA Reverse Transcription Kit. RT-qPCR was done on RNA from the same mice used for microarray (n = 3–4 per group), as well as an additional second cohort treated in an identical fashion with a KD (n = 5–7 per group). The Taqman probes (Life Technologies) used were Pld5, Mm00620912_m1, Fam, S; Glp1r, Mm00445292_m1, Fam, S; Ankfn1: Mm03039417-m1, Fam, S; Kmt2d, Mm01717064-g1, Fam, S, with Pgk1 and Gapdh as controls (Mm99999915_g1, Vic; Mm00435617_m1, Vic, S). For Zic5, the available Taqman probe did not yield any data, so we designed and used a Sybr green assay (Zic5-F: 5'-GAGGCGCTTCCTAGTACTCC-'3; Zic5-R: 5'-GCTGCTATTGGCAAACTTCCTA-'3 with control gene Tfrc (Tfrc-F: 5'-GAGGCGCTTCCTAGTACTCC-'3; Tfrc-R: 5'-CTTGCCGAGCAAGGCTAAAC-'3). The two experimental groups were run and normalized to untreated wild-type and then combined for analysis.

Perfusion, Sectioning, and Staining.

Perfusion, cryosectioning, and immunofluorescence staining were performed as previously described (Bjornsson et al. 2014). EdU (Life Technologies) in PBS/6% (vol/vol) DMSO (10 mg/mL) injections (50 μg/g/d), were delivered either for 7 consecutive days, followed by immediate perfusion (proliferation), or 7 consecutive days of injection and then perfusion on the 30th day after the first injection (survival). For staining, every sixth brain section was used, and blocking was done with 5% (mass/vol) BSA. EdU was labeled with Click-iT EdU Alexa Fluor 488 Imaging Kit

(Thermo Fisher), as well as DAPI mounting with Vectamount (Vector Laboratories). EdU quantification was performed blinded to genotype and treatment. Labeled cells were counted in every sixth slice in the GCL of the DG, and average number per slice was calculated for each brain. Immunofluorescence was performed with the following primary antibodies: DCX (Santa Cruz Biotechnology; 1:200 goat), trimethylated H3K4 (Cell Signaling; 1:500 rabbit), acetylated H3K9, and H3K14 (Cell Signaling; 1:5,000 rabbit). Incubations were performed overnight at 4 °C in blocking buffer. Previous experiments performed on normal serum from which the antibodies were derived showed no nonspecific immunoreactivity (Bjornsson et al. 2014).

Confocal Microscopy.

Z-stack images were taken at either 10×, using Zeiss Axiovert 200 (Carl Zeiss), or 25×, using Zeiss AxioExaminer multiphoton (Carl Zeiss), with genotypes and treatment blinded to the researcher. Fluorescence intensity of the highlighted GCL layer at the midpoint of the z-stack was measured at 10× magnification, using the Zen software (Carl Zeiss). Fluorescence intensity of either the H3K4me3 or H3ac antibody was divided by the DAPI fluorescence intensity to normalize for cell numbers. For ease of interpretation, values were normalized to *Kmt2d*$^{+/+}$ levels. Group comparisons were done using a Student's *t* test, with significance set at $P < 0.05$.

DCX Area Measurement.

The DCX positive fraction of the GCL was measured by taking 4× pictures and using the Bezier tool on NS elements 2.0 software (Nikon) to measure the area of DCX$^+$ cells that expressed DCX, as well as the entire area of the GCL. The researcher was blinded to mouse genotype and treatment. The fraction of the GCL that showed DCX$^+$ cells was then calculated, and group differences were analyzed using a Student's *t* test with significance value set at $P < 0.05$.

Behavioral Testing.

Behavioral testing was conducted on mice between 1 and 2 mo of age and performed and analyzed blinded to genotype and treatment, with all experiments performed in the late morning or early afternoon. Each particular behavioral test was performed at a consistent time of day. For open-field testing, *Kmt2d*$^{+/+}$ and *Kmt2d*$^{+/\beta Geo}$ mice were placed individually in an open-field chamber (San Diego Instruments) for ten 180-s intervals. These intervals were combined to give an average activity level, and treatment and genotype groups were compared using a Student's *t* test with significance value set at $P < 0.05$. For grip strength, mice were allowed to grab onto the grip strength meter (Columbus Instruments) and were lightly pulled by the tail with increasing force until releasing their grip. This was repeated five times for each mouse, with the highest and lowest value being discarded. The remaining three values were then averaged. Average grip strength for treatment and genotype groups were compared with a Student's *t* test with significance value set at $P < 0.05$. For the MWM, all testing was performed in a standard 1.1-m diameter tank filled with room temperature water stained with white tempera paint (Crayola). The tank had a small platform submerged 2 cm below the water level in the middle of one of the four tank quadrants. For the first 3 d, the platform had a visible flag on top (flag training), and each mouse was placed in the tank for four consecutive 60-s trials in which they were trained to reach the visible platform. During each trial, the platform was moved to a different quadrant, but the mouse was always entered into the tank in the same location. Latency for each trial for each mouse was recorded, and if the mouse could not reach the platform in 60 s, they were placed on the platform. After flag training, the visible flag was removed, and for 5 d, mice were trained to reach the now hidden platform (hidden platform training), with four consecutive trials per mouse per day, with a maximum allotment of 60 s per trial. The platform was never moved, but each trial, the mouse was entered into a different quadrant, with the order of these

quadrants randomly assigned for each day. On the final day (probe trial), the platform was removed, the mice were allowed to swim for 90 s, and the number of crossings over the previous location of the platform was measured. For training and probe tests, data were recorded both manually and electronically, with ANY-maze software (San Diego Instruments). The four genotype and treatment groups were analyzed for differences, using a Student's *t* test during the probe trial and with repeated-measures ANOVA within-subjects test for the latencies.

Acknowledgements

We thank Dr. H. Dietz, Dr. B. Migeon, Dr. A. Chakravarti, Dr. P. Cole, and Dr. D. Valle for their many helpful suggestions. We thank Catherine Kiefe for her assistance with creating and editing Figs. S1 and andS4.S4. We also thank H. S. Cho for his work in the early stages of this project and Dr. J. A. Fahrner for her work on the latter stages of this project. Finally, we thank M. F. Kemper, R. J. Pawlosky, and R. L. Veech for advice regarding how to best measure BHB in brain. This work was supported by a National Institute of Health grant (to H.T.B.; Director's Early Independence Award, DP5OD017877) and a gift from the Benjamin family (no relation to the first author).

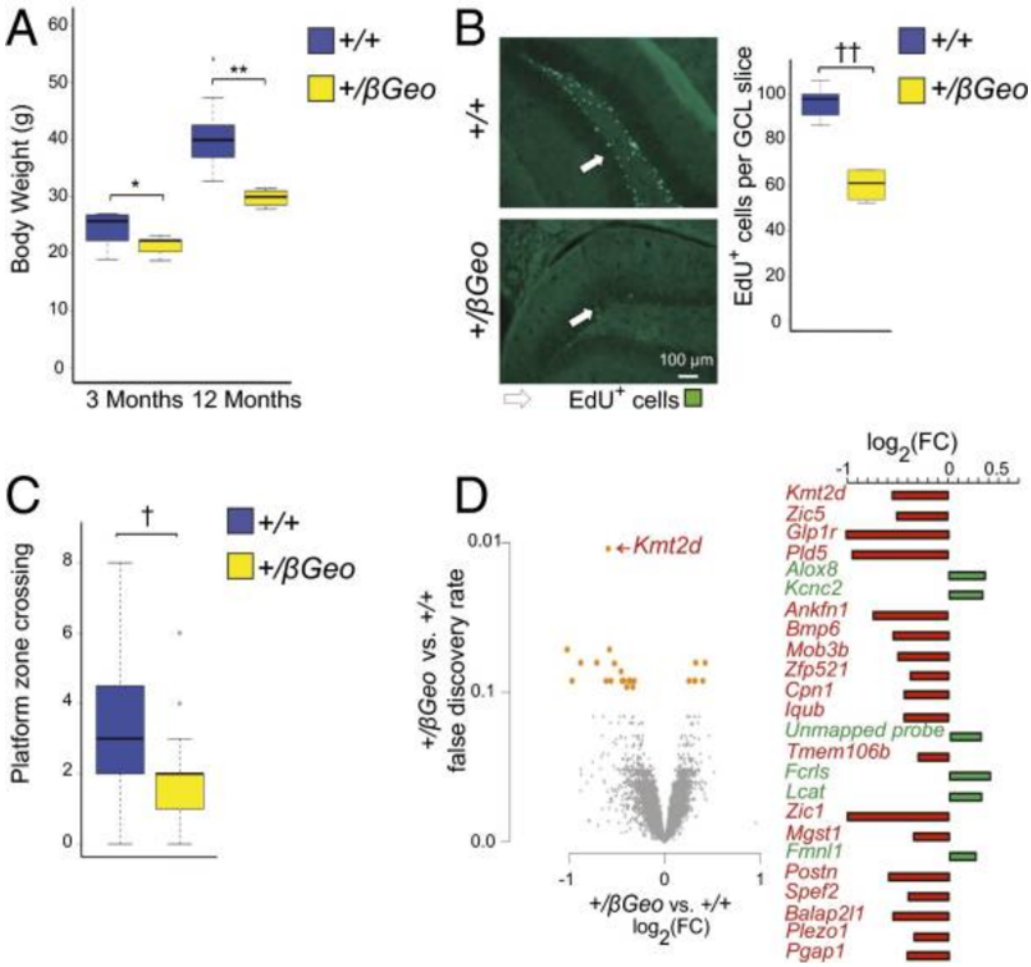

Figure 1. Phenotypes observed in fully backcrossed (C57BL/6J) *Kmt2d*$^{+/\beta Geo}$ mice. (*A*) *Kmt2d*$^{+/\beta Geo}$ mice weigh significantly less than age-matched *Kmt2d*$^{+/+}$ mice at 3 mo, and this weight difference becomes more pronounced at 12 mo (n = 4–10 per group, both sexes). (*B*) *Kmt2d*$^{+/\beta Geo}$ mice demonstrate significantly fewer ($P < 0.005$) EdU$^+$ cells in the GCL of the DG compared with *Kmt2d*$^{+/+}$ littermates, following an EdU proliferation staining assay (n = 4–7 per group). (*C*) *Kmt2d*$^{+/\beta Geo}$ mice (yellow) demonstrate a significant decrease ($P < 0.005$) in platform zone crosses during a MWM probe trial compared with *Kmt2d*$^{+/+}$ (blue) littermates (n = 23–27 per group). (*D*) Gene expression microarray from hippocampus reveals 18 significantly down-regulated probe-sets between *Kmt2d*$^{+/\beta Geo}$ and *Kmt2d*$^{+/+}$ littermates, as well as six that were significantly up-regulated (n = 6–7 per group; FDR < 10%). *$P < 0.05$; **$P < 0.01$; †$P < 0.005$; ††$P < 0.001$.

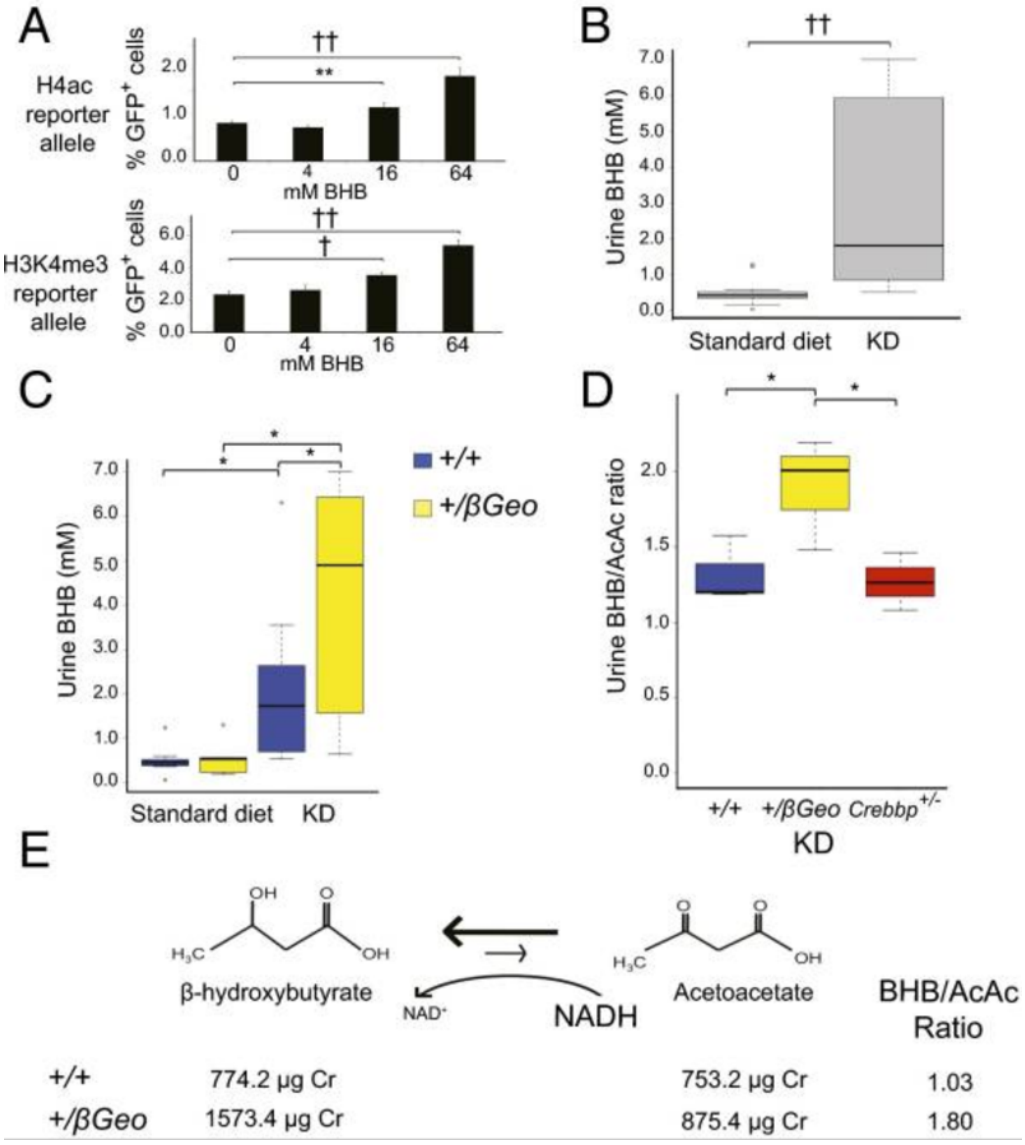

Figure 2. BHB is an endogenous histone deacetylase inhibitor that is elevated in *Kmt2d*$^{+/\beta Geo}$ mice on a KD. (*A*) Stably transfected HEK293 cells with either an H4ac or an H3K4me3 reporter allele both show a dose-dependent increase in fluorescence with increasing amounts of BHB in culture media (n = 5–7 replicates per condition). (*B*) Mice treated with the KD for 2 wk show a significant (P < 0.001) increase of urine BHB compared with standard diet–treated controls (n = 12–17 per group). (*C*) When separated by genotype, urine from KD-treated mice revealed significantly increased urine BHB levels (P < 0.05) in *Kmt2d*$^{+/\beta Geo}$ mice compared with *Kmt2d*$^{+/+}$ controls, suggesting *Kmt2d*$^{+/\beta Geo}$ mice are predisposed to preferentially increased BHB levels during ketosis (n = 4–12 per group). (*D*) GC-MS analysis confirmed this observation and revealed that this increase in BHB is in fact a result of an altered BHB/AcAc ratio, which is significantly elevated in KD-treated *Kmt2d*$^{+/\beta Geo}$ mice, but not *Crebbp*$^{+/-}$ mice, compared with controls (P = 0.38; n = 3 per group). (*E*) This schematic demonstrates how the BHB/AcAc ratio is controlled by the cellular NADH/NAD$^+$ ratio (47, 48), suggesting that *Kmt2d*$^{+/\beta Geo}$ and not *Crebbp*$^{+/-}$ mice maintain relatively higher NADH levels during ketosis (Figs. S7 and andS8).S8). *P < 0.05; **P < 0.01; $^{\dagger}P$ < 0.005; $^{\ddagger}P$ < 0.001.

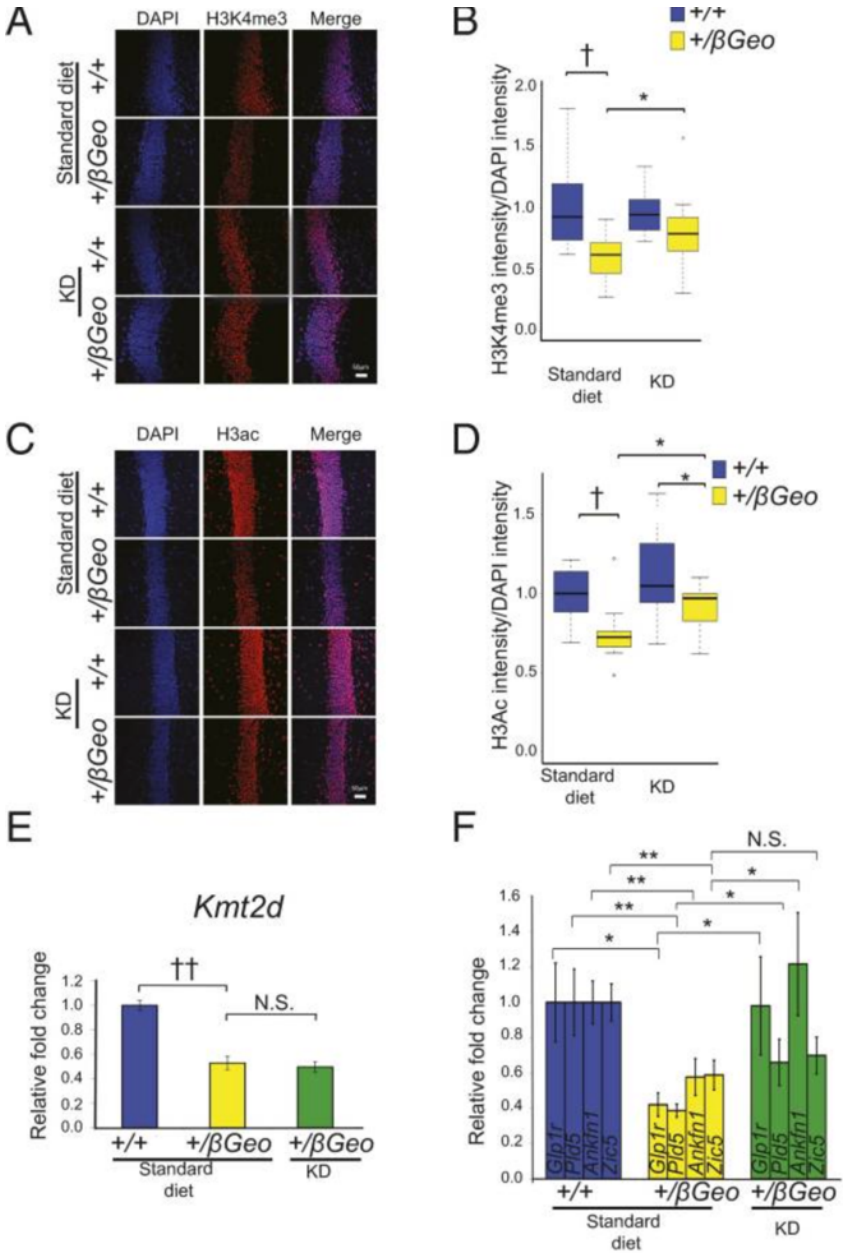

Figure 3. KD treatment promotes open chromatin in the hippocampus and rescues gene expression abnormalities in *Kmt2d*$^{+/\beta Geo}$ mice. (*A* and *B*) *Kmt2d*$^{+/\beta Geo}$ mice demonstrate a significantly ($P < 0.005$) decreased H3K4me3/DAPI fluorescence ratio in the GCL of the DG compared with *Kmt2d*$^{+/+}$ littermates on a standard diet. Upon 2 wk on the KD, there is a significant ($P < 0.05$) increase in the H3K4me3/DAPI fluorescence in *Kmt2d*$^{+/\beta Geo}$ mice and no significant difference ($P = 0.09$) between the two genotypes ($n = 10–12$ per group). (*C* and *D*) *Kmt2d*$^{+/\beta Geo}$ mice show a significant decrease ($P < 0.005$) in the H3ac/DAPI fluorescence ratio compared with *Kmt2d*$^{+/+}$ littermates; this ratio significantly increased ($P < 0.05$) in *Kmt2d*$^{+/\beta Geo}$ mice after 2 wk on the KD ($n = 11–14$ per group). (*E*) *Kmt2d* expression does not demonstrate any change on a KD treatment ($n = 9–11$ per group). (*F*) Validation of candidate genes by RT-qPCR confirming both the down-regulation as well as rescue on KD treatment ($n = 9–11$ per group). (Scale bar: 50 μm.) N.S., not significant, $P > 0.05$; *$P < 0.05$; **$P < 0.01$; †$P < 0.005$; ††$P < 0.001$.

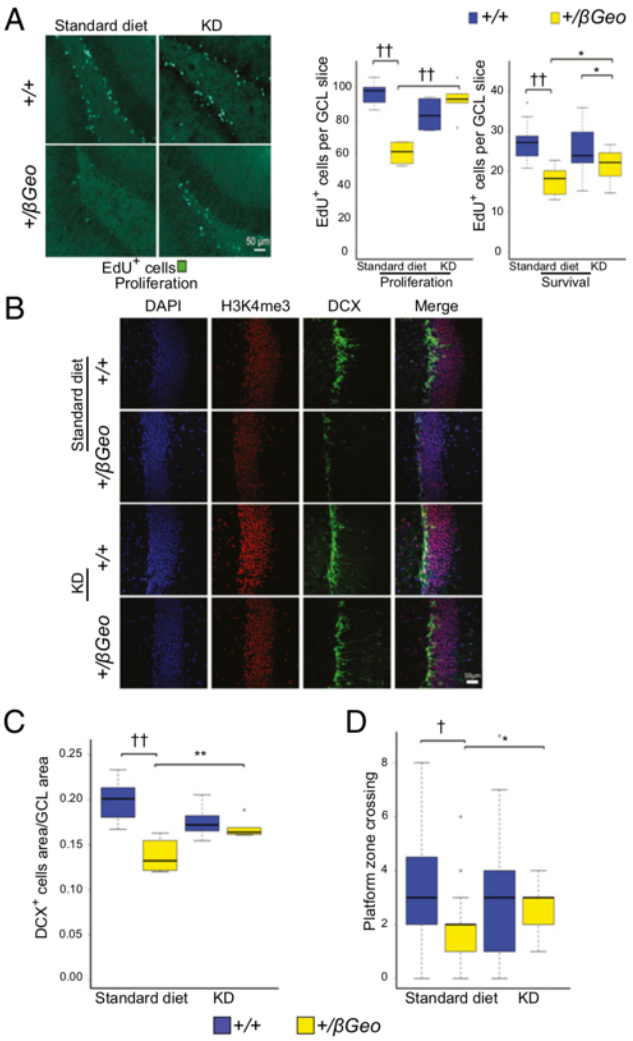

Figure 4. KD treatment rescues the neurogenesis and hippocampal memory defects in *Kmt2d*$^{+/\beta Geo}$ mice. (*A*) *Kmt2d*$^{+/\beta Geo}$ mice demonstrate significantly fewer EdU^{+} cells in the GCL of the DG, both immediately after 7 d of EdU injection (proliferation, $P < 0.001$) or 30 d after start of EdU injection (survival, $P < 0.001$). Both measures increase significantly ($P < 0.001$; $P < 0.05$) in *Kmt2d*$^{+/\beta Geo}$ mice on the KD for 2 wk (n = 5–9, proliferation; n = 8–15, survival). (*B* and *C*) *Kmt2d*$^{+/\beta Geo}$ mice on a standard diet demonstrate a significantly smaller DCX^{+} cell population in the GCL of the DG ($P < 0.001$) compared with *Kmt2d*$^{+/+}$ littermates. This ratio significantly increases ($P < 0.01$) in *Kmt2d*$^{+/\beta Geo}$ mice after 2 wk of a KD (n = 7–12 per group). (*D*) The number of platform crossings during the probe trial portion of the MWM increased significantly ($P < 0.05$) in *Kmt2d*$^{+/\beta Geo}$ mice on the KD compared with a standard diet. Compared with KD-treated *Kmt2d*$^{+/+}$ mice, KD-treated *Kmt2d*$^{+/\beta Geo}$ mice showed no significant difference in platform crossings ($P = 0.239$; n = 19–32 per group). *Kmt2d*$^{+/\beta Geo}$ mice also took longer to reach the platform during the 5-d hidden platform testing of the MWM compared with *Kmt2d*$^{+/+}$ controls (increased escape latency); however, KD treatment did not appear to have a significant effect, as assayed by repeated-measures ANOVA (Fig. S10*A*). Flag testing showed no significant differences between treatment or genotype for platform latency (Fig. S10*B*). Further control tests for strength, activity, and anxiety-like behaviors (grip strength and open field testing) were unaffected by the genotype (Fig. S10 *C* and *D*). $^{*}P < 0.05$; $^{**}P < 0.01$; $^{\dagger}P < 0.005$; $^{\ddagger}P < 0.001$. (Scale bar: 50 μm.)

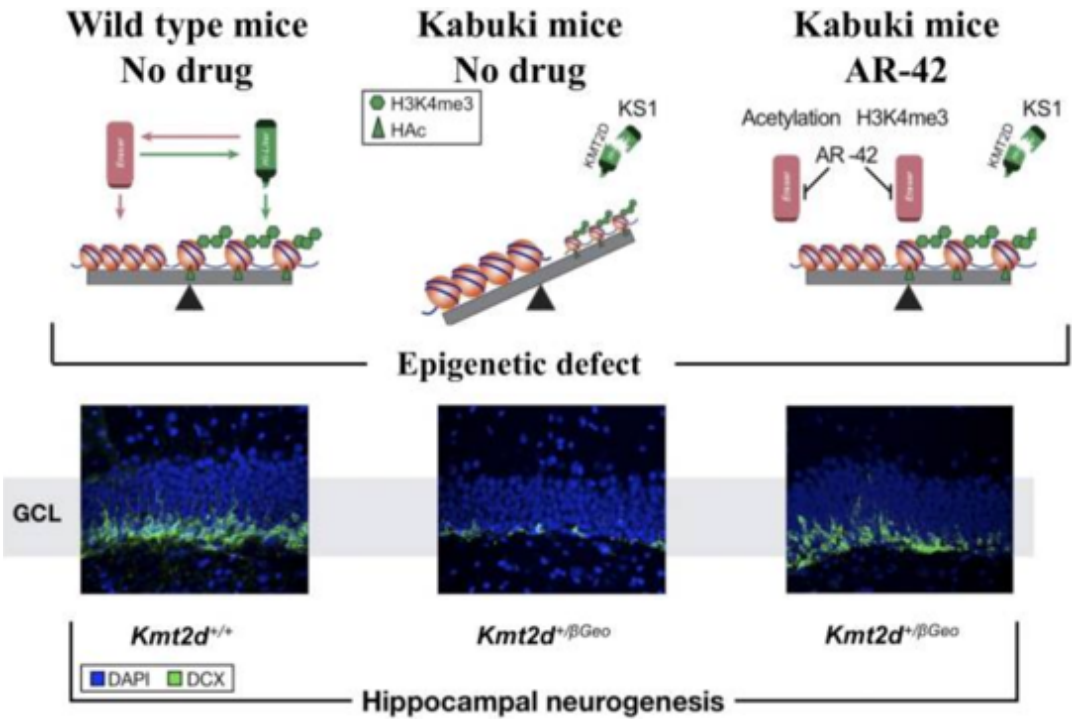

Supplementary Figure 1. Schematic summary of prior findings. *Kmt2d*$^{+/\beta Geo}$ mice on a mixed C57BL/6J and 129SvEv background demonstrated a global deficiency of the open chromatin mark H3K4me3 in association with decreased neurogenesis in the GCL of the DG (*Middle*) compared with littermate *Kmt2d*$^{+/+}$ mice (*Left*). These defects were rescued with AR-42 (*Right*) (6), a class 1 and 2 histone deacetylase inhibitor (24), which has recently been shown to inhibit HDAC5 in liver cells (49).

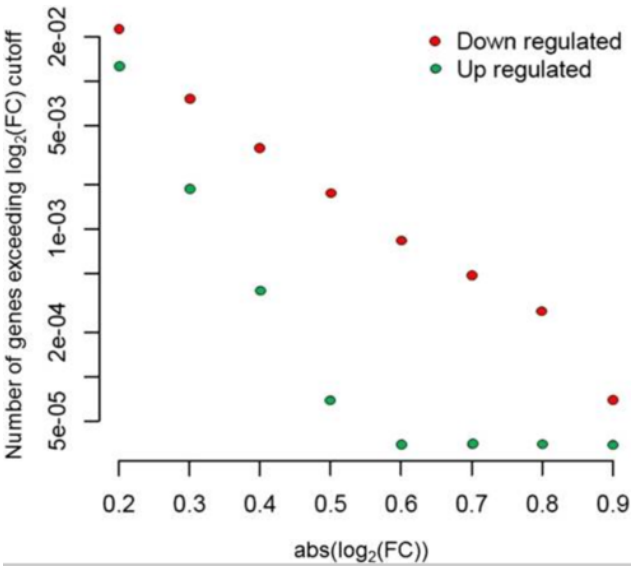

Supplementary Figure 2. *Kmt2d*$^{+/\beta Geo}$ mice demonstrate a generalized tendency toward down-regulation of gene expression. Even when data were explored below the level of statistical significance for the top 1,000 most highly expressed genes and put into bins, there was a generalized tendency toward down-regulation of gene expression at all fold change (FC) bins (n = 6 per group).

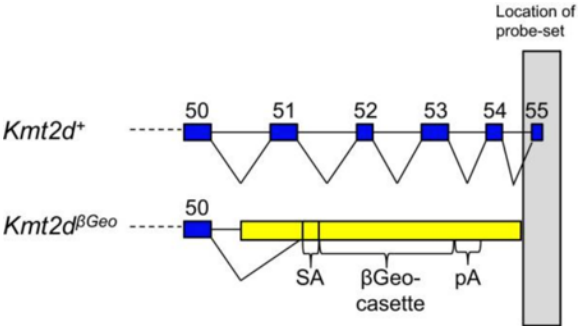

Supplementary Figure 3. The *Kmt2d* probe-set that shows differential expression from microarray analysis is downstream of the SET domain. Schematic of the probe-set that overlaps the last exon of *Kmt2d*.

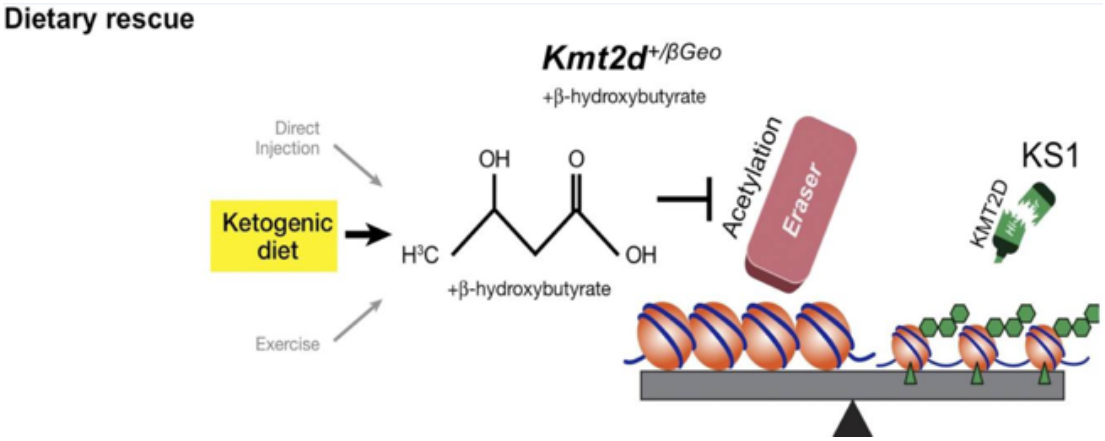

Supplementary Figure 4. The rationale describing how a KD could be used to counter the epigenetic defect in *Kmt2d*$^{+/\beta Geo}$ mice. There are multiple ways to increase blood levels of BHB (direct injection, KD, and exercise). Because BHB is an endogenous HDACi, it may rescue the epigenetic abnormality seen in *Kmt2d*$^{+/\beta Geo}$ mice, and thereby provide similar therapeutic benefits as AR-42 in *Kmt2d*$^{+/\beta Geo}$ mice (Fig. S1).

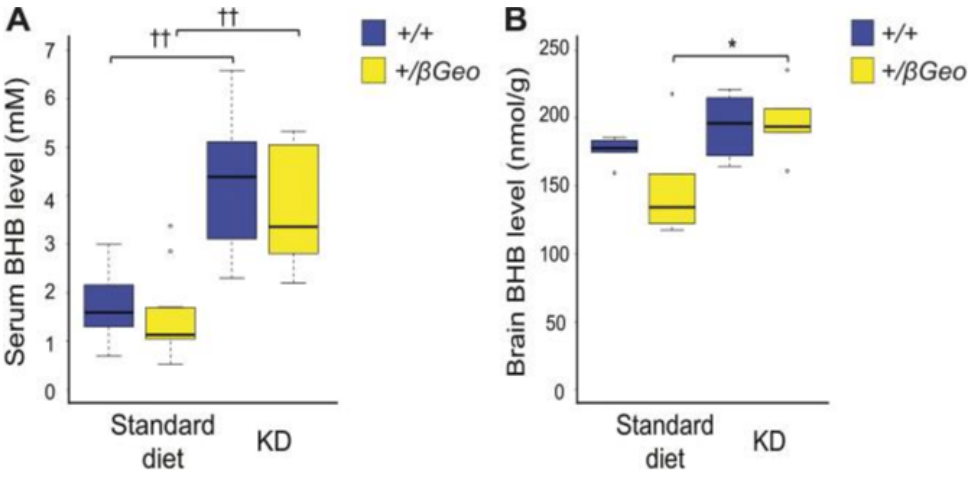

Supplementary Figure 5. BHB is elevated in the serum and brain of *Kmt2d*$^{+/\beta Geo}$ mice on a KD. (*A*) Serum BHB levels in *Kmt2d*$^{+/\beta Geo}$ mice ($n > 10$) and littermate controls ($n > 10$) after 2 wk of the KD. (*B*) Brain BHB levels in *Kmt2d*$^{+/\beta Geo}$ mice ($n \geq 5$) and littermate controls ($n \geq 5$) after 2 wk of the KD. $^{*}P < 0.05$; $^{\dagger\dagger}P < 0.001$.

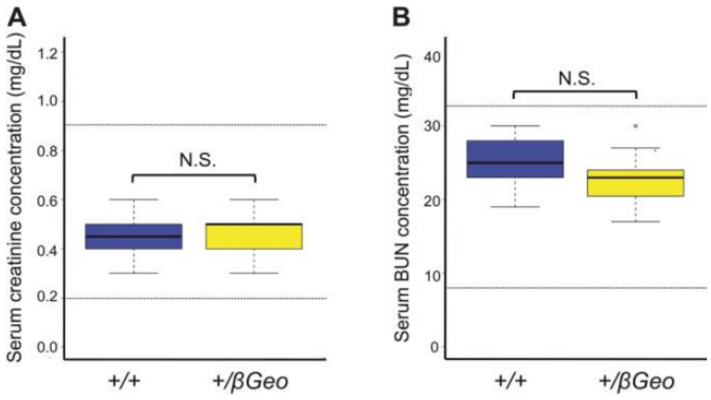

Supplementary Figure 6. Two markers of renal function are normal in *Kmt2d*$^{+/\beta Geo}$ mice. (*A*) Creatinine levels in young mice (6 wk old) do not show a significant difference (Welch's *t* test) between *Kmt2d*$^{+/\beta Geo}$ mice (n = 11) and littermate *Kmt2d*$^{+/+}$ mice (n = 14), and all values are within the range of normal levels for mice of this age (dotted lines). (*B*) Blood urea nitrogen (BUN) levels show no significant difference (Welch's *t* test) between *Kmt2d*$^{+/\beta Geo}$ mice (n = 11) and littermate *Kmt2d*$^{+/+}$ mice (n = 14), and all values are within the range of normal levels for mice (dotted lines). N.S., not significant, $P > 0.05$.

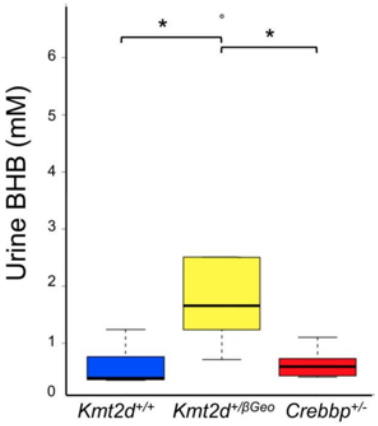

Supplementary Figure 7. *Crebbp*$^{+/-}$ mice do not share metabolic alterations found in *Kmt2d*$^{+/\beta Geo}$ mice. Rubinstein-Taybi syndrome is another Mendelian disorder of the epigenetic machinery, caused by deficiency of a histone acetyltransferase (CREBBP), which secondarily leads to a global deficiency of histone acetylation (14). The histone tails have previously been suggested to act as a potential acetyl-CoA sink (15). Furthermore, other studies have linked NAD^+ and histone acetylation (16). A global deficiency of histone acetylation could therefore potentially lead to chronic acetyl-CoA elevation, thereby driving beta-oxidation and secondarily increasing NADH/NAD^+ ratio in both KS and Rubinstein-Taybi syndrome. BHB levels from urine show a significant ($P < 0.05$) elevation in *Kmt2d*$^{+/\beta Geo}$ mice compared with *Kmt2d*$^{+/+}$ and *Crebbp*$^{+/-}$ mice (13) (n = 6–8 per group). However, no significant differences were seen between *Kmt2d*$^{+/+}$ and *Crebbp*$^{+/-}$ mice ($P = 0.36$). *$P <$ 0.05.

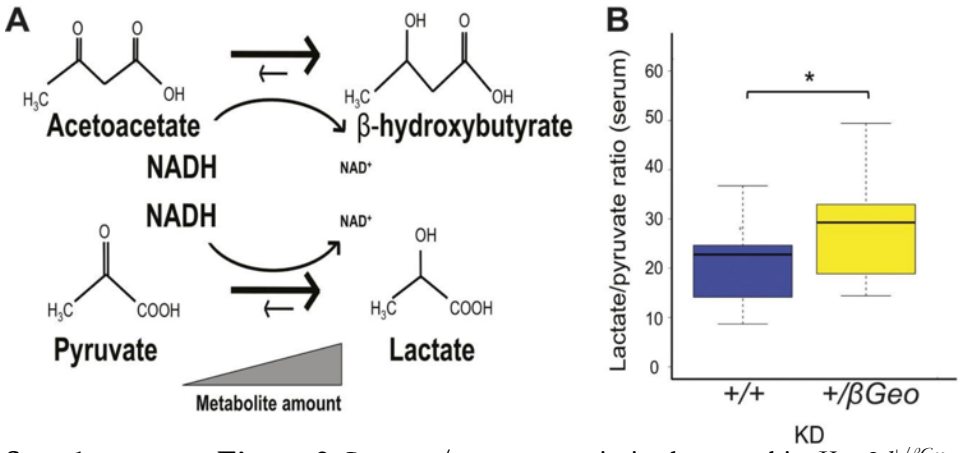

Supplementary Figure 8. Lactate/pyruvate ratio is abnormal in *Kmt2d*$^{+/\beta Geo}$ mice. (*A*) Both BHB/AcAc and lactate/pyruvate ratios are controlled by the NADH/NAD$^+$ ratio. (*B*) In addition to the increased BHB/AcAc ratio, serum analysis from KD-treated animals shows *Kmt2d*$^{+/\beta Geo}$ mice had a significant increase in the lactate/pyruvate (Lac/Pyr) ratio compared with KD-treated *Kmt2d*$^{+/+}$ littermates (n = 12–15 per group). *$P < 0.05$.

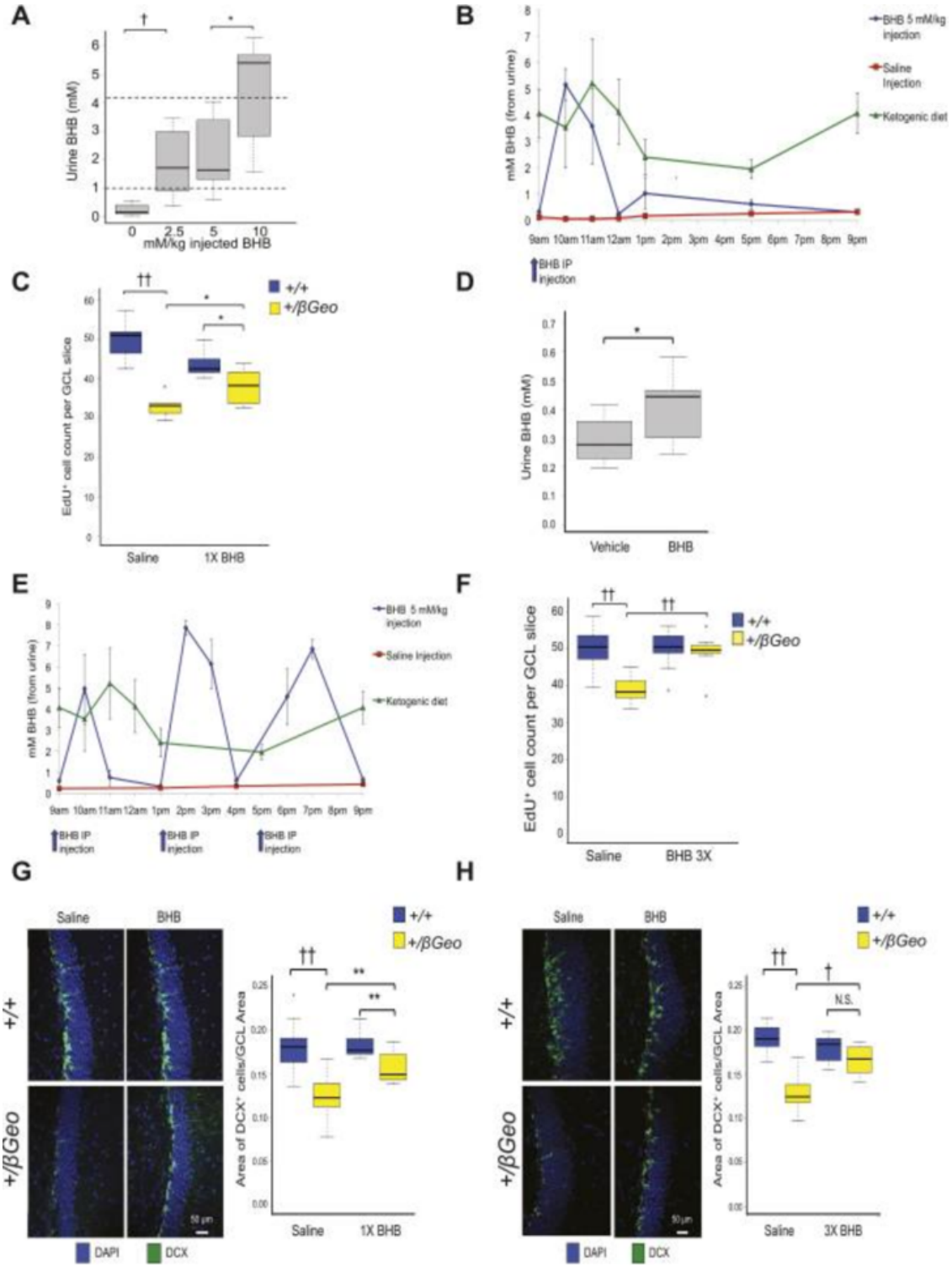

Supplementary Figure 9. Exogenous BHB treatment rescues the neurogenesis defect in *Kmt2d*$^{+/\beta Geo}$ mice. (*A*) Several distinct doses (0, 2.5, 5, 10 mM/kg) of BHB were injected i.p., followed by urine collection 1.5 h later (approximate time of BHB peak levels) (19). The 5 mM/kg

dose shows a BHB level that resembles the urine BHB profile (approximated in this figure with dashed lines) from KD-treated mice (n = 22 total). (*B*) A single 5 mM/kg BHB injection (9 AM) of BHB per day (for 2 wk) yielded comparable peak levels as mice on a KD but less total daily exposure, as seen from a urine time course (12 h; n = 4–5 per group). Also shown is the saline vehicle group. (*C*) *Kmt2d*$^{+/\beta Geo}$ mice injected with a once-daily dose of 5 mM/kg BHB (for 2 wk) show a significant increase in the EdU$^+$ cell numbers in the GCL of the DG of the mice compared with *Kmt2d*$^{+/\beta Geo}$ mice injected with saline vehicle. However, this rescue did not show the same magnitude of rescue compared with the EdU$^+$ cell numbers from KD treatment (n = 5–12). (*D*) Mice implanted with a 2-wk BHB pump that provided 2.5 mg/mL BHB at a rate of 0.25 μL/h showed a significant ($P < 0.05$) increase in BHB measured from urine (n = 10–12 per group). However, although the pump provided a constant stream of BHB, the urine BHB did not reach comparable levels to what was seen in mice on a KD (~1–2 mM BHB). (*E*) The combination of osmotic pumps and three injections of 5 mM/kg BHB at 9 AM, 1 AM, and 5 AM showed a more similar BHB profile to KD-treated mice when treated for 2 wk (n = 4–5 per group). (*F*) When treated with this higher daily dose of BHB for 2 wk, we saw a more pronounced rescue of EdU$^+$ cell numbers in the DG GCL in *Kmt2d*$^{+/\beta Geo}$ mice, which more closely mirrors the rescue seen after KD treatment. (*G* and *H*) We further confirmed the neurogenesis rescue at both low and high doses of BHB (treated for 2 wk) by looking at the fraction of DCX$^+$ cells in the DG GCL, and found that this measure showed similar neurogenesis rescues compared with EdU analysis (n = 7–10 per group). $^*P < 0.05$; $^{**}P < 0.01$; $^{\dagger}P < 0.005$. $^{\dagger\dagger}P < 0.001$. N.S., not significant, $P > 0.05$.

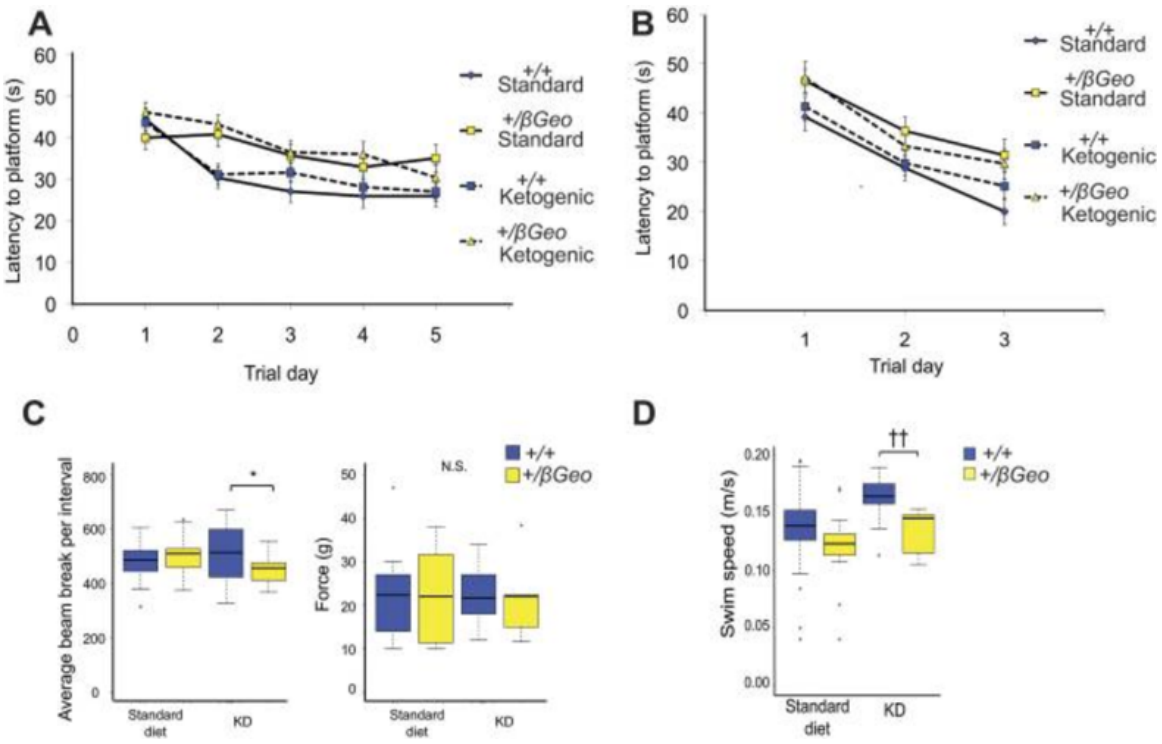

Supplementary Figure 10. Control experiments for behavioral testing. (*A*) The latencies to find the hidden platform during the 5 d of training showed a significant interaction ($P < 0.05$) between genotypes, but no significant effect from treatment ($P = 0.204$), as examined by a repeated-measures ANOVA. (*B*) The latencies to find the platform during the flag training did not show a significant interaction for either genotype or treatment ($P = 0.142$), as examined by a repeated-measures ANOVA ($n = 19–32$ per group). (*C*) *Kmt2d*$^{+/\beta Geo}$ mice did not show a significant difference from *Kmt2d*$^{+/+}$ mice on the regular diet, and did not demonstrate decreased activity on the KD in an open-field test, whereas *Kmt2d*$^{+/+}$ mice did show an increase ($P < 0.05$) in activity compared with *Kmt2d*$^{+/\beta Geo}$ mice only when both were treated with the KD. There were no differences for grip strength for either genotype or treatment ($n = 5–15$ per group). (*D*) *Kmt2d*$^{+/\beta Geo}$ mice did not show a significant difference from *Kmt2d*$^{+/+}$ mice on the regular diet, and did not have decreased activity on the KD, as measured by an open field test, whereas *Kmt2d*$^{+/+}$ mice did show an increase ($P < 0.001$) in activity compared with *Kmt2d*$^{+/\beta Geo}$ mice only when both were treated with the KD ($n = 13–26$ per group). The increased activity seen in wild-type animals on KD has been previously described (50). $^{*}P < 0.05$; $^{\dagger\dagger}P < 0.001$.

CHAPTER 3: PRECOCIOUS NEURONAL DIFFERENTIATION AND DISRUPTED OXYGEN RESPONSES IN KABUKI SYNDROME

Adapted from:

> **Carosso, G.A.**, Boukas, L., Augustin, J.J., Nguyen, H.N., Winer, B.L., Cannon, G.H., Robertson, J.D., Zhang, L., Hansen, K.D., Goff, L.A. and Bjornsson, H.T., 2019. Precocious neuronal differentiation and disrupted oxygen responses in Kabuki syndrome. *JCI Insight*, 4(20).

Graphical Abstract

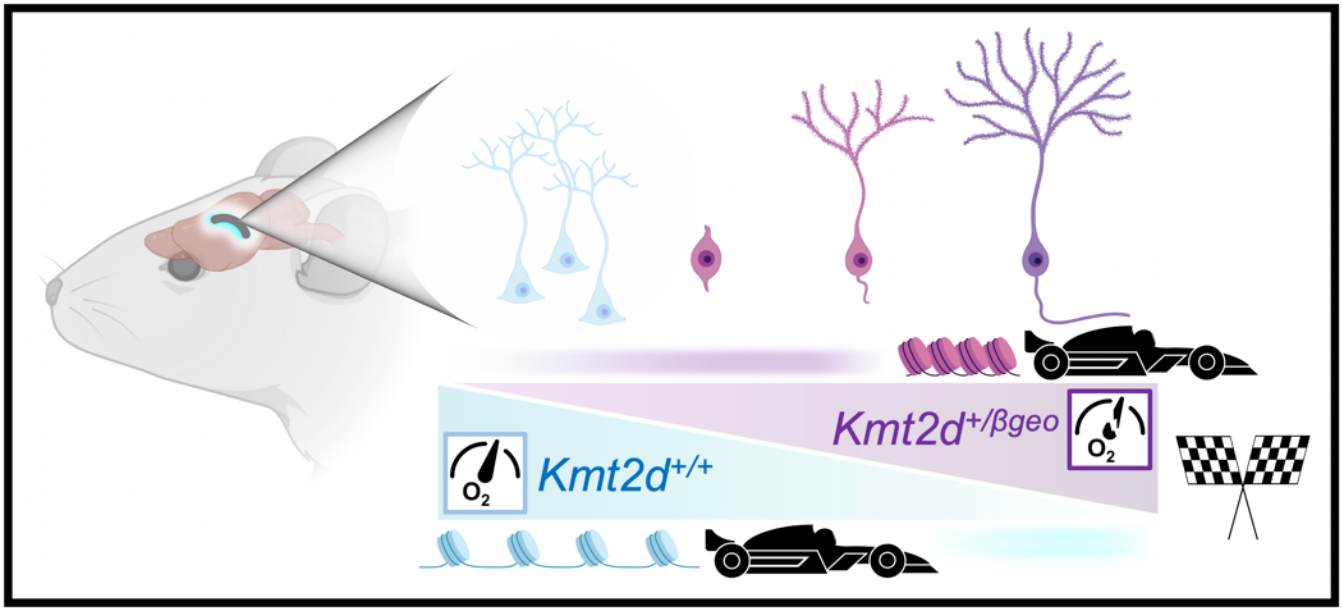

Abstract

Chromatin modifiers act to coordinate gene expression changes critical to neuronal differentiation from neural stem/progenitor cells (NS/PCs). Lysine-specific methyltransferase 2D *(KMT2D)* encodes a histone methyltransferase that promotes transcriptional activation, and is frequently mutated in cancers and in the majority (>70%) of patients diagnosed with the congenital, multisystem intellectual disability (ID) disorder Kabuki syndrome 1 (KS1). Critical roles for KMT2D are established in various non-neural tissues, but the effects of KMT2D loss in brain cell development have not been described. We conducted parallel studies of proliferation, differentiation, transcription, and chromatin profiling in KMT2D-deficient human and mouse models to define KMT2D-regulated functions in neurodevelopmental contexts, including adult-born hippocampal NSPCs in vivo and in vitro. We report cell-autonomous defects in proliferation, cell cycle, and survival, accompanied by early NSPC maturation in several KMT2D-deficient model systems. Transcriptional suppression in KMT2D-deficient cells indicated strong perturbation of hypoxia-responsive metabolism pathways. Functional experiments confirmed abnormalities of cellular hypoxia responses in KMT2D-deficient neural cells, and accelerated NSPC maturation in vivo. Together, our findings support a model in which loss of KMT2D function suppresses expression of oxygen-responsive gene programs important to neural progenitor maintenance, resulting in precocious neuronal differentiation in a mouse model of KS1.

Introduction

Trithorax group proteins promote chromatin accessibility by exerting antagonistic functions against Polycomb group transcriptional suppressors to activate gene expression (Schuettengruber et al. 2007). Fine-tuning of cell type transitions as NSPCs undergo neuronal development depends critically on this duality, based on the severe neurodevelopmental defects resulting from variants in numerous chromatin-modifying genes (Bjornsson 2015). Loss-of-function variants in genes encoding two such enzymes, KMT2D and lysine-specific demethylase 6A (KDM6A/UTX) produce the ID disorder KS (KS1 and KS2, respectively) (Ng et al. 2010; Miyake et al. 2013). Up to 74% (Hannibal et al. 2011) of KS cases result from mutations in *KMT2D* (KS1), encoding a major histone H3 lysine 4 (H3K4) methyltransferase, which catalyzes chromatin-opening modifications at context-specific targets. Specific requirements for KMT2D in cardiac precursors (Ang et al. 2016), B cells (Ortega-Molina et al. 2015; Zhang et al. 2015), muscle and adipose (Lee et al. 2013), and epithelial tissues (Lin-Shiao et al. 2018) have been shown for *KMT2D*-associated cardiac, immunologic, and oncogenic phenotypes (Froimchuk et al. 2017), yet the effects of KMT2D deficiency in neurodevelopment are not yet understood.

We previously described a mouse model of KS1, *Kmt2d*$^{+/\beta_{geo}}$, demonstrating characteristic features including craniofacial abnormalities and visuospatial memory impairments, associated with decreased numbers of adult-born hippocampal NSPCs in the dentate gyrus (DG) (Bjornsson et al. 2014). Decreased DG grey matter volume was subsequently observed in KS1 patients (Boisgontier et al. 2018). The continual birth and integration of new neurons makes adult neurogenesis the most potent form of lifelong plasticity in the brains of many mammals (Gonçalves et al. 2016), though recent studies disagree about its extent in humans (Sorrells et al. 2018; Moreno-Jiménez et al. 2019; Tobin et al. 2019). During late embryonic stages, a subset of multipotent NSPCs persists in the DG (Berg et al. 2019), and these cells are subject to an array of intrinsic and extrinsic factors affecting

their maintenance, i.e. self-renewal, proliferation, and neuronal differentiation, throughout adult life. Mounting evidence tightly links metabolic rewiring (Zheng et al. 2016) and hypoxic states in the DG (Mazumdar et al. 2010; Chatzi et al. 2015) to the cell-intrinsic regulation of NSPC maintenance.

Here, we find that KMT2D deficiency strongly suppresses metabolic gene expression and leads to reduced proliferation, abnormal hypoxia responses, and precocious neuronal maturation in multiple KS1 model systems. Importantly, these phenotypes were validated *in vivo* in a KS1 mouse model, supporting a role for these abnormalities in the pathogenesis of KS1-associated ID.

Results

Genetic ablation of the *Kmt2d* SET methyltransferase domain disrupts proliferation and cell cycle in a cell-autonomous manner

We first selected the HT22 mouse hippocampal neuronal cell line (Morimoto and Koshland 1990) for analysis of KMT2D catalytic function in a neuronal context. We deleted the gDNA sequence encoding the Su(var)3-9, enhancer-of-zeste and trithorax (SET) methyltransferase domain with CRISPR-Cas9, using an upstream small guide RNA ($sgRNA^{up}$) in exon 52, and either $sgRNA^{1}$ (exon 54) or $sgRNA^{2}$ (intron 54); this resulted in deletions of 565 bp ($Kmt2d^{\Delta 1}$) or 654 bp ($Kmt2d^{\Delta 2}$), respectively, as verified by Sanger DNA sequencing, in silico translation, and PCR (Supplementary Figure 3.1A-B). Targeted cells were clonally expanded to establish heterozygous ($Kmt2d^{+/\Delta}$) and homozygous ($Kmt2d^{\Delta/\Delta}$) cell lines to compare with the parental wild-type line ($Kmt2d^{+/+}$). Both the biological replicate alleles, $Kmt2d^{\Delta 1}$ and $Kmt2d^{\Delta 2}$, were included; thus, the combined data are denoted hereafter simply as $Kmt2d^{+/\Delta}$ or $Kmt2d^{\Delta/\Delta}$. The *Kmt2d* mRNA encoded within the targeted region was ~50% decreased in $Kmt2d^{+/\Delta}$ cells and absent in $Kmt2d^{\Delta/\Delta}$ cells, whereas the *Kmt2d* mRNA from exons upstream of the deletion site was unaffected (Supplementary Figure 3.1C). Immunofluorescence against KMT2D, detecting a peptide sequence upstream of deletions

(Supplementary Figure 3.1D), demonstrate a distinct nuclear distribution of KMT2D in *Kmt2d*$^{+/+}$ cells but it was more diffuse in *Kmt2d*$^{+/\Delta}$ and *Kmt2d*$^{\Delta/\Delta}$ cells, whereas the expression of a neuronal nuclear marker, RNA binding protein fox-1 homolog 3 (RBFOX3), was uniformly nuclear, independent of genotype (Figure 3.1A).

Proliferation analysis after equal-density plating revealed cell densities ~52% less in *Kmt2d*$^{+/\Delta}$ cells and ~39% less in *Kmt2d*$^{\Delta/\Delta}$ cells, compared to wild-type (Figure 3.1B). This defect was supported by dye-based generational tracking, which detected a modestly reduced dilution of the fluorescent tracer, i.e. fewer cell divisions, in *Kmt2d*$^{+/\Delta}$ and *Kmt2d*$^{\Delta/\Delta}$ daughter cells compared to wild-type (Figure 3.1C, Supplementary Figure 3.1E). on the other hand, the initial dye uptake in parental cells was genotype-independent. Flow cytometric analysis of cell cycle occupancy, using marker of proliferation, Ki-67 (KI67) and a DNA label, revealed that more *Kmt2d*$^{+/\Delta}$ and *Kmt2d*$^{\Delta/\Delta}$ cells were in S and G_2 phase, compared to wild-type (Figure 3.1D, Supplementary Figure 3.1F). To determine temporal dynamics of cell cycle progression, we synchronized cells in G_2/M phase and analyzed DNA content at timepoints after release (Figure 3.1E). At 3 hours - 18 hours after release, wild-type cells exited G_2/M phase at higher rates than *Kmt2d*$^{\Delta/\Delta}$ cells, . Cell death was analyzed by flow cytometric detection of caspase-3/7 substrate cleavage, which can distinguish early apoptotic cells. Compared to wild-types, apoptotic cells were greater in both *Kmt2d*$^{+/\Delta}$ cells (~287%) and *Kmt2d*$^{\Delta/\Delta}$ cells (~478%) (Figure 3.1F).

To examine proliferation in primary hippocampal progenitors, we isolated NSPCs from micro-dissected DG of *Kmt2d*$^{+/\beta geo}$ mice and wild-type littermates. Most NSPCs expressed the NSPC marker nestin (NES), with a minority of cells expressing mature neuron marker calbindin (CALB) (Figure 3.1G). Cells were plated at equal density and pulsed with cell division marker 5-ethynyl-2′-deoxyuridine (EdU), then quantified by confocal microscopy. Compared to wild-type, *Kmt2d*$^{+/\beta geo}$

NSPCs had lower proliferation rates as measured by EdU incorporation and cell density (Figure 3.1H).

Our findings of proliferation defects, G_2/M cell cycle delay, and increased apoptosis in hippocampal cells whose *Kmt2d* had been inactivated by SET domain deletion, together with proliferation defects in primary *Kmt2d*$^{+/\beta geo}$ hippocampal NSPCs, support a role for KMT2D activity in neurodevelopment.

Loss of the KMT2D SET methyltransferase domain suppresses transcription of KMT2D-regulated hypoxia response genes

We performed high-coverage RNA-seq comparing three *Kmt2d*$^{\Delta/\Delta}$ clones against the parental *Kmt2d*$^{+/+}$ line, each clone intriplicate, followed by differential expression analysis. These libraries clustered robustly by genotype with clear separation of *Kmt2d*$^{\Delta/\Delta}$ cells from *Kmt2d*$^{+/+}$ by Principal Component Analysis (PCA). We found 575 differentially-expressed genes (DEGs) that met the significance test (See methods). (Figure 3.2A, Supplementary Figure 3.2A-B, Supplementary Table 1). ~76% of DEGs (436 genes) were downregulated in *Kmt2d*$^{\Delta/\Delta}$ cells, including known KMT2D targets such as Krueppel-like factor 10 (*Klf10*) (8), revealing that the global transcription was strongly suppressed following inactivation of *Kmt2d*. Overrepresentation analysis (ORA) revealed significant enrichment of gene networks among *Kmt2d*$^{\Delta/\Delta}$ downregulated DEGs, including glycolysis and hypoxia-inducible factor 1A (HIF1A) signaling, whereas fewer networks were enriched in *Kmt2d*$^{\Delta/\Delta}$ upregulated DEGs (Figure 3.2B).

We reasoned that among *Kmt2d*$^{\Delta/\Delta}$ DEGs, the subset of genes that could also bind KMT2D itself in wild-type cells, would more likely represent the direct transcriptional consequences of *Kmt2d* inactivation, whereas non-bound DEGs might reflect secondary effects. We performed chromatin immunoprecipitation, followed by high-throughput sequencing (ChIP-seq) using a previously

validated ChIP-grade KMT2D antibody (Lee et al. 2013) in *Kmt2d*$^{+/+}$ HT22 cells. We identified 3,756 KMT2D binding peaks that were significantly enriched over input (Supplementary Table 3.2). ~10% of them occur inside promoters, ~33% (1,235 peaks) occur within 5 kb of a transcription start site (TSS±5kb), and ~25% occur within 2 kb (TSS±2kb) (Supplementary Figure 3.2C-F). To account for promoter and enhancer interactions, we reasoned that TSS±5kb peaks, compared to more distal peaks, most likely reflect KMT2D cis-regulatory functions on proximal genes, so we refer to them as KMT2D-bound genes. The 1,463 observed KMT2D-bound genes (Supplementary Table 3) were significantly enriched in mRNA 3'UTR binding, rho GTPase signaling, circadian clock, translation, oxidative stress, HIF1A signaling, and other pathways (Supplementary Figure 3.2G).

Then we intersected KMT2D-bound genes with *Kmt2d*$^{\Delta/\Delta}$ DEGs and found 74 likely direct target genes (Supplementary Table 3; ~85% (63 genes) were downregulated (Figure 3.2C); these include insulin-like growth factor 1 (*Igf1*), and fos-like antigen 2 (*Fosl2*). At least 20 observed KMT2D-bound, *Kmt2d*$^{\Delta/\Delta}$ DEGs had been previously reported to be KMT2D targets in other tissues (Ortega-Molina et al. 2015; Guo et al. 2012). KMT2D-bound, *Kmt2d*$^{\Delta/\Delta}$ down-DEGs were most significantly enriched for pathways involved in face morphogenesis, glycolysis, hypoxia response, and proliferation; surprisingly, 29 of these 63 genes are also regulated by HIF1A (Semenza 2000). Although craniofacial features are prominent in KS1, we believe that the enrichment of face morphogenesis genes in HT22 cells most likely reflects pleiotropic functions of face morphogenesis genes. KMT2D ChIP-seq peaks on HIF1A-regulated genes were clustered at promoters and enhancers, often overlapping CpG islands (*Fosl2)*, or clustering at alternative TSSs, (retinoic acid receptor alpha (*Rara*)), or in enhancer-like peaks, (DNA-damage-inducible transcript 4 (*Ddit4*)) (Figure 3.2D, Supplementary Figure 3.2H).

As a large fraction of KMT2D-bound, *Kmt2d*$^{\Delta/\Delta}$ DEGs control oxygen-responsive metabolism, we interrogated the shared KMT2D and HIF1A binding sites. First, we intersected KMT2D peaks with HIF1A peaks previously found in embryonic heart (Guimarães-Camboa et al. 2015), and found that 423 regions overlapped (Figure 3.2E). Like KMT2D, HIF1A showed ~10% of peaks located inside promoters, but among shared KMT2D/HIF1A-bound peaks this fraction approached ~40%, supporting cooperative regulatory activity (Supplementary Figure 3.2I). We identified 289 genes whose start site occurred within 5kb of the overlapped KMT2D/HIF1A-bound peaks, including 8 *Kmt2d*$^{\Delta/\Delta}$ DEGs (Supplementary Table 3). To check if KMT2D/HIF1A-bound genes are seen in other tissues we interrogated other reported gene sets having experimentally validated, hypoxia-induced HIF1A binding in their promoter (Benita et al. 2009). Of 86 validated genes, 5 were KMT2D-bound, *Kmt2d*$^{\Delta/\Delta}$ downregulated DEGs, 23.3-fold more than expected by chance (Fisher's Exact Test, p=4.74e-6) (Supplementary Table 3). Of 81 genes validated in three or more tissues, 3 were KMT2D-bound, *Kmt2d*$^{\Delta/\Delta}$ downregulated DEGs: *Klf10*, *Rara*, and *Ddit4* (Fisher's Exact Test, p=0.002).

Given the prevalence of oxygen response genes among *Kmt2d*$^{\Delta/\Delta}$ downregulated DEGs and shared KMT2D/HIF1A targets, we hypothesized that KMT2D had a positive regulatory role in the transcriptional responses to hypoxia in HT22 cells. We subjected *Kmt2d*$^{+/+}$, *Kmt2d*$^{+/\Delta}$, and *Kmt2d*$^{\Delta/\Delta}$ cells to normoxia (21% O_2) or hypoxia (1% O_2), and measured hypoxia-induced gene expression responses. Analysis of canonical HIF1A targets, vascular endothelial growth factor A (*Vegfa*), Bcl2/adenovirus E1B 19-KD protein-interacting protein 3 (*Bnip3*), DNA-damage-inducible transcript 3 (*Ddit3*), and cyclin-dependent kinase inhibitor 1A (*Cdkn1A*), in *Kmt2d*$^{+/+}$ cells revealed robust upregulations upon hypoxic exposure; in contrast, *Kmt2d*$^{+/\Delta}$ and *Kmt2d*$^{\Delta/\Delta}$ cell lines failed to induce these genes to comparable levels (Figure 3.2F, Supplementary Figure 3.2J). Under hypoxic conditions, HIF1A undergoes nuclear translocation, i.e. activation. We therefore quantified the

HIF1A fluorescence in the nucleus under normoxia (21% O_2) and hypoxia (1% O_2) (Supplementary Figure 3.2K). Unexpectedly, we found that under normoxia, *Kmt2d*$^{\Delta/\Delta}$ cells exhibited >2-fold HIF1A activation than *Kmt2d*$^{+/+}$ cells. Upon hypoxic exposure, HIF1A activation doubled in wild-type cells, but failed to respond in *Kmt2d*$^{+/\Delta}$ cells and *Kmt2d*$^{\Delta/\Delta}$ cells.

Taken together, our data suggest that KMT2D plays an important role in positively regulating HIF1A-inducible, oxygen-responsive metabolic gene programs in neuronal cells.

KS1 patient-derived cells recapitulate KMT2D-associated defects in proliferation and cell cycle

We reprogrammed skin biopsy fibroblasts to generate induced pluripotent stem cells (iPSCs) from a previously described female KS1 patient with a heterozygous nonsense *KMT2D* mutation (c.7903C>T:p.R2635*); she had characteristic facial features, congenital heart disease, and visuospatial memory impairments (Sanz et al. 2010). We selected iPSCs (KS1-1) with a normal 46, XX karyotype (Supplementary Figure 3.3A) and characteristic morphology (Figure 3.3A) for comparison with the previously described iPSC lines from unrelated healthy controls (C1-2, C3-1) (Wen et al. 2014). *KMT2D* mRNA quantification in KS1 iPSCs confirmed the decreased message compared to controls, as expected for haploinsufficiency (Supplementary Figure 3.3B-C). Quantification after EdU pulse demonstrated lower proliferation rates (~25%) in KS1 iPSCs compared to controls (Figure 3.3B), accompanied by the expected shift in cell cycle occupancy (Figure 3.3C, Supplementary Figure 3.3D) favoring G_2/M phase (24% more cells).

We next generated NES-expressing NSPCs through parallel differentiation of KS1 and control iPSCs, using an established small molecule inhibition protocol (Li et al. 2011). We confirmed that *KMT2D* was decreased in KS1 NSPCs by RT-qPCR (Supplementary Figure 3.3E), and that the cells had normal morphology, independent of genotype (Figure 3.3D, Supplementary Figure 3.3F).

EdU incorporation rates revealed KS1 NSPCs had a marked proliferation defect (~47% reduced, Figure 3.3E) and fewer mitotic divisions (Supplementary Figure 3.3G). KS1 NSPCs did not display a cell cycle defect (Figure 3.3F, Supplementary Figure 3.3H), suggesting either cell-type dependence or loss of this phenotype during in vitro differentiation. Flow cytometry indicated higher proportions of dying cells in KS1 samples compared to controls among both iPSCs (~130%) and NSPCs (~115%) (Figure 3.3G, Supplementary Figure 3.3I-J).

To determine whether G_2/M bias, seen in KS1 iPSCs, occurred in unmanipulated primary cells from additional KS1 patients, we analyzed fibroblasts from three molecularly confirmed KS1 patients (KS1-1, KS1-2, KS1-3) and healthy controls. Fibroblasts were synchronized in G_2/M phase followed by flow cytometric analysis of DNA content. At 3 hours post-release, control cells had exited G_2/M phase, in contrast to KS1 cells which remained in G_2/M (Figure 3.3H). Thus, delayed G_2/M exit was consistent in primary, non-reprogrammed cells from three KS1 patients.

Transcriptional suppression of metabolic genes in cycling cells, and precocious neuronal differentiation in KS1 patient-derived NSPCs

To interrogate transcriptional consequences of *KMT2D* loss in the context of neuronal differentiation, we performed single-cell RNA sequencing (scRNA-seq) in iPSCs and NSPCs from the KS1 patient and controls (Supplementary Figure 3.4A). The expression of cell-type markers confirmed that libraries segregated into clusters reflecting distinct cell identities of the expected lineages (Supplementary Figure 3.4B-D).

First, differential expression analysis in iPSCs and NSPCs identified genes downregulated or upregulated in KS1 patient relative to healthy controls (Supplementary Figure 3.4E). KS1 iPSCs displayed strong transcriptional suppression among 421 DEGs, with 372 genes down and 49 genes up (Supplementary Table 4). NSPCs showed 346 significant DEGs (147 genes were down and 199

genes were up) (Supplementary Table 5). Intersection of KS1 iPSC and NSPC DEG lists showed that 40 genes were shared down and 10 genes were shared up (Supplementary Figure 3.4F-G, Supplementary Table 6). Shared down genes included glycolysis genes, aldehyde dehydrogenase 7 family member A1 (*ALDH7A1*), enolase 1 (*ENO1*), and triosephosphate isomerase 1 (*TPI1*), as well as factors important to stem cell maintenance including proliferation-associated protein 2G4 (*PA2G4*) and protein lin-28 homolog A (*LIN28A*). As for *Kmt2d*$^{\Delta/\Delta}$ HT22 cells, downregulated genes in KS1 patient iPSCs and NSPCs were significantly enriched for HIF1A direct targets, genes containing the hypoxia-responsive element (HRE) 5'-RCGTG-3' motif, and known hypoxia response genes (Supplementary Figure 3.4H).

We next focused on NSPCs from KS1 and controls to interrogate transcriptional effects during neuronal differentiation. We used Uniform Manifold Approximation and Projection (UMAP), a sensitive assay to visualize single cell transcriptomes, while preserving both local and global relationships (McInnes et al. 2018). Control NSPCs were tightly clustered, indicating similar expression profiles, in contrast to KS1 cells which were distinctly separated, at first but gradually a subset (top) of cells resembled more closely the clustering of the controls (Figure 3.4A). We then partitioned single-cell libraries into developmentally informative subsets as follows: First, we verified that differential KS1gene expression in NSPCs was not due to differences in cell cycle phase composition (Supplementary Figure 3.5A, Supplementary Table 7). Next, we partitioned cells by the expression of stage-specific markers to define a differentiation trajectory consisting of early or "cycling" NSPCs, "transitioning" NSPCs, and "differentiating" NSPCs (Figure 3.4B). Cycling cells comprised the majority of NSPCs analyzed and exhibited the greatest KS1-associated expression differences, whereas expression profiles of transitioning and differentiating NSPCs show gradual convergence of gene expression. We analyzed DEGs exclusively within cycling, transitioning, and differentiating NSPC subsets to determine if particular gene networks drive transcriptional

differences in a stage-specific manner (Figure 3.4C, Supplementary Table 7). KS1 DEGs in transitioning NSPCs, (and to a lesser extent cycling NSPCs), showed enrichment of genes comprising the Notch signaling pathway, including delta-like protein 3 (*DLL3*), protein jagged-1 (*JAG1*), transcription factor HES-5 (*HES5*), and cyclin D1 (*CCND1*). Cycling NSPCs had DEGs enriched in glycolysis pathways.

Apart from increased rates of KS1 cell death (Figure 3.3G), another possible factor in the observed decrease of proliferative KS1 NSPCs (Figure 3.3E) could be a change in cellular differentiation, such as precocious cell maturation, resulting in depletion of cycling precursors. To explore this by scRNA-seq, we examined markers ranging from immature cells ($PAX6^{+}$) to the most differentiated cells ($MAP2^{+}$) (Figure 3.4D-E). We further restricted analysis to the transitioning and differentiating, i.e. "maturing" NSPC subset (Supplementary Figure 3.5B), defining a trajectory that enabled parsing of cells into binned deciles of increasing maturation (Supplementary Figure 3.5C-H). Quantification of cell densities revealed strong bias of KS1 NSPCs in the most matured bins relative to controls (Figure 3.4F), i.e. greater representation of mature NSPCs from KS1 than controls. Using flow cytometry, we corroborated these transcriptional signatures at the protein level, finding KS1 NSPCs increased MAP2 fluorescence and decreased PAX6 fluorescence, relative to control (Figure 3.4G-H).

Together, these results link transcriptional suppression of metabolic gene pathways to cell-autonomous proliferation defects in stem cell models from a KS1 patient; our scRNA-seq data suggest that precocious differentiation of NSPCs could contribute to KS1-associated neurodevelopmental defects.

In vivo defects of neurogenesis and NSPC differentiation in a *Kmt2d*$^{+/\beta geo}$ mouse model of KS1

Finally, we asked whether proliferative defects, transcriptional suppression, and precocious differentiation phenotypes validate in vivo, using an established KS1 mouse model. *Kmt2d*$^{+/\beta geo}$ mice, bearing a *Kmt2d* truncating mutation, were previously found to have visuospatial memory impairments and fewer doublecortin (DCX$^+$) NSPCs in the DG subgranular zone (SGZ) (Benjamin et al. 2017; Bjornsson et al. 2014), but the progression of the NSPC lineage in *Kmt2d*$^{+/\beta geo}$ mice has not been characterized.

We conducted cell cycle and RNA-seq analysis in *Kmt2d*$^{+/\beta geo}$ mice, using an EdU pulse paradigm to label adult-born cells. We sampled micro-dissected DG within 1 cell cycle (16 hours) to capture the full complement of dividing NSPCs (Figure 3.5A), then purified EdU$^+$ nuclei by fluorescence-activated cell sorting (FACS) (Figure 3.5B, Supplementary Figure 3.6A). DNA content analysis revealed enrichment of G_2/M phase in *Kmt2d*$^{+/\beta geo}$ EdU$^+$ DG nuclei (Figure 3.5C). We next profiled transcription by RNA-seq in purified EdU$^+$ DG nuclei, yielding 827 DEGs (Supplementary Figure 3.6B-C, Supplementary Table 8). The 416 down-regulated genes in *Kmt2d*$^{+/\beta geo}$ nuclei were enriched for misfolded protein binding, TCA cycle, proteasome complex, oxygen response, and poly(A) RNA-binding genes. Given the observed downregulation of poly(A) RNA-binding genes, we considered the possibility that improper 3'UTR-mediated mRNA metabolism could lead to accumulation of transcripts influencing NSPC maturation. Indeed, despite little overall bias toward up or downregulation in *Kmt2d*$^{+/\beta geo}$ DG nuclei, our study of positive regulators of neuronal differentiation revealed a marked predominance of upregulated pro-neural transcripts (only 3 genes down but 14 genes up), including copine-1 (*Cpne1*), focal adhesion kinase 1 (*Ptk2*), ras-related protein RAB11A (*Rab11A*), and retinoblastoma-associated protein 1 (*Rb1*). Of interest, KS1 patient's NSPCs also showed upregulated pro-neural genes such as nuclear receptor subfamily 2, group F, member 1 (*NR2F1*) and pro-neural transcription factor HES-1 (*HES1*), whereas *Kmt2d*$^{\Delta/\Delta}$ HT22 cells had upregulated brain-derived neurotrophic factor (*Bdnf*) and neuron-specific

microtubule component (*Tubb3/Tuj1*). Such pro-neural gene expression observed across KS1 models raises the possibility that NSPC differentiation rates could be altered in *Kmt2d*$^{+/\beta geo}$ mice.

To examine NSPC lineage progression in vivo, we analyzed stage-specific cell abundances both at steady-state and after birthdating of adult-born NSPCs by EdU pulse, comparing *Kmt2d*$^{+/\beta geo}$ mice to sex- and age-matched *Kmt2d*$^{+/+}$ littermates (Figure 3.5D, Supplementary Figure 3.6D).

At steady-state, we observed significantly fewer NSPCs in *Kmt2d*$^{+/\beta geo}$ mice compared to *Kmt2d*$^{+/+}$ mice at all stages (Figure 3.5E). The cell division marker, minichromosome maintenance complex component 2 (MCM2), distinguished NES^{+} NSPCs in the quiescent (MCM2^{-}) or activated (MCM2^{+}) state. Quiescent radial glia-like (qRGL, NES^{+}MCM2^{-}) NSPCs were ~39% less numerous in *Kmt2d*$^{+/\beta geo}$ mice, indicating a baseline paucity in the stem cell pool. Activated RGL (aRGL, NES^{+}MCM2^{+}) NSPCs were ~43% less numerous, and intermediate progenitor cell (IPC, NES^{-} MCM2^{+}) NSPCs were ~26% fewer. We confirmed prior observations of fewer neuroblast (NB, DCX^{+}) NSPCs, finding a 28% decrease in *Kmt2d*$^{+/\beta geo}$ mice. By stratifying analysis along the septotemporal axis of the DG, we observed that aRGL NSPC reductions in *Kmt2d*$^{+/\beta geo}$ mice were more pronounced in the septal DG than the temporal region (Supplementary Figure 3.6E), congruous with spatial memory defects localized to the septal DG (Morris et al. 2012). Because DCX^{+} NSPCs migrate radially during maturation, we compared radial distances of DCX^{+} cell bodies from the SGZ plane and observed increased distances in *Kmt2d*$^{+/\beta geo}$ mice (Supplementary Figure 3.6F). Finally, despite diminished NSPC populations in *Kmt2d*$^{+/\beta geo}$ mice, we observed no numeric differences among mature neurons (RBFOX3^{+}) (Supplementary Figure 3.6G), nor were gross anatomical differences seen by MRI volumetric analysis (Supplementary Figure 3.6H, Supplementary Table 9).

From these data, we then calculated a lineage progression index to approximate the expansion potential of each successive neurogenic cell type. Although *Kmt2d*$^{+/\beta geo}$ mice showed fewer

total NSPCs of each type at steady-state, the lineage progression index at each cell-type transition did not differ significantly (Supplementary Figure 3.6I), suggesting that particular cell-type transition impairments are not responsible for the adult neurogenesis defect. However, we did note substantially higher variance of RGL activation rates in *Kmt2d*$^{+/\beta geo}$ mice, suggesting impaired coordination of NSPC mitotic entry (Supplementary Figure 3.6J).

Pulse-labeling with marker-based imaging enables precise measurement of birth dates, i.e. mitotic division, of specific cell types. To resolve temporal dynamics of NSPC differentiation in *Kmt2d*$^{+/\beta geo}$ and wild-type mice, we pulsed adult mice with EdU for a period of 2 weeks, during which a subset of labeled DG cells is expected to reach a late NSPC (NB) stage, characterized by radial extension of a DCX$^+$ neuronal process. In contrast, another subset of pulsed cells, bearing a NES$^+$ qRGL-like process, represents NSPCs that remain in a stem-like state. Thus, by quantifying EdU-labeled cells exhibiting either a DCX$^+$ neuronal process (EdU$^+$DCX$^+$) or a NES$^+$ qRGL-like process (EdU$^+$NES$^+$) (Figure 3.5F, Supplementary Figure 3.7A), one can compare relative differentiation status, where a higher proportion of EdU$^+$DCX$^+$ cells would indicate early or precocious maturation. Indeed, though steady-state cell numbers again confirmed fewer total NES$^+$ and DCX$^+$ NSPCs in *Kmt2d*$^{+/\beta geo}$ mice compared to wild-types, among pulsed cells the *Kmt2d*$^{+/\beta geo}$ mice exhibited a significantly greater fraction of EdU$^+$DCX$^+$ immature neurons (Figure 3.5F). In other words, *Kmt2d*$^{+/\beta geo}$ DG NSPCs born within the preceding 2 weeks had achieved a more advanced differentiation state than wild-type cells born in the same window.

Together, studies of adult neurogenesis dynamics in *Kmt2d*$^{+/\beta geo}$ mice suggest that in vivo neurodevelopmental effects of KMT2D loss recapitulate many phenotypes observed initially in vitro using mouse HT22 cells and KS1 human-derived cells. While comparison of gene expression profiles across these KS1 models revealed few individual genes with shared dysregulation among all

models, at network level we observed high enrichment of HIF1A regulatory and RNA metabolism pathways in a comparison of all DEGs in these KS1 models (Supplementary Figure 3.8A-D).

Precocious differentiation and reduced hypoxia responses in *Kmt2d*$^{+/\beta geo}$ primary hippocampal NSPCs

Cellular oxygen availability has previously been directly linked to maintenance and differentiation of embryonic (Zhu et al. 2011; Mazumdar et al. 2010; Zheng et al. 2016) and adult DG NSPCs. Primary hippocampal NSPCs of *Kmt2d*$^{+/\beta geo}$ mice showed increased HIF1A activation compared to wild-type NSPCs, and both genotypes showed increased HIF1A activation upon treatment by HIF1A-stabilizing agent dimethyloxaloylglycine (DMOG) for 12 hours (Supplementary Figure 3.9A). We then subjected NSPCs to a standard in vitro neuronal differentiation protocol, quantifying cell marker expression between 0-8 days (Supplementary Figure 3.10A-B). Prior to differentiation (day 0), wild-type NSPCs expressed low levels of a mature DG neuron marker, prospero-related homeobox 1 (PROX1), while *Kmt2d*$^{+/\beta geo}$ NSPCs surprisingly showed an increase (Supplementary Figure 3.10C). By measuring expression of a pro-neural transcription factor, achaete-scute homolog 1 (ASCL1), we observed a baseline decrease (day 0) in *Kmt2d*$^{+/\beta geo}$ NSPCs compared to wild-type (Supplementary Figure 3.10D). In contrast, after 2 days in differentiation conditions, *Kmt2d*$^{+/\beta geo}$ NSPCs responded with greater ASCL1 expression compared to wild-types, an effect sustained at 4 and 8 days. DMOG treatment increased ASCL1 levels in both genotypes, though to greater magnitude in wild-type than *Kmt2d*$^{+/\beta geo}$ NSPCs. Together, these data are consistent with a link between cellular hypoxia response and neuronal differentiation in hippocampal NSPCs (Mazumdar et al. 2010).

Discussion

The ID disorder KS1 is caused by mutations in the histone methyltransferase *KMT2D*, but mechanistic links to neurodevelopmental and cognitive consequences in patients are not yet clear. KS1 diagnoses are typically made after childbirth, but the inherent reversibility of chromatin modifications raises the possibility that a detailed understanding of KMT2D activity in neuronal cells could identify molecular targets for postnatal interventions in KS1-associated ID.

Here, we report that KMT2D-deficient human and mouse neurodevelopment models, in vitro and in vivo, demonstrate similar patterns of transcriptional suppression, proliferative defects, and precocious cellular differentiation. These phenotypes were cell-autonomous in vitro, suggesting that 1) chromatin and gene expression studies in neurogenic cell types could yield disease-relevant KMT2D targets and 2) these cellular models provide platforms for screening of novel therapeutic strategies or targeted manipulations. We performed transcriptomic and KMT2D profiling in these models and observed systematic suppression of hypoxia response pathways, particularly among HIF1A-regulated genes that are also directly KMT2D-bound in neuronal cells. Physically overlapping KMT2D- and HIF1A-bound genomic loci were observed across tissues, ~40% of these at promoters, raising the possibility of shared etiologies in embryonically distinct KS1-affected organ systems. Furthermore, KMT2D-deficient neuronal cells, in contrast to isogenic wild-type cells, were unable to mount characteristic hypoxia-inducible gene activation responses when exposed to low-oxygen conditions, demonstrating oxygen response defects in KS1 models.

The implication of hypoxia response defects in KS1 suggests clinical relevance of recent findings in neurodevelopmental regulation. First, the adult hippocampal NSPC niche harbors locally hypoxic, but dynamic, microenvironments and the hypoxic state positively influences NSPC survival (Chatzi et al. 2015; Mazumdar et al. 2010). Thus, compromised hypoxia responses could render cells particularly vulnerable to changes in oxygen levels as experienced by maturing NSPCs as they migrate from DG SGZ vasculature. Second, NSPC maturation is coupled to a metabolic rewiring

from glycolysis in early NSPCs, to oxidative phosphorylation in maturing neurons. Zheng and colleagues (Zheng et al. 2016) recently found this metabolic switch, marked by suppression of glycolytic genes, to be essential for neuronal maturation. In KS1 neural models we observed suppression of hypoxia-responsive glycolytic genes accompanied by upregulation of pro-neuronal differentiation genes, and demonstrated precocious maturation of DG NSPCs by in vivo pulsing of adult *Kmt2d*$^{+/\beta geo}$ mice, as well as in vitro differentiation of *Kmt2d*$^{+/\beta geo}$ primary DG NSPCs. Future studies could determine whether targeted chromatin opening at hypoxia response loci normalizes differentiation dynamics in KS1 NSPCs.

Analogous findings regarding premature activation of terminal differentiation genes, reduced proliferation, and precocious maturation in KMT2D-depleted keratinocytes were recently linked to disorganized epidermal stratification (Lin-Shiao et al. 2018). Furthermore, in KMT2D-deficient cardiomyocytes, loss of H3K4me2 at KMT2D-bound hypoxia response genes associated with cell cycle and proliferative defects in heart development (Ang et al. 2016). In contrast, KMT2D deletion in B cells conferred proliferative advantage and impaired cell maturation, despite significant up-regulation of differentiation genes (Zhang et al. 2015; Lee et al. 2013). Thus, while KMT2D's role in enhancer-mediated gene expression during differentiation is well-established (Froimchuk et al. 2017), phenotypic manifestations appear cell type- and stage-dependent. We now extend KMT2D-associated phenotypes of transcriptional perturbance, hypoxia response, cell cycle, proliferation, and premature differentiation to neuronal contexts. Phenotypic concordance across tissues of disparate embryonic origin suggests that KMT2D targets important to KS1 phenotypes support basic cellular homeostatic functions related to housekeeping, energy production, and cell cycle progression, rather than genes with purely brain-specific function. Furthermore, we report concordant phenotypes both from nonsense *KMT2D* mutations (patient iPSCs and NSPCs), and mutations limited to the

KMT2D SET domain (HT22 cells, *Kmt2d*$^{+/\beta geo}$ mice), indicating that loss of either gene dosage or catalytic function of KMT2D can be pathogenic.

Present results indicate that adult hippocampal neurogenesis defects, which we previously found to associate with visuospatial memory defects in *Kmt2d*$^{+/\beta geo}$ mice, are observable at all stages examined, including fewer quiescent NSPCs in the DG which could indicate either post-natal depletion or altered niche development in the embryo. Despite having fewer total NSPCs, by pulse-chase experiments we observed the *Kmt2d*$^{+/\beta geo}$ NSPC population to achieve a more advanced maturation stage than that of wild-type littermates. Interestingly, adult-born NSPCs wield a disproportionately strong influence on DG circuitry and visuospatial learning during younger, but not older, neuronal maturation stages (Zhuo et al. 2016). This stage-dependent coupling of NSPC maturation with cognitive outcomes increases the likelihood that accelerated neuronal differentiation rates could negatively impact visuospatial memory acquisition. Furthermore, multispecies comparisons demonstrate that measured decreases in neurogenesis rates are consistent with accelerated neuronal maturation rates across the lifespan (Snyder 2019).

The apparent paradox of increased HIF1A activation, despite blunted hypoxia-responsive expression in *Kmt2d*$^{+/\Delta}$ and *Kmt2d*$^{\Delta/\Delta}$ neuronal cells raises two possibilities. First, chronic HIF1A activity could result in cellular compensatory efforts to downregulate hypoxia response genes. In this case, heterochromatin environments at HIF1A-binding genes could prevent induction. Alternatively, cellular oxygen sensing could be coupled to gene expression through chromatin states in a HIF1A-independent manner. Independent studies recently discovered direct oxygen sensing by KDM6A/UTX (the H3K27 demethylase lost in KS2 patients) as well as the H3K4/H3K36 demethylase 5A (KDM5A), which controlled chromatin states and cell differentiation in a HIF1A-independent manner (Chakraborty et al. 2019; Batie et al. 2019). These findings link hypoxia-induced histone methylation at H3K4, H3K27, H3K9, and H3K36 directly with control of maturation in

multiple cell types, further supporting the notion that KS-associated transcriptional suppression, in the adult DG context, could impact NSPC stage-dependent learning (Zhuo et al. 2016) via metabolic dysregulation. Hypoxia-upregulated H3K4me3 peaks (Batie et al. 2019) were enriched in HIF1A target gene promoters, where we presently observed high overlaps in KMT2D/HIF1A-bound loci. Strikingly, loss of KDM5A, whose activity opposes that of KMT2D at H3K4 sites, caused upregulation of hypoxia-responsive genes (Batie et al. 2019), i.e. an effect opposite to the present KS1-associated suppression of hypoxia response genes such as *Klf10* and *Bnip3l*. Several histone demethylases, and at least 33 chromatin modifiers in total, have been shown to impact hypoxia response genes, 11 of these associating with developmental disorders or cancers, yet KMT2D and other histone methyltransferases had not yet been implicated (Luo and Wang 2018).

In summary, our findings suggest that KMT2D deficiency disrupts neurogenesis by negatively impacting NSPC maintenance functions including cell cycle, proliferation, and survival, that leads to decreased adult NSPC numbers and precocious neuronal differentiation. Chromatin and transcriptome profiling has identified KMT2D- and HIF1A-regulated gene programs suppressed across KS1 model systems, implicating roles for hypoxia responses in regulating neuronal differentiation. Indeed, we demonstrate KMT2D-dependent HIF1A activation and target gene induction in KS1 neural models, as well as diminished response to hypoxic conditions during in vitro neuronal differentiation in *Kmt2d*$^{+/\beta_{geo}}$ NSPCs. Our findings are consistent with an etiological model for KS1-associated developmental changes in which the loss of KMT2D suppresses oxygen response programs critical for early NSPC maintenance, hence favoring precocious cellular differentiation during hippocampal neurogenesis.

Methods

Media and reagents are listed (Supplementary Table 10).

Animals

The *Kmt2d*$^{+/\beta geo}$ allele (Mll2Gt(RRt024)Byg) was generated by Bay Genomics (University of California) through the random insertion of a gene trap vector. *Kmt2d*$^{+/\beta geo}$ mice were fully backcrossed to C57Bl/6J background (JAX) over more than 10 generations. Animals were housed in a 14-hour light/10-hour dark cycle with free access to food and water. Experiments compare age- and sex-matched littermates. Genotyping by PCR has been described (Bjornsson et al. 2014).

Primary hippocampal NSPCs

Female C57Bl/6J mice (JAX) were mated to *Kmt2d*$^{+/\beta geo}$ males and sacrificed for embryo harvest at embryonic day 18. Micro-dissected DG from *Kmt2d*$^{+/\beta geo}$ and *Kmt2d*$^{+/+}$ littermate embryos was processed for NSPC isolation and in vitro differentiation as described (Bernas et al. 2017).

Patient-derived iPSCs, NSPCs, and fibroblasts

Skin biopsy fibroblasts were cultured from molecularly confirmed KS1 patients (KS1-1, KS1-2, KS1-3). KS1-1 fibroblasts were reprogrammed using non-integrating Sendai virus vectors (CytoTune-iPS 2.0). 5 days post-induction, cells were transferred to mouse embryonic fibroblast (MEF) feeder plates in iPSC media. 21 days post-induction, high quality colonies were manually selected for propagation and karyotyping by G-banding. Generation of healthy control lines (C3-1 and C1-2) was previously described (Wen et al. 2014). Feeder MEFs from E13.5 CF-1 mice were mitotically inactivated by irradiation. iPSCs were enzymatically passaged every 4-8 days using collagenase. NSPCs were induced from iPSCs as previously described (Li et al. 2011), briefly, by

inhibiting glycogen synthase kinase 3 (GSK3), transforming growth factor β (TGF-β), γ-secretase, and Notch signaling pathways using small molecules CHIR99021 (4 μM), SB431542 (3 μM), and Compound E (0.1 μM), in the presence of hLIF (10 ng/ml) and ROCK inhibitor (5 μM) for 7 days. NSPCs were split with Accutase and propagated in neural induction medium on a Matrigel.

CRISPR-Cas9 deletions in HT22 cells

HT22 mouse hippocampal cells are commercially available, but were a gift of the Goff Laboratory and maintained in HT22 media. sgRNAs targeting two loci spanning the *Kmt2d* SET domain-encoding region, with cut sites in exon 52 and either exon 54 ($Kmt2d^{\Delta 1}$) or intron 54 ($Kmt2d^{\Delta 2}$), were integrated into Cas9 plasmid (pSpCas9BB-2A-puro v2.0 (PX459)) and delivered to cells at 20% confluency using Lipofectamine 2000 according to the manufacturer's protocol. After puromycin selection, mutant cells were identified by PCR (primers listed) and clonally expanded. Following Sanger sequencing, a subset of clones appearing heterozygous by PCR, but found to bear strand invasion, were removed from analyses.

RNA-seq in HT22 cells: library preparation

Cells were plated at equal density and sampled at 60% confluency. Total RNA was isolated from three biological replicates of $Kmt2d^{\Delta/\Delta}$ clones and $Kmt2d^{+/+}$ parental cells using Direct-Zol RNA MicroPrep, and libraries were constructed in technical triplicate using NEBNext Poly(A) Magnetic Isolation Module and NEBNext UltraII RNA Library Prep Kit for Illumina, with size selection by AMPure XP beads, according to manufacturer protocols. Library quantification and quality checks were done using KAPA Library Quantification Kit for Illumina, High Sensitivity

DNA Kit on BioAnalyzer, and Qubit dsDNA HS Assay. Paired end 50 bp reads were obtained for pooled libraries using Illumina HiSeq 2500.

RNA-seq in HT22 cells: data analysis

We first obtained a fasta file with all mouse cDNA sequences (Mus_musculus.GRCm38.cdna.all.fa.gz) from Ensembl (http://uswest.ensembl.org/Mus_musculus/Info/Index, version 91, downloaded January 2018). Then, sequencing reads were pseudoaligned to this fasta file and transcript abundances were subsequently quantified, using Salmon (Patro et al. 2017). We then used the tximport R package (Soneson et al. 2015) to convert the transcript abundances into normalized gene-level counts, by setting the "countsFromAbundance" parameter equal to "lengthScaledTPM". Next, we used the edgeR (Robinson et al. 2010; McCarthy et al. 2012) and limma (Ritchie et al. 2015) R packages to log2 transform these gene-level counts, and normalize each of the samples with the "voom" function using the effective library size (that is, the product of the library size and the normalization factors, the latter of which we computed with the "calcNormFactors" function provided in edgeR). Subsequently, we estimated the mean-variance relationship, and calculated weights for each observation. In order to account for the correlation between technical replicates of the same clone when performing the differential analysis, we fit a mixed linear model, using the function "duplicateCorrelation" from the statmod R package (Giner and Smyth 2016) to block by clone. The differential analysis was then performed using the limma R package. Differentially expressed genes were called with 0.05 as the cutoff for the False Discovery Rate (FDR).

When performing the principal component analysis, transcript abundances were first converted into gene-level counts using the tximport R package, with the "countsFromAbundance" parameter equal to "no". Then, we applied a variance stabilizing transformation to these gene-level

counts using the "vst" function from the DESeq2 R package (Love et al. 2014), with the parameter "blind" set to "TRUE", and subsequently estimated the principal components (without scaling the expression matrix) using the 1000 most variable genes.

scRNA-seq: library preparation

NSPCs were induced in parallel from each iPSC line (KS1-1, C1-2, C3-1) under identical conditions, and passaged three times before sampling. iPSCs were detached from MEF feeders using collagenase (200 units/ml). iPSCs and NSPCs were dissociated to single-cell suspension using Accutase. Cell counts and viability were analyzed using Countess II. scRNA-seq libraries were created with Chromium Single Cell 3' Library & Gel Bead Kit v2 (10x Genomics) according to manufacturer protocol. Targeted cell recovery for each sample was 5,000 cells. Sufficient cDNA for library construction was achieved using 20 amplification cycles for iPSC libraries and 16 cycles for NSPC libraries. Sample indexing was achieved using 11 PCR cycles for iPSC libraries and 5 cycles for NSPC libraries. scRNA-seq libraries were sequenced using Illumina NextSeq 500.

scRNA-seq: data analysis

Sequencing output was processed through the Cell Ranger 2.1.0 preprocessing pipeline using default parameters with the exception of --expect-cells=5000 for `cellranger count` and --normalize=none for `cellranger aggr`. Reads were quantified against hg19 using the 10x reference genome and transcriptome builds (refdata-cellranger-GRCh38-1.2.0). The aggregated raw count matrix was then used as input for the Monocle2 single-cell RNAseq framework. Differential gene expression analysis was performed on all NSPCs and iPSCs with respect to genotype (KS1 patient vs healthy control) and was performed using the Monocle2 (Trapnell et al. 2014) likelihood ratio test (0.1% FDR, Monocle2 LRT, Benjamini-Hochberg corrected) with `num_genes_expressed` added as

a nuisance parameter to both the full and reduced models. The directionality of the differential gene test was determined by calculating the mean gene expression across all KS1 patient-derived and healthy control cells respectively, evaluating the relative fold change. High-variance genes were selected as those with a positive residual to the estimated dispersion fit and a mean number of reads per cell >=0.0005. Cell cycle stage was determined by profiling cell cycle associated genes across all cells and assigning cell cycle state using the R/Bioconductor package scran (Lun et al. 2016). Dimensionality reduction and visualization was performed via UMAP (McInnes et al. 2018) on the log10(counts + 1) of the high variance genes in the NSPC dataset. The first 10 principal components were used as input for UMAP using the default parameters of the R/CRAN package umap. Cells were assigned to clusters using Monocle2's implementation of the louvain community detection algorithm. Learned clusters were then aggregated by hand based on marker gene expression into three clusters ("Differentiating", "Transitioning", "Cycling"). Differential gene expression within clusters, and between genotypes was performed as described above. The "Differentiating" cluster was then segregated, and a smooth line was fitted using a linear regression. This line was determined to represent the direction of differentiation by examination of marker genes (Supplementary Figure 3.5C-H). The residuals of this fit were then plotted and deciles were calculated containing equal number of cells along the axis of differentiation. The number of cells in each decile was then counted with respect to genotype.

ChIP-seq: library preparation

Kmt2d$^{+/+}$ HT22 cells were sampled at 70% confluency and processed for pull-down with ChIP-grade KMT2D antibody (Millipore Sigma) according to ENCODE guidelines. Sonicated, reverse-crosslinked chromatin served as input control. Briefly, ~300 million cells per cell line were crosslinked in 1% formaldehyde, quenched with 0.125 M glycine, and cell lysate supernatants were

collected for immediate processing or snap-frozen for storage at -80°C. Nuclei (20 million/sample) were diluted in 1 ml RIPA buffer were sonicated using Bioruptor for 6 cycles of 5 minutes (60 seconds on/30 seconds off) in ice-cold water bath. Supernatants containing sheared chromatin were pre-cleared with Protein A Dynabeads and incubated overnight at 4°C with 8 μg KMT2D antibody. ChIP DNA was recovered by Dynabead incubation (overnight at 4°C plus 6 hours at room temperature) before 6 sequential salt washes of increasing stringency, then eluted and reverse crosslinked overnight at 65°C. DNA was purified using DNA Clean and Concentrator (Zymo Research) and quantified using High Sensitivity DNA Kit on BioAnalyzer, and Qubit dsDNA HS Assay. DNA libraries were constructed using NEBNext UltraII DNA Library Prep Kit for Illumina and quantified using KAPA Library Quantification Kit for Illumina. Paired end 75 bp reads were obtained for pooled libraries using Illumina HiSeq 2500.

ChIP-seq: data analysis

Sequencing reads were aligned to the mouse reference genome (mm10) using Bowtie2 (Langmead and Salzberg 2012). Then, duplicate reads were removed with the function MarkDuplicates from Picard (http://broadinstitute.github.io/picard/). Peaks were subsequently called using MACS2 (Zhang et al. 2008), with the "keep-dup" parameter equal to "all". After peak calling, we excluded all peaks that overlapped with blacklisted regions provided by ENCODE (Amemiya et al. 2019). As a quality metric, using the resulting list of peaks, we computed the fraction of reads in peaks (frip) with the "featureCounts" function in the Rsubread package (Liao et al. 2019), with the "requireBothEndsMapped" parameter equal to "TRUE", and the "countChimericFragments" and "countMultiMappingReads" parameters equal to FALSE. We found frip to be 2.9%, which is within the range of values for a point-source factor (Landt et al. 2012).

To identify genes likely to be regulated in *cis* by KMT2D, we first obtained the coordinates of 10kb regions centered around the TSS for each gene, using the "promoters" function from the EnsDb.Mmusculus.v79 R package (Rainer 2017), with the "filter" parameter equal to "TxBiotypeFilter("protein_coding")", and the "upstream" and "downstream" parameters both equal to 5000. Subsequently, we selected those genes whose extended promoter (+/- 5kb from the TSS) overlapped with at least one KMT2D peak, using the "findOverlaps" function in the GenomicRanges R package (Lawrence et al. 2013).

Purification of EdU$^+$ nuclei

Mice were given 150 mg/kg EdU by intraperitoneal injection and sampled after 16 hours. DG was micro-dissected in ice-cold PBS immediately following sacrifice by halothane inhalation. Total nuclei were purified as described (Rizzardi et al. 2019) with addition of RNase inhibitor to all buffers. Briefly, DG was dounce-homogenized in 1 ml lysis buffer and layered above a sucrose gradient for ultracentrifugation at 28,600 RPM for 2 hours at 4°C. Nuclei were resuspended in Click-iT EdU AlexaFluor-488 with RNAse inhibitor, and incubated 30 minutes at room temperature. Samples were passed through 40 μm filter, stained with 1 μg/ml DAPI, and kept on ice before sorting. Lysates processed identically from non-EdU-injected mice served as negative controls during sorting with Beckman Coulter MoFlo Cell Sorter. Cell cycle analysis by DNA content was performed with gates discriminating 2N and 4N cells by DAPI fluorescence.

RNA-seq: EdU$^+$ nuclei

Purified EdU$^+$ nuclei from 3 *Kmt2d*$^{+/\beta_{geo}}$ and 3 wild-type littermate female mice (500 nuclei pooled per genotype) were sorted into Smart-Seq 2 lysis buffer (2 μL Smart-Seq2 lysis buffer with RNase inhibitor, 1 μL oligo-dT primer, and 1 μL dNTPs), briefly spun by tabletop microcentrifuge,

and snap-frozen on dry ice. Nuclei were processed according to a modified Smart-seq2 protocol (Picelli et al. 2013). Briefly, lysates were thawed to 4°C, heated to 72°C for 5 minutes, and immediately placed on ice. Template-switching first-strand cDNA synthesis was performed using a 5'-biotinylated TSO oligo. cDNAs were amplified using 20 cycles of KAPA HiFi PCR and 5'-biotinylated ISPCR primer. Amplified cDNA was cleaned using 1:1 ratio of Ampure XP beads and approximately 250 pg was input to a one-quarter-sized Nextera XT tagmentation reaction. Tagmented fragments were amplified for 12 enrichment cycles and dual indexes were added to each well to uniquely label each library. Concentrations were assessed with Quant-iT PicoGreen dsDNA Reagent (Invitrogen) and samples were diluted to ~2nM and pooled. Pooled libraries were sequenced on the Illumina HiSeq 2500 platform to a target mean depth of ~8 x 105 bp paired-end fragments per cycle. Paired-end reads were aligned to mm10 using HISAT2 (D. Kim et al. 2015) with default parameters except: -p 8. Aligned reads from individual samples were quantified against a reference genome (GENCODE vM8) using cuffquant (Mudge and Harrow 2015). Normalized expression estimates across all samples were obtained using cuffnorm with default parameters (Trapnell et al. 2012).

RT-qPCR

Total RNA was isolated by RNeasy Mini and cDNA libraries were constructed with High-Capacity cDNA Reverse Transcription Kit (Applied Biosystems) according to manufacturer protocols. Experiments were performed in technical triplicate, with biological replicates as indicated. Probes were from Taqman.

Immunostaining, confocal imaging, and processing

Coronal brain sections of 30 μm (every sixth slice) were analyzed in serial order. Briefly, adult brains were PFA-fixed by transcardial perfusion and post-fixed for 12 hours before cryoprotection by 30% sucrose in phosphate buffer. Brains were sectioned by cryostat (Leica), directly mounted to charged slides, and stored at -80°C. Antigen retrieval (DakoCytomation) was performed at 95°C for 20 minutes. Overnight incubation at 4°C in primary antibodies (Supplementary Table 10) preceded AlexaFluor-conjugated secondary antibody (1:500). Tiled, z-stacked images were acquired using Zeiss LSM780 FCS AxioObserver confocal microscope and Zen software (Zeiss) to encompass entire DG structure. Images were quantified using Imaris (BitPlane) by experimenters blinded to genotype. Cell counts were corrected by DG area multiplied by z-thickness, and expressed as cells/mm^3. For pulse-label experiments, mice were injected with 150 mg/kg EdU in saline every 48 hours and sampled as above. DCX^+ neuroblast distance from SGZ plane was measured in Fiji (NIH). Patient-derived cell imaging utilized EVOS FL Cell Imaging System with analysis in Fiji.

FACS and analysis

Flow cytometry analysis with FACSverse and FACSsuite (BD Biosciences), and sorting by Beckman Coulter MoFlo Cell Sorter with proper gate settings and doublet discrimination (Supplementary Figure 3.3J, Supplementary Figure 3.6A). Runs of 10,000 or more cells were analyzed from technical triplicate culture wells and analyzed in FlowJo v10 (Tree Star Inc). Unstained and secondary-only samples served as control. Cells were sampled after 30-minute pulse of EdU (10 μM) using Click-iT EdU Flow Cytometry Assay (ThermoFisher Scientific). CellTrace Violet and CellEvent caspase-3/7 reagent (ThermoFisher Scientific) were used according to manufacturer protocols. For cycle synchronization, 250 ng/ml nocodazole (Sigma) was applied for 18 hours before release.

Magnetic Resonance Imaging (MRI)

3D T2-weighted MRI (9.4T) was performed in PFA-perfused brains of *Kmt2d*$^{+/\beta geo}$ (n=3) and *Kmt2d*$^{+/+}$ (n=3) female mice aged 4 months. Atlas-based, volume-corrected analysis was performed in 25 brain regions (DtiStudio).

Statistics

For high-throughput experiments, see Methods. For cellular assays, see Figure Legends. Statistical analyses with multiple comparisons correction were done with GraphPad Prism (version 7.0b). Gene set enrichments were determined according to WebGestalt (J. Wang et al. 2017), or by Fisher's Exact Test in R version 3.5.2 as indicated.

Study Approval

All mouse experiments were performed using protocols approved by the Animal Care and Use Committee of Johns Hopkins University School of Medicine and are in accordance with NIH guidelines. Informed consent regarding KS1 patient samples was obtained according to institutional IRB and ISCRO protocols approved by JHU.

Author contributions

GAC and HTB conceived the study; GAC and HTB wrote the manuscript; GAC, HNN, GC, JDR, LZ performed experiments; GAC, LB, JA, KDH and LG analyzed data.

Acknowledgments

HTB is funded through an Early Independence Award from the National Institutes of Health (NIH, DP5OD017877), the Icelandic Research Fund (195835-051), and the Louma G. Foundation. Imaging was performed with NIH support (S10OD016374). Karyotype facility supported by NICHD (1U54 HD079123-01A1). FACS was performed at the Bloomberg School of Public Health. We thank Michael Sherman for assistance with image quantification and Manisha Aggarwal for MRI. Schematics created with Mark Sandusky or Biorender.com. Hongjun Song and Kai Ge provided critical reagents and advice. Hal Dietz and Gregg Semenza provided conceptual guidance.

Data availability

High-throughput data are publicly available. RNA-seq and ChIP-seq: GEO #GSE126167. scRNA-seq: GEO #GSE126027. Scripts for scRNA-seq analysis are available at https://github.com/Jaugust7/Kabuki-Syndrome-scRNA-analysis.

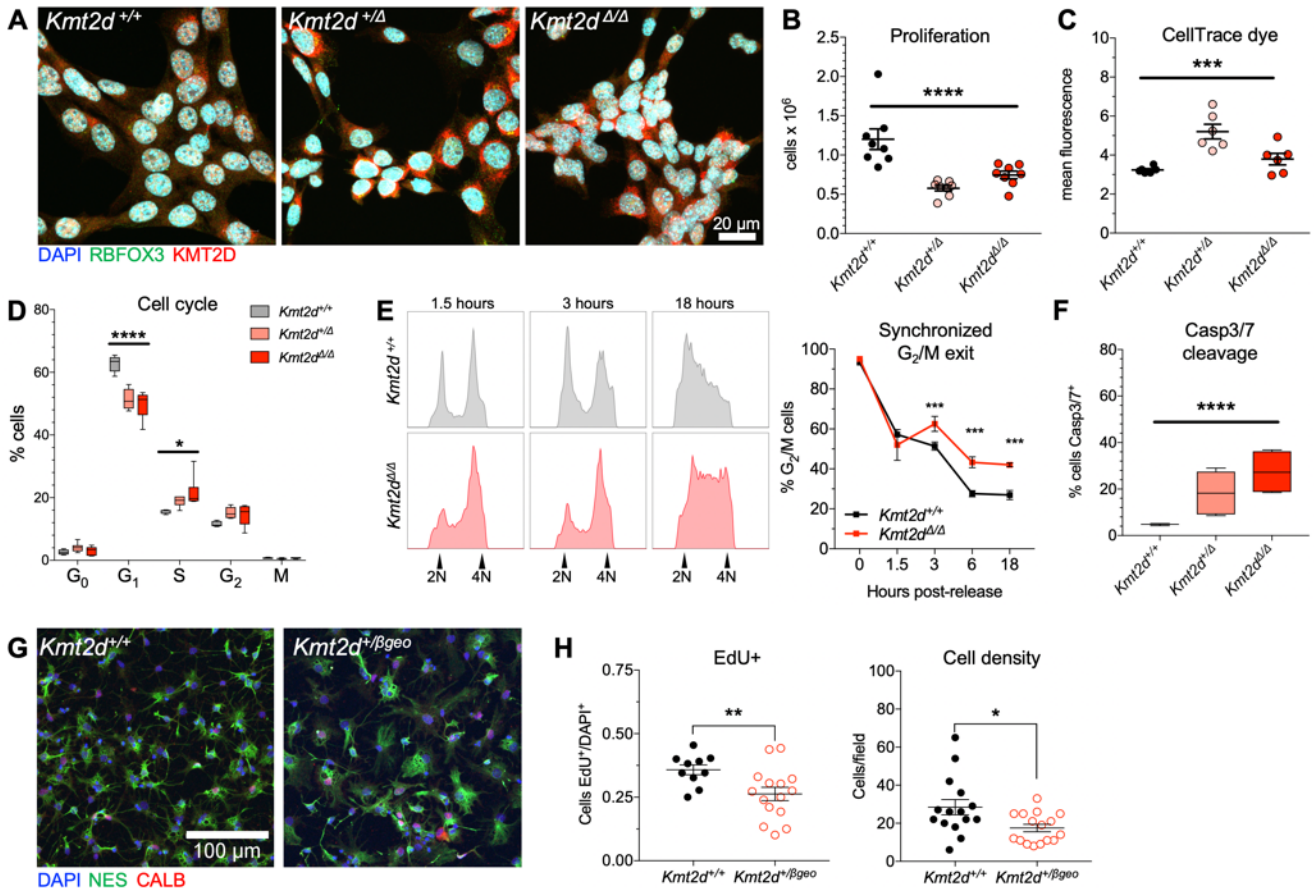

Figure 3.1. Genetic ablation of the *Kmt2d* SET methyltransferase domain disrupts proliferation and cell cycle in a cell-autonomous manner. (**A**) Representative immunostaining against KMT2D and RBFOX3 in *Kmt2d*$^{+/+}$, *Kmt2d*$^{+/\Delta}$, and *Kmt2d*$^{\Delta/\Delta}$ HT22 cells. (**B**) Decreased proliferation in *Kmt2d*-inactivated cells quantified 72 hours after equal density plating. One-way ANOVA. (**C**) Generational tracking reveals fewer cell divisions, i.e. reduced dye dilution, of CellTrace Violet in *Kmt2d*$^{+/\Delta}$ and *Kmt2d*$^{\Delta/\Delta}$ cells at 72 hours. One-way ANOVA. (**D**) Flow cytometric quantification of cell cycle phases using KI67 and DAPI fluorescence. One-way ANOVA for each cycle phase, independently. (**E**) *Kmt2d*$^{+/+}$ and *Kmt2d*$^{\Delta/\Delta}$ cells synchronized and released for analysis of G_2/M exit, by DNA content, up to 18 hours after release, and quantification of cells in G_2/M (technical triplicates per time point). Bars indicate mean ± SEM. Two-way ANOVA ($P<0.0001$) with post hoc multiple comparisons. (**F**) Flow cytometric quantification of early apoptotic cells by caspase-3/7 fluorescence. One-way ANOVA. (**G**) Confocal images of nestin (NES) and calbindin (CALB) expressing primary hippocampal NSPCs from *Kmt2d*$^{+/+}$ and *Kmt2d*$^{+/\beta geo}$ mice, and (**H**) quantified proliferation. Student's t-test. Bars indicate mean ± SEM. Boxes indicate mean ± interquartile range; whiskers indicate minima and maxima. (*$p<0.05$, **$p<0.01$, ***$p<0.001$, ****$p<0.0001$). Scale bars 20 μm (**A**) or 100 μm (**G**).

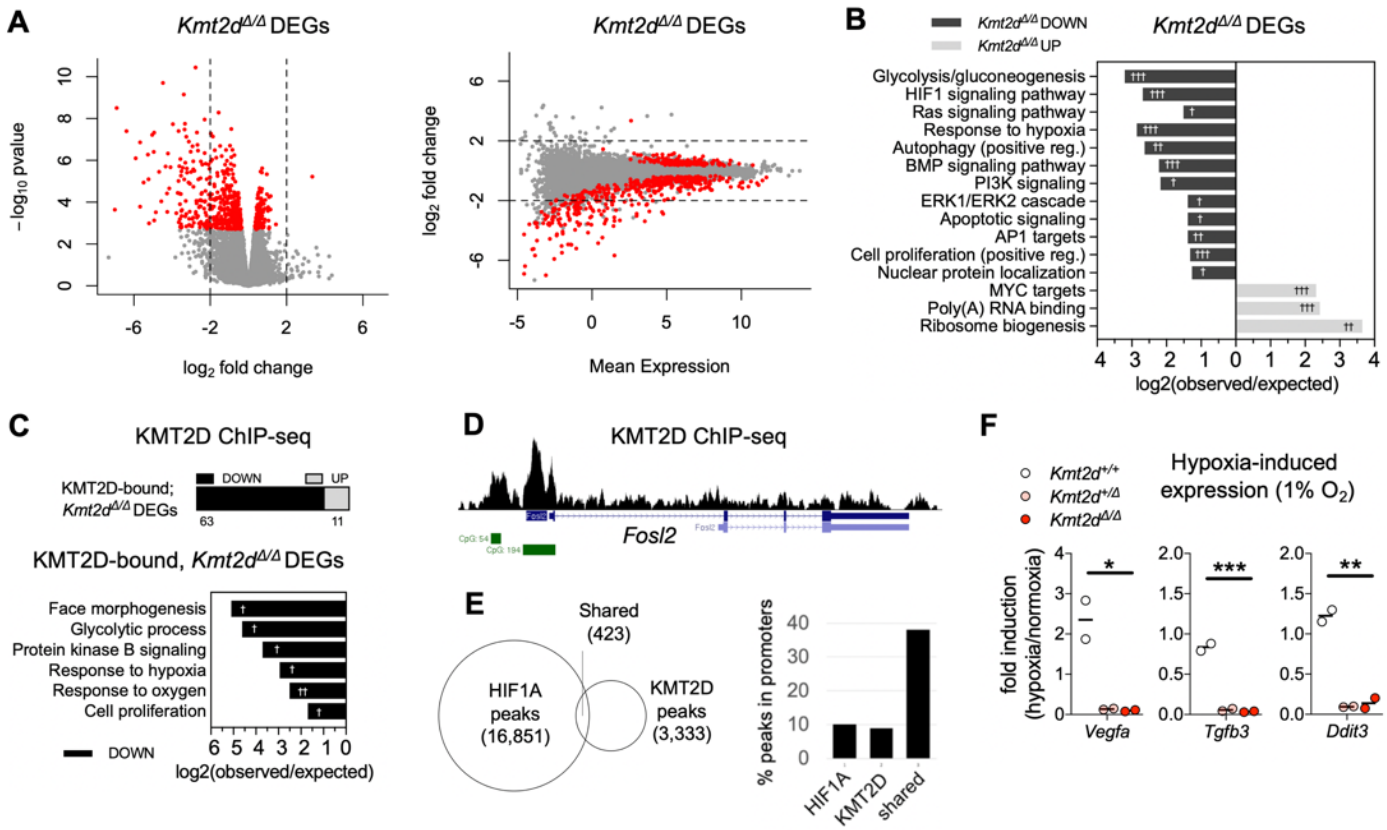

Figure 3.2. Suppressed transcription of KMT2D-regulated hypoxia response genes upon loss of the *Kmt2d* SET methyltransferase domain in neuronal cells. (**A**) Expression analysis by RNA-seq in HT22 cells reveals 575 significant differentially expressed genes (DEGs) in $Kmt2d^{\Delta/\Delta}$ clones (3 biological replicates) relative to $Kmt2d^{+/+}$ cells, each in technical triplicate. Fold changes in expression indicate most significant $Kmt2d^{\Delta/\Delta}$ DEGs (~76%, red dots) are downregulated in $Kmt2d^{\Delta/\Delta}$ cells, plotted against p-value and mean expression. (**B**) Gene networks significantly enriched among down- or up-regulated $Kmt2d^{\Delta/\Delta}$ DEGs. (**C**) $Kmt2d^{\Delta/\Delta}$ DEGs which are also KMT2D-bound, as determined by ChIP-seq chromatin profiling in $Kmt2d^{+/+}$ HT22 cells, and gene networks significantly enriched among KMT2D-bound, $Kmt2d^{\Delta/\Delta}$ DEGs. (**D**) Representative ChIP-seq track of a KMT2D-bound, $Kmt2d^{\Delta/\Delta}$ DEG depicting KMT2D binding peaks (black), RefSeq gene annotations (blue), and CpG islands (green). (**E**) Overlapping loci of observed KMT2D-ChIP peaks in HT22 cells and HIF1A-ChIP peaks in embryonic heart (37). Overlapping KMT2D/HIF1A peak regions, compared to individually bound regions, are enriched at gene promoters. (**F**) RT-qPCR analysis of hypoxia-induced gene expression in $Kmt2d^{+/+}$, $Kmt2d^{+/\Delta}$, and $Kmt2d^{\Delta/\Delta}$ cells, following 72 hours in normoxia (21% O_2) or hypoxia (1% O_2), with fold induction of target gene mRNA. 2 biological replicates per genotype, each in technical triplicate. One-way ANOVA. (*p<0.05, **p<0.01, ***p<0.001). Fisher's Exact Test (†FDR<0.05, ††FDR<0.01, †††FDR<0.001).

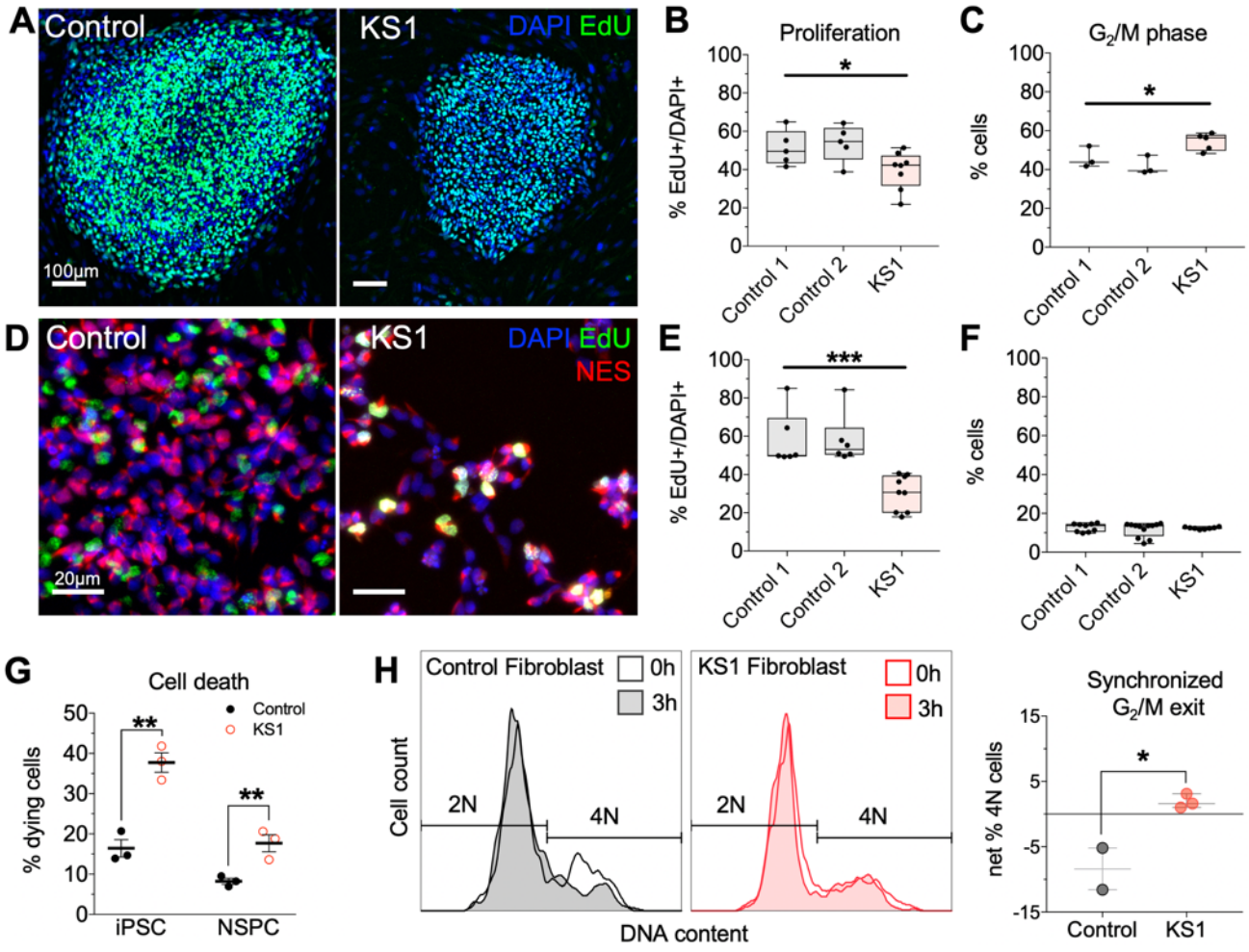

Figure 3.3. KS1 patient-derived cells recapitulate KMT2D-associated defects in proliferation and cell cycle. (**A**) Representative immunostaining of iPSCs derived from a *KMT2D*$^{+/-}$ KS1 patient (c.7903C>T:p.R2635*) and healthy controls. (**B**) Proliferating cells were pulsed with EdU for 30 minutes and quantified by flow cytometry. One-way ANOVA. (**C**) Cell cycle analysis in iPSCs, discriminating 2N and 4N DNA content (G_1/G_0 and G_2/M, respectively) by flow cytometry using DAPI fluorescence. One-way ANOVA. (**D**) Representative immunostaining of NES-expressing NSPCs induced from iPSCs of KS1 patient and controls. (**E**) EdU pulse assay quantified by flow cytometry. One-way ANOVA. (**F**) Cell cycle analysis in NSPCs. One-way ANOVA. (**G**) Quantification of dying cells by flow cytometric scatter profiles in KS1 patient and control cells. Student's t-test. (**H**) Synchronized G_2/M exit analysis by flow cytometry in fibroblasts from KS1 patients (KS1-1, KS1-2, KS1-3) and healthy controls (Controls 3 and 4), in triplicate per cell line. Cells were enriched for G_2/M phase using nocodazole and analyzed by DAPI fluorescence to quantify G_2/M phase cell fractions at 0 and 3 hours after release. Student's t-test. Bars indicate mean ± SEM. Boxes indicate mean ± interquartile range; whiskers indicate minima and maxima. (*$p<0.05$, **$p<0.01$, ***$p<0.001$). Scale bars 100 µm (**A**) or 20 µm (**D**).

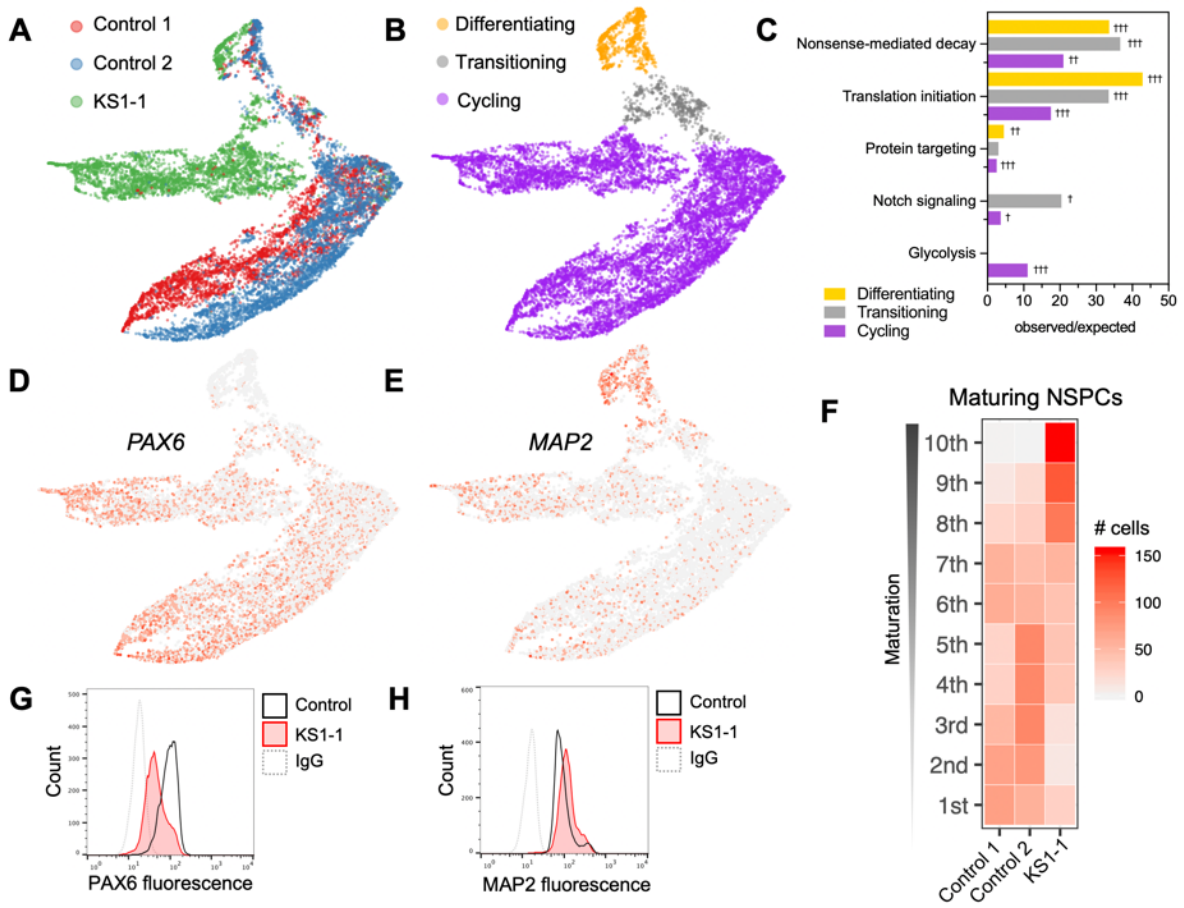

Figure 3.4. Transcriptional suppression of metabolic genes in cycling cells, and precocious neuronal differentiation in KS1 patient-derived NSPCs. (**A**) Single-cell RNA-seq profiling in patient and healthy control iPSC-derived NSPCs (~5,000 cells per patient), with Uniform Manifold Approximation Projection (UMAP) to visualize gene expression differences between cells. (**B**) NSPCs partitioned by maturation stage as defined by stage-specific marker expression, and (**C**) enriched gene networks, analyzed exclusively among DEGs for each NSPC subset (cycling, transitioning, and differentiating). (**D-E**) Representative UMAPs annotated by relative expression intensities of NSPC markers, revealing the maturation trajectory from early NSPCs (*PAX6*$^{+}$) to differentiating NSPCs (*MAP2*$^{+}$). (**F**) Heatmap comparing density of NSPCs along the maturation trajectory, defined by binned marker expression from earliest (1st) to most differentiated (10th) deciles, with KS1 cells disproportionately occupying the most mature bins. (**G-H**) Protein-level experimental validation of marker expression differences by flow cytometry in NSPCs from KS1 patient and controls, plotting fluorescence intensities of PAX6 and MAP2. Fisher's Exact Test (†FDR<0.05, ††FDR<0.01, †††FDR<0.001).

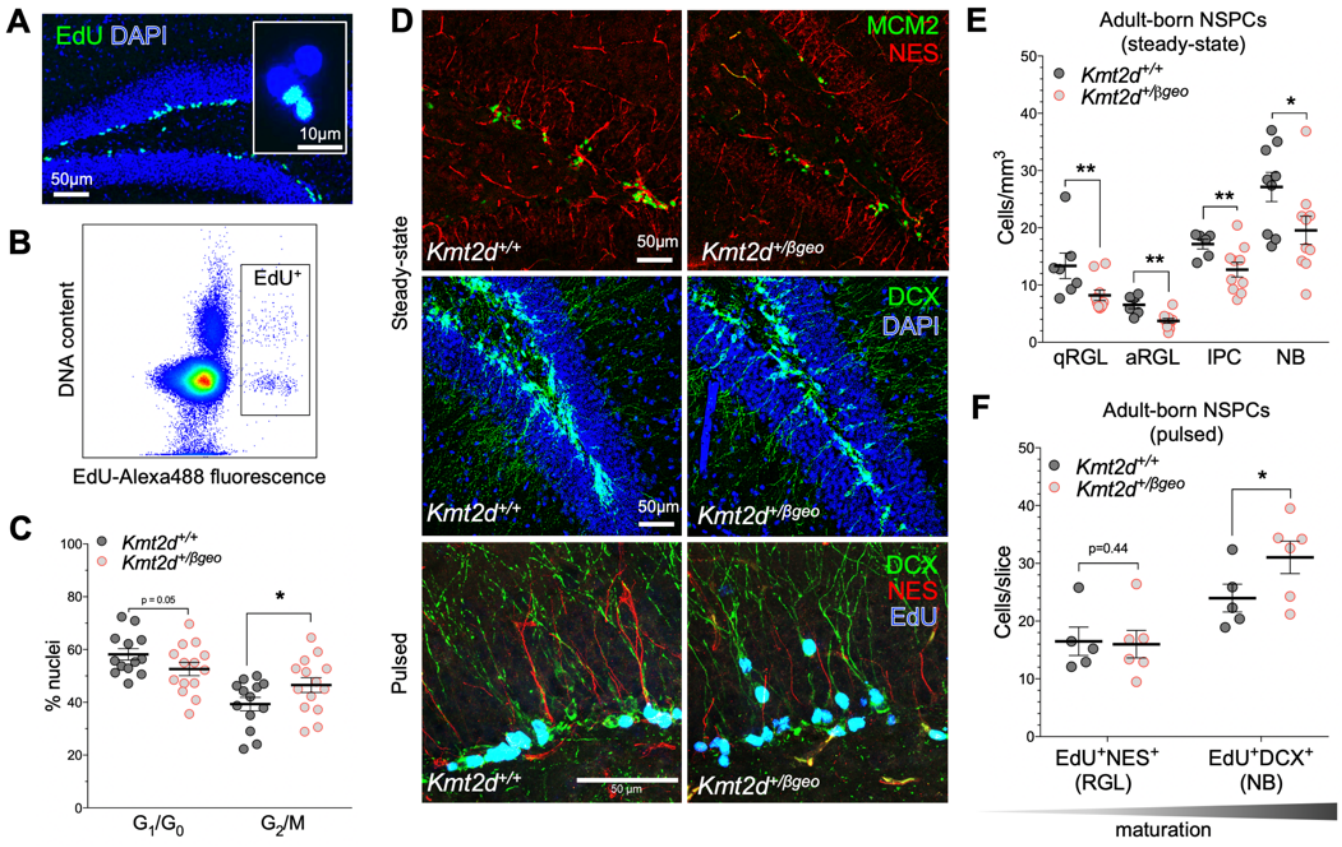

Figure 3.5. In vivo defects of neurogenesis and NSPC differentiation in a *Kmt2d*$^{+/\beta geo}$ mouse model of KS1

(**A**) Immunostaining images of dividing (EdU-pulsed) dentate gyrus (DG) NSPCs, and nuclei purified from micro-dissected DG by fluorescence-activated cell sorting (FACS) (**B**) of labeled nuclei. (**C**) Cell cycle analysis in purified EdU$^+$ DG nuclei from *Kmt2d*$^{+/+}$ and *Kmt2d*$^{+/\beta geo}$ mice sampled 16 hours post-pulse, using DAPI fluorescence (13-14 mice per genotype, 200-500 nuclei per mouse). (**D**) Representative confocal immunostaining of neurogenesis markers in the DG of adult *Kmt2d*$^{+/+}$ and *Kmt2d*$^{+/\beta geo}$ mice at steady-state (6-10 mice per genotype, 7-10 z-stack images per mouse) or after EdU pulse (5-6 mice per genotype, 10 z-stack images per mouse). NES$^+$ radial glia-like (RGL) NSPCs, in either quiescent (MCM2$^-$) or activated (MCM2$^+$) states (qRGL and aRGL, respectively), MCM2$^+$NES$^-$ intermediate progenitor cells (IPCs), and DCX$^+$ neuroblasts (NB) were quantified. (**E-F**) Quantification of stage-specific NSPC densities (qRGL, aRGL, IPC, and NB) in adult *Kmt2d*$^{+/+}$ and *Kmt2d*$^{\beta/geo}$ mice at steady-state (**E**) or after EdU pulse-chase (2 weeks) to birthdate differentiating NSPCs (**F**). Bars indicate mean ± SEM. Student's t-test (*p<0.05, **p<0.01, ***p<0.001). Scale bars 50 μm, unless specified (**A**, inset, 10 μm).

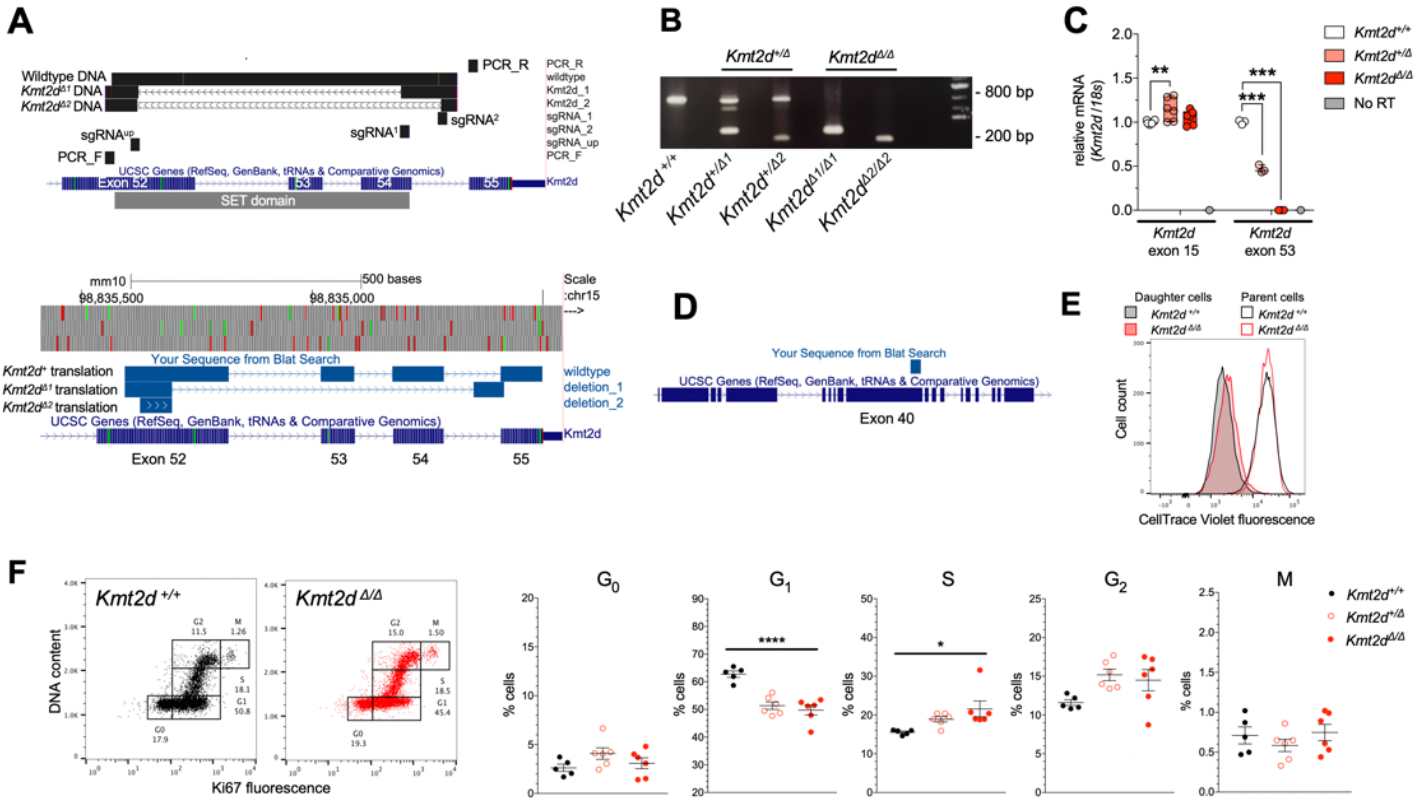

Supplementary Figure 3.1. CRISPR-targeted HT22 cells. (**A**) Sanger-sequenced DNA of wild-type (*Kmt2d*$^{+}$) and targeted (*Kmt2d*$^{\Delta}$) alleles in HT22 cells, mapped with sgRNAs and PCR primers, to *Kmt2d* locus (mm10) on chromosome 15. Mapping of Sanger-sequenced DNA after in silico translation to predict amino acid sequences illustrates premature termination codons (PTC) created in *Kmt2d*$^{\Delta 1}$ and *Kmt2d*$^{\Delta 2}$ alleles. (**B**) PCR with probes flanking sgRNA cut sites identifies experimental cell lines (*Kmt2d*$^{+/\Delta}$ and *Kmt2d*$^{\Delta/\Delta}$) compared to wild-type (*Kmt2d*$^{+/+}$). (**C**) RT-qPCR analysis of mRNA using probes spanning upstream exons (15-16) or exons within the deletion site (53-54). Two-way ANOVA with post hoc multiple comparisons. (**D**) Mapped peptide sequence of KMT2D antibody (Sigma). (**E**) Flow cytometric CellTrace fluorescence after 72 hours in HT22 cells. Increased intensity indicates less dye dilution, i.e. fewer cell divisions in mutants (left). Parental cell data confirm genotype-independent dye uptake (right) at 0 hours. (**F**) Cell cycle gating by flow cytometric analysis using Ki67 and DAPI to discriminate individual stages (G_0, G_1, S, G_2, M) in *Kmt2d*$^{+/+}$ and *Kmt2d*$^{\Delta/\Delta}$ cells, and quantification of each cycle phase. One-way ANOVA. Bars indicate mean ± SEM. Boxes indicate mean ± interquartile range; whiskers indicate minima and maxima. (*p<0.05, **p<0.01, ***p<0.001, ****p<0.0001).

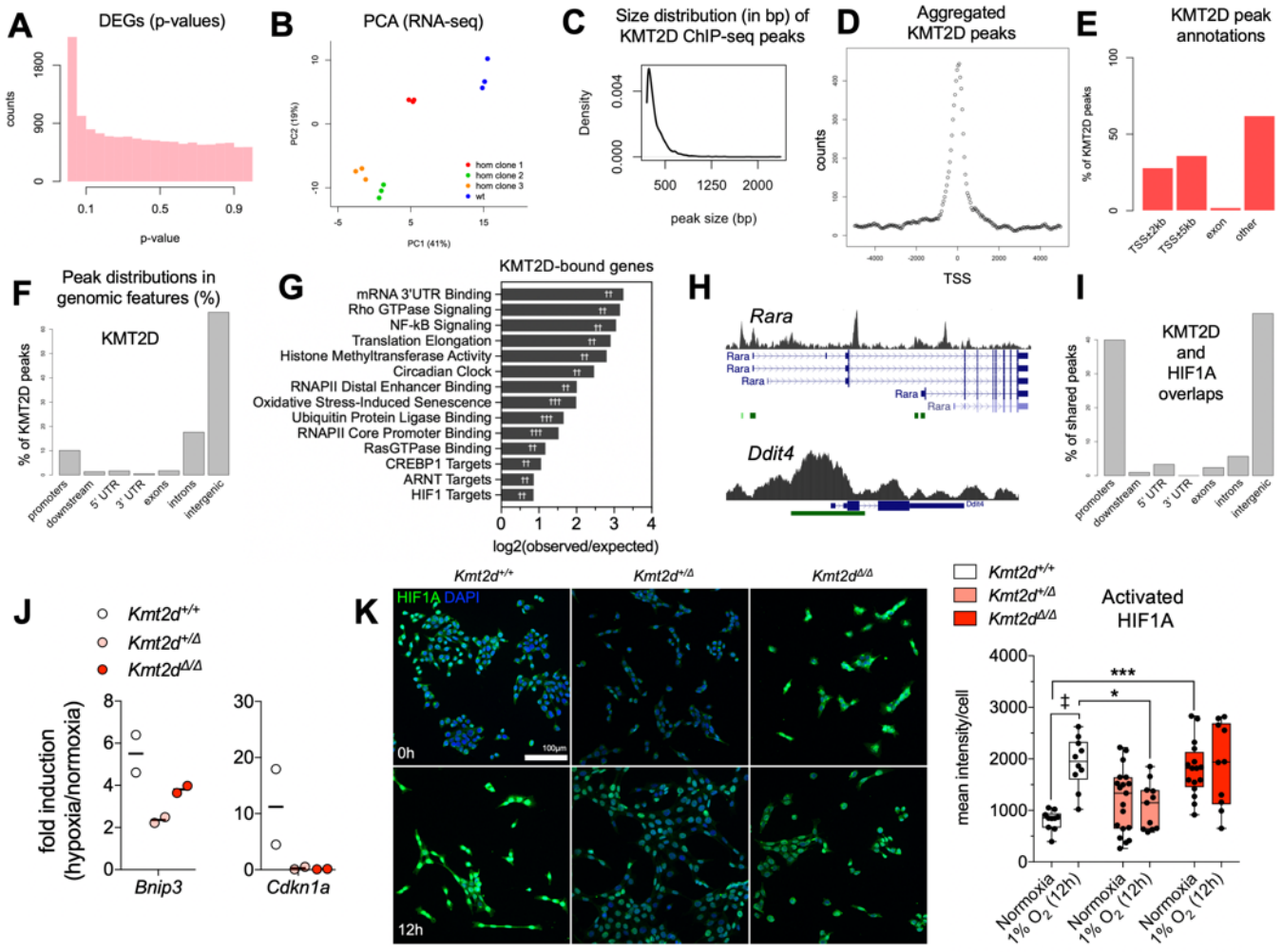

Supplementary Figure 3.2. HT22 cell RNA-seq and ChIP-seq analysis. (**A**) P-value distribution in *Kmt2d*$^{\Delta/\Delta}$ DEGs relative to wild-type indicates a well-calibrated test. (**B**) PCA visualizing clear expression differences in wild-type and *Kmt2d*$^{\Delta/\Delta}$ HT22 cells. (**C**) The size distribution (in bp) of KMT2D ChIP-seq peaks. (**D**) Validation of KMT2D peak distributions about gene TSSs and (**E-F**) genomic features. (**G**) Gene networks showing highest fold change in enrichment among genes proximal to KMT2D peaks (TSS±5 kb). Fisher's Exact Test (†FDR<0.05, ††FDR<0.01, †††FDR<0.001). (**H**) KMT2D peaks clustered at alternate TSSs of *Rara* gene and enhancer-like peaks at *Ddit4* gene. (**I**) Genomic features at overlapping KMT2D and HIF1A (37) ChIP-seq peaks. (**J**) RT-qPCR analysis of hypoxia-induced gene expression in HT22 cells, upon 1% O_2 exposure. One-way ANOVA (n.s.). (**K**) HIF1A nuclear fluorescence, i.e. activation, analysis. Representative z-stacked confocal images are shown with quantifications of nuclear HIF1A fluorescence. Two-way ANOVA with post hoc multiple comparisons (significance from wild-type, *p<0.05, **p<0.01, ***p<0.001; and from baseline, ‡p<0.01). Boxes indicate mean ± interquartile range; whiskers indicate minima and maxima. Scale bar 100 μm.

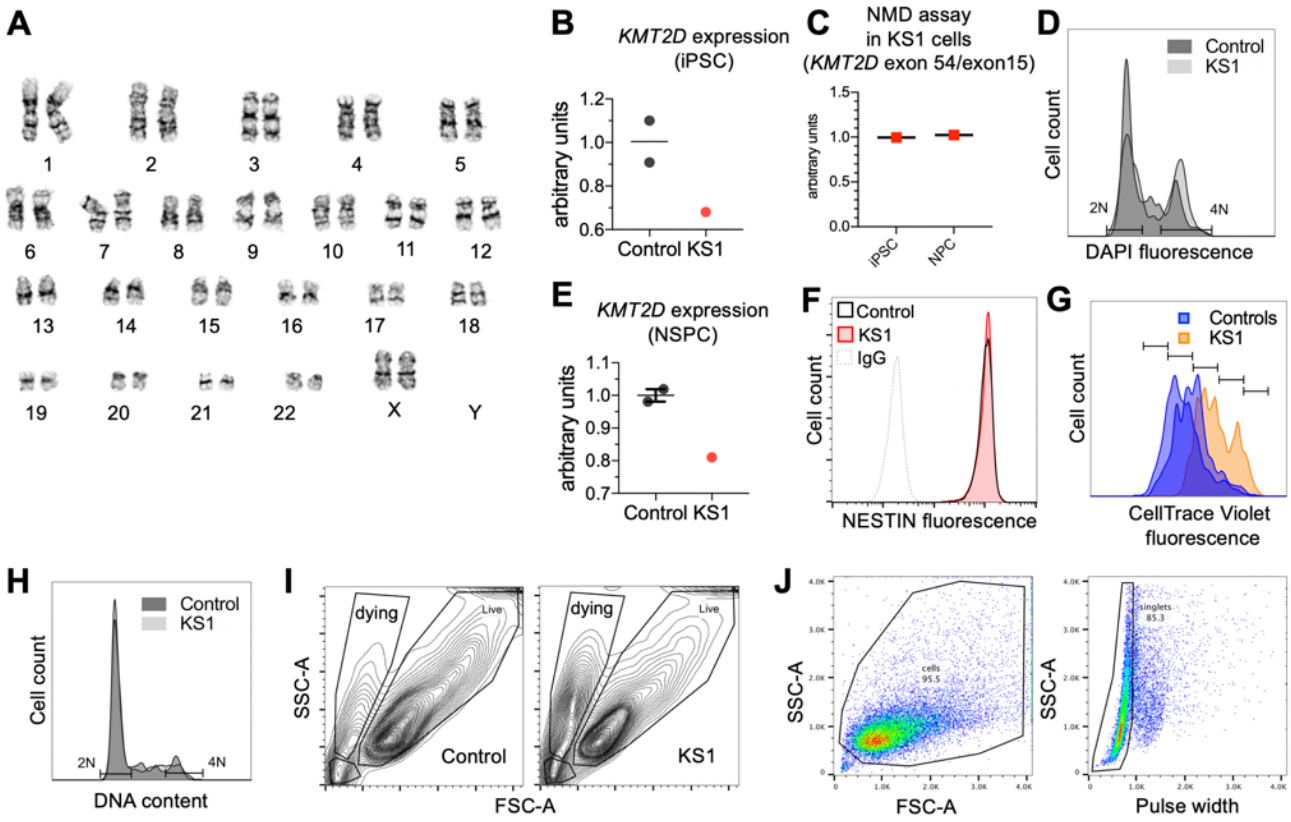

Supplementary Figure 3.3. iPSC and NSPC line validations and additional phenotyping. (**A**) 46, XX normal female karyotype in KS1-1 iPSCs. (**B**) RT-qPCR analysis of *KMT2D* (exon 15) expression in KS1 iPSCs compared to two healthy control iPSC lines (C1-2 and C3-1). Dots represent average of technical triplicates per patient line. Bars indicate mean. (**C**) RT-qPCR demonstrating equivalent exonic ratios of *KMT2D* exon 15 to exon 54, measured in technical triplicate, consistent with NMD of the entire transcript. (**D**) Flow cytometric analysis of DNA content by DAPI fluorescence in iPSCs. (**E**) RT-qPCR analysis of *KMT2D* (exon 15) expression in NSPCs derived from the KS1 and control iPSC lines, measured in technical triplicate. (**F**) Flow cytometric analysis of NES fluorescence intensity in KS1 and control NSPCs. (**G**) CellTrace Violet generational tracking showing fewer divisions (i.e. higher dye intensity) in patient-derived NSPCs over 72 hours. (**H**) Flow cytometric analysis of DNA content by DAPI fluorescence in NSPCs. (**I**) Sample flow cytometric gating for detection of scatter profiles indicative of cell death-associated cellular condensation. (**J**) Representative gating of viable cells and doublet discrimination in immunofluorescence-based flow cytometric analyses of iPSCs and NSPCs.

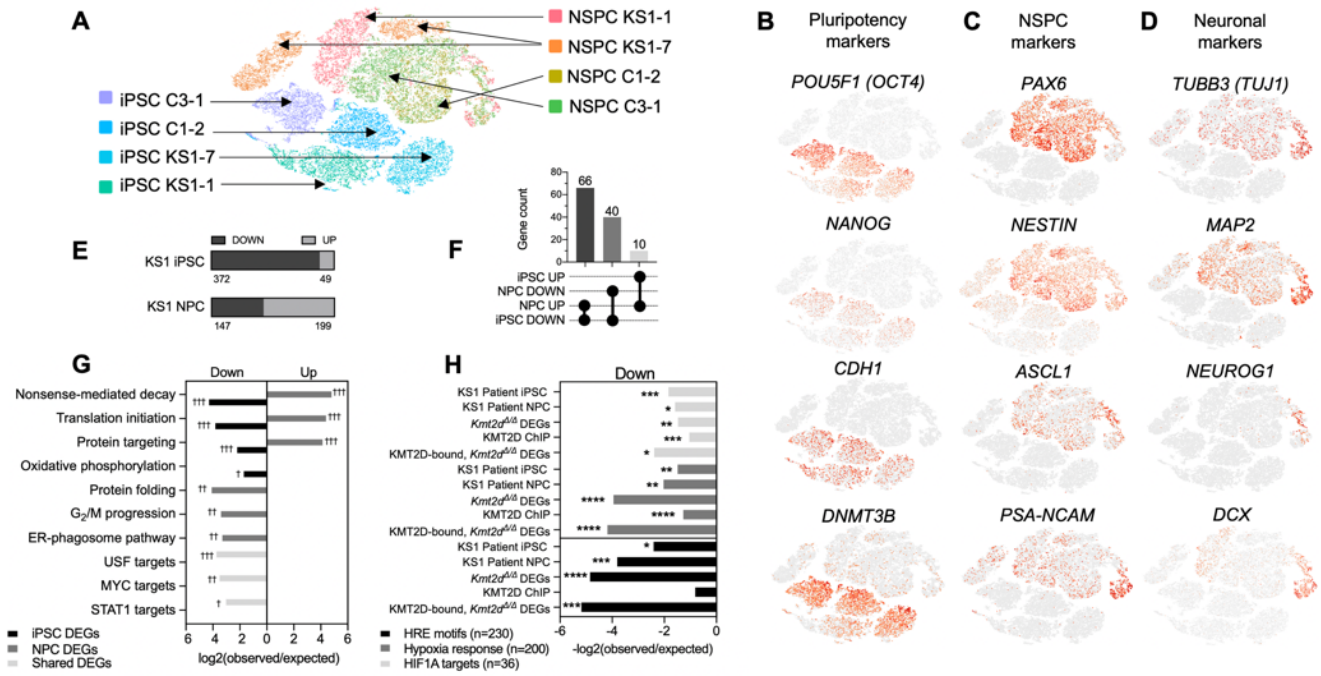

Supplementary Figure 3.4. iPSC and NSPC single-cell RNA-seq analysis. (**A**) t-stochastic neighbor embedding (tSNE) representation of iPSC and NSPC libraries sequenced on 10XGenomics platform. Cell clusters colored by cell type and patient ID. iPSCs and NSPCs derived from patient K1-7 were excluded from downstream analysis due to abnormal karyotype. (**B-D**) Representative tSNE of iPSC, NSPC, and neuronal markers demonstrating expected cell identities and revealing a gradient of cell maturation. (**E**) Proportions of DEGs down- or up-regulated in KS1 patient iPSCs or NSPCs compared to respective healthy controls, (**F**) DEG lists intersected for overlaps among down-regulated and up-regulated genes, and (**G**) Gene networks most enriched among differentially expressed genes (DEGs) in KS1 patient iPSCs and NSPCs relative to respective healthy controls, and DEGs shared in both cell types. (**H**) Significant enrichments of Hypoxia Response genes, HIF1A Direct Target genes, and genes containing the Hypoxia Response Element (HRE) RCGTG motif among observed DEGs in KS1 Patient iPSCs, KS1 Patient NSPCs, *Kmt2d*$^{\Delta/\Delta}$ HT22 cells, as well as KMT2D-bound genes in wild-type HT22 cells, and KMT2D-bound, down-regulated genes in *Kmt2d*$^{\Delta/\Delta}$ HT22 cells). Fisher's Exact Test (*p<0.05, **p<0.01, ***p<0.001; †FDR<0.05, ††FDR<0.01, †††FDR<0.001).

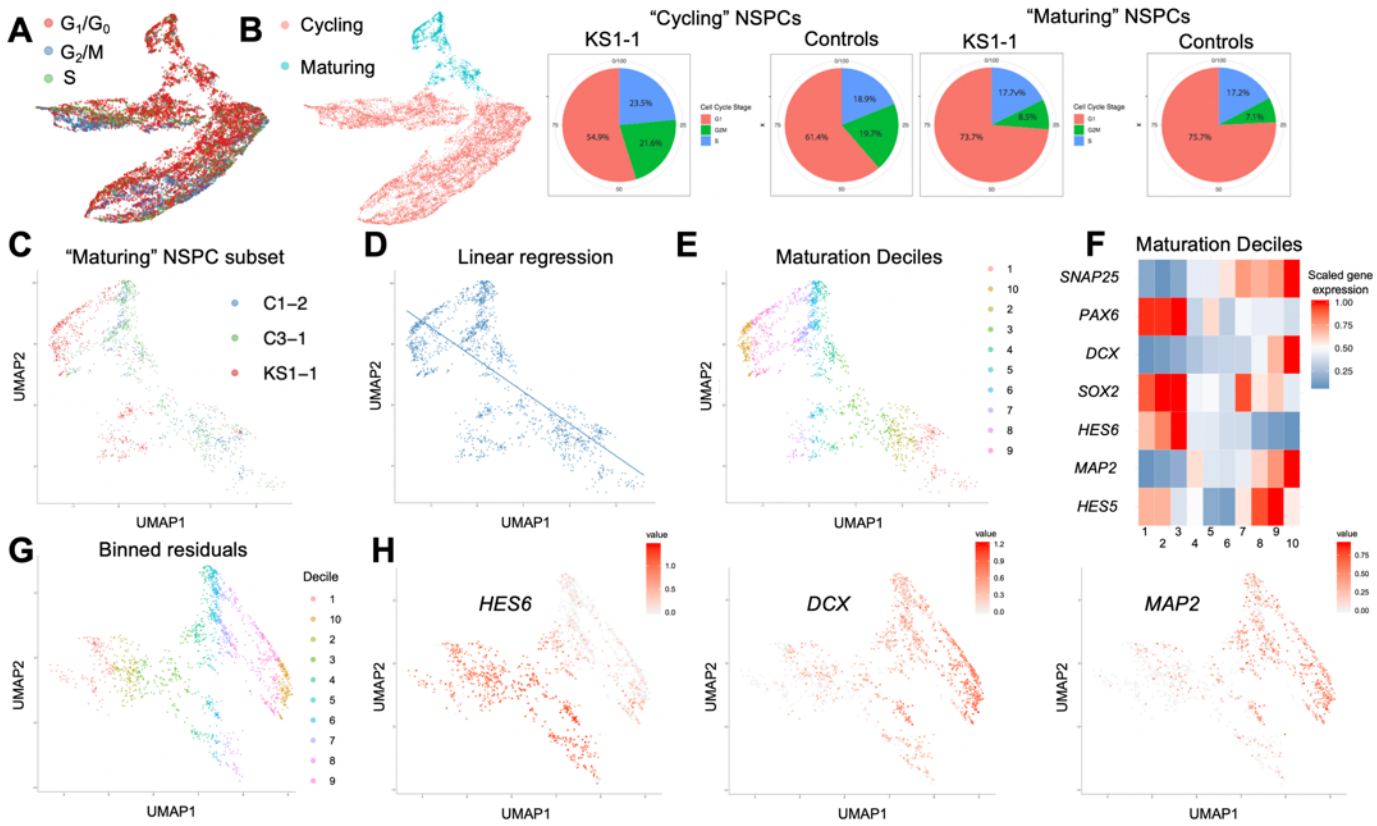

Supplementary Figure 3.5. Stratified scRNA-seq analysis of NSPCs. Uniform Manifold Approximation Projection (UMAP) of single-cell NSPC libraries partitioned by (**A**) cell cycle marker expression into subsets of G_1/G_0, S, and G_2/M cells, used for cycle phase-stratified differential expression analysis to rule out confounding differences in cell cycle phase composition on NSPC transcriptome comparisons. (**B**) Subset of "Cycling" versus non-cycling, "Maturing" NSPCs, which includes "Transitioning" and "Differentiating" cells as defined (Figure 4B), and UMAP-based cell cycle occupancies consistent with experimental FACS data (Figure 3F). (**C-H**) UMAP analysis of Differentiating NSPCs displaying (**C**) library patient ID's, (**D**) smooth linear regression fitted to define the maturation trajectory and (**E**) binned deciles of progressively maturing cells along the regression. (**F**) Relative expression of selected NSPC markers defining directionality of the maturation trajectory. (**G**) Binned residuals used to calculate deciles containing equal number of cells along the axis of differentiation. (**H**) Representative NSPC marker expression plotted over binned residuals.

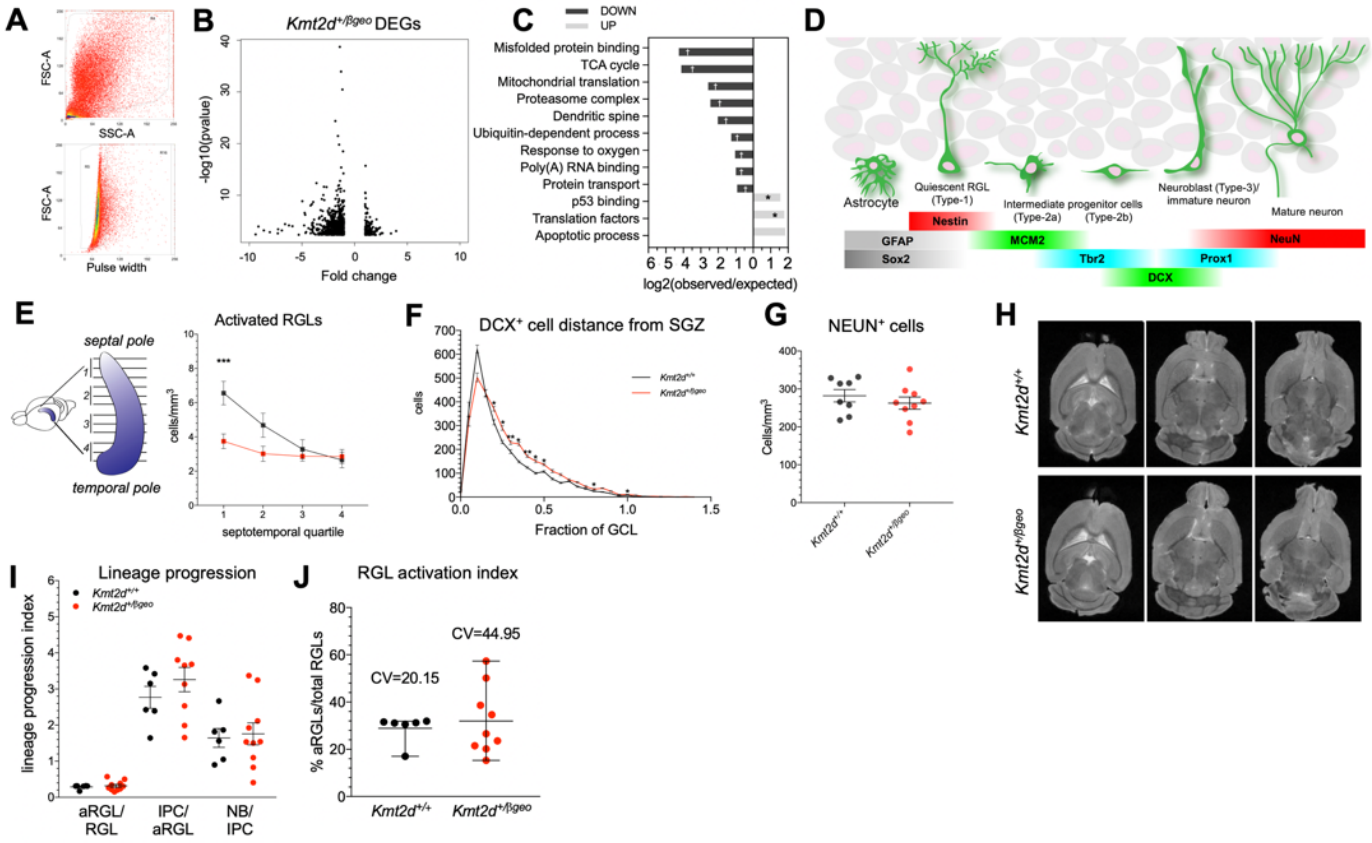

Supplementary Figure 3.6. Phenotyping of *Kmt2d*$^{+/\beta geo}$ mice. (**A**) Sample FACS gating for viable nuclei and doublet discrimination during purification of cycling EdU^{+} nuclei purified from *Kmt2d*$^{+/+}$ and *Kmt2d*$^{+/\beta geo}$ mice at 16 hours post-EdU pulse for RNA-seq and cell cycle analysis. (**B**) RNA-seq analysis of differential gene expression in purified EdU^{+} DG nuclei from *Kmt2d*$^{+/+}$ and *Kmt2d*$^{+/\beta geo}$ mice. (**C**) Gene networks most enriched among DEGs down- or up-regulated in *Kmt2d*$^{+/\beta geo}$ nuclei, showing transcriptional suppression of cellular metabolic pathways. Fisher's Exact Test (†FDR<0.05, ††FDR<0.01, †††FDR<0.001). (**D**) Schematic depicting marker expression during sequential stages of adult DG neurogenesis. (**E**) Serial ordering of perfusion-fixed brain slices enables anatomically-stratified analysis of neurogenesis, for quantification of activated RGL NSPC density along the septotemporal axis of the DG in *Kmt2d*$^{+/+}$ and *Kmt2d*$^{+/\beta geo}$ mice, indicating preferential disruption at the septal DG. Two-way ANOVA with post hoc multiple comparisons. (**F**) Quantification of DCX^{+} NB cell body distance from SGZ plane in 8-week-old mice (9-10 mice per genotype, >1,000 cells per mouse). Two-way ANOVA with post hoc multiple comparisons. (**G**) Quantification of RBFOX3/NEUN^{+} mature DG neurons in 8-week-old mice (8-9 mice per genotype, 10 z-stacks per mouse). Student's t-test (n.s.). (**H**) Sample images of T2-weighted MRI (9.4T) in PFA-fixed brains of female mice 4 months old. (**I**) Comparison of lineage progression index, an approximation of expansion potential for each cell type transition, indicates absence of genotype-associated blockages at any particular cell-type transition analyzed, and (**J**) increased Coefficient of Variance (CV) in RGL activation rates in *Kmt2d*$^{+/\beta geo}$ mice. Bars indicate mean ± SEM. (*p<0.05, **p<0.01, ***p<0.001).

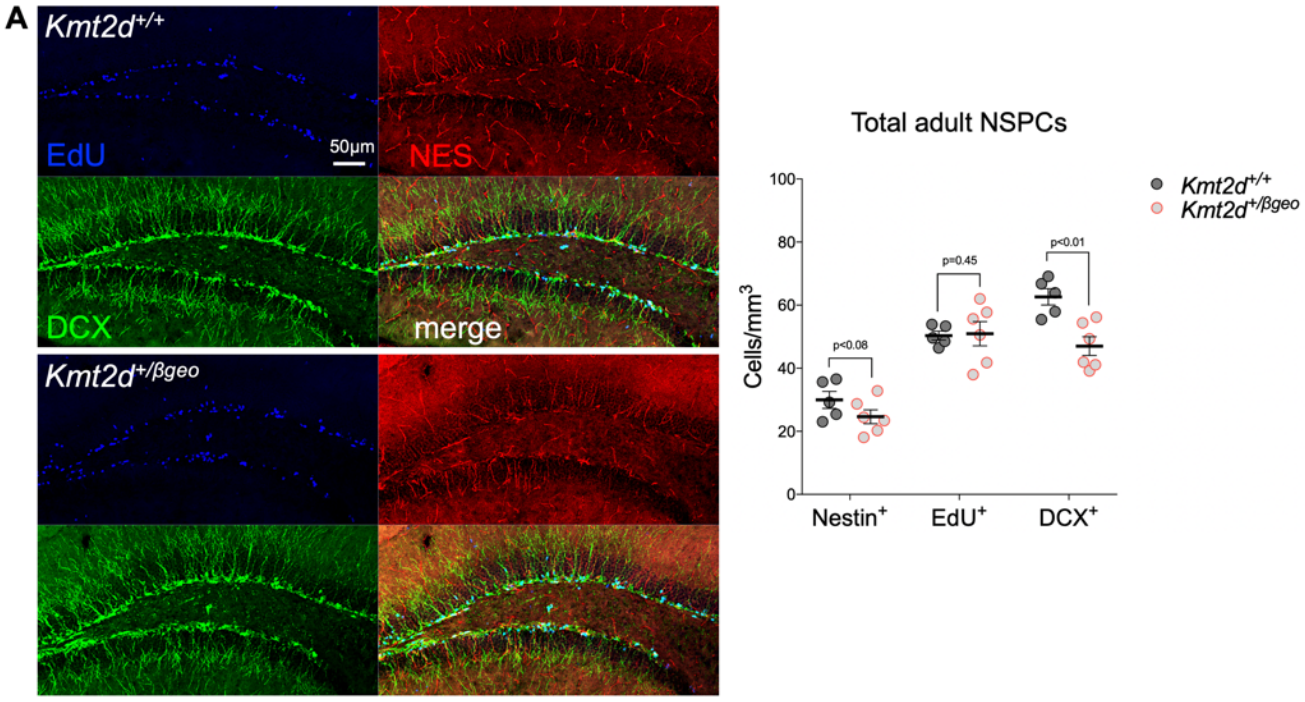

Supplementary Figure 3.7. Pulse-labeling to birth-date adult-born NSPCs in vivo. (**A**) Representative immunostaining from *Kmt2d*$^{+/+}$ and *Kmt2d*$^{+/\beta geo}$ mice (5-6 mice per genotype, 10 z-stacks per mouse) of EdU pulse-labeled cells extending a NES^{+} process (early RGL NSPCs) or DCX^{+} process (maturing NB NSPCs), showing the entire DG area quantified. Steady-state quantification of NSPCs and EdU-labeled NSPCs, confirming steady-state reduction of adult neurogenesis in *Kmt2d*$^{+/\beta geo}$ mice, despite their increased number of EdU^{+}DCX^{+} double-labeled NBs in the same experiment (Figure 5E-F). Bars indicate mean ± SEM, Student's t-test. Scale bar 50 μm.

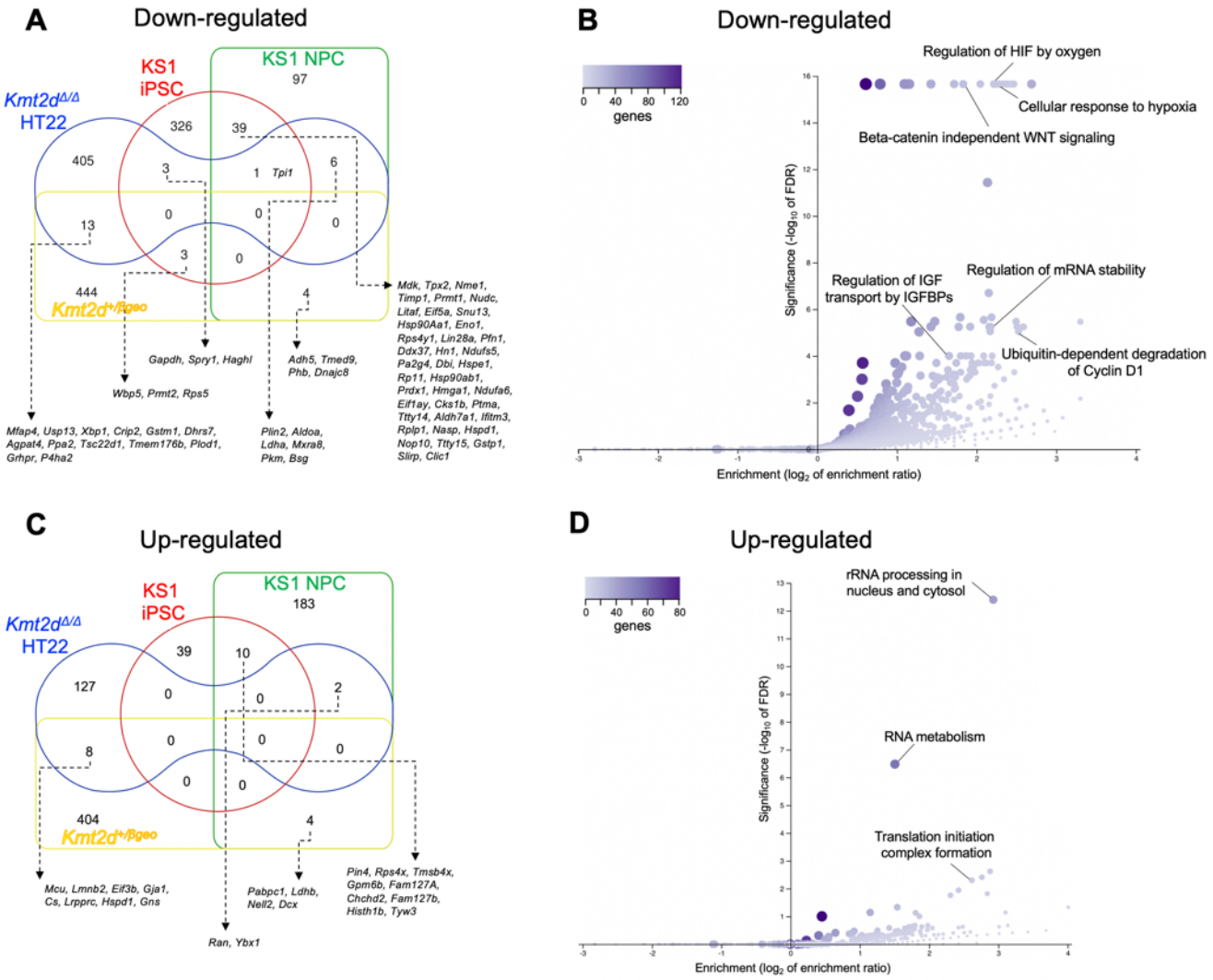

Supplementary Figure 3.8. Comparison of gene expression across KS1 models. (**A-B**) Euler diagram depicting shared transcriptional downregulation in KS1 models with individual genes (**A**) and pathways enriched among down-regulated genes from all KS1 models presently studied (**B**). (**C-D**) Euler diagram depicting transcriptional upregulation in KS1 models with individual genes (**C**) and pathways enriched among up-regulated genes from all KS1 models presently studied (**D**). Enrichments expressed as $\log_2$ of enrichment ratio. Significance expressed as $-\log_{10}$ of FDR. (WebGestalt).

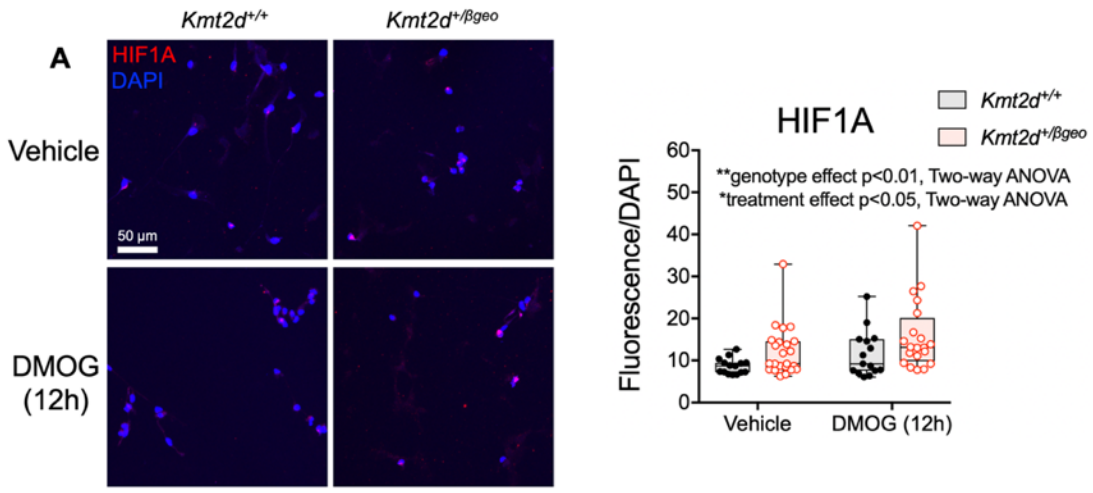

Supplementary Figure 3.9. HIF1A activation in primary hippocampal NSPCs. (**A**) Representative confocal images of primary hippocampal NSPCs isolated from micro-dissected DG of *Kmt2d*$^{+/+}$ and *Kmt2d*$^{+/\beta geo}$ mice, with quantification for analysis of HIF1A fluorescence inside the nucleus (DAPI^{+} volume). Two-way ANOVA with post-hoc multiple comparisons. (*p<0.05, **p<0.01, ***p<0.001). Boxes indicate mean ± interquartile range; whiskers indicate minima and maxima. Scale bar 50 µm.

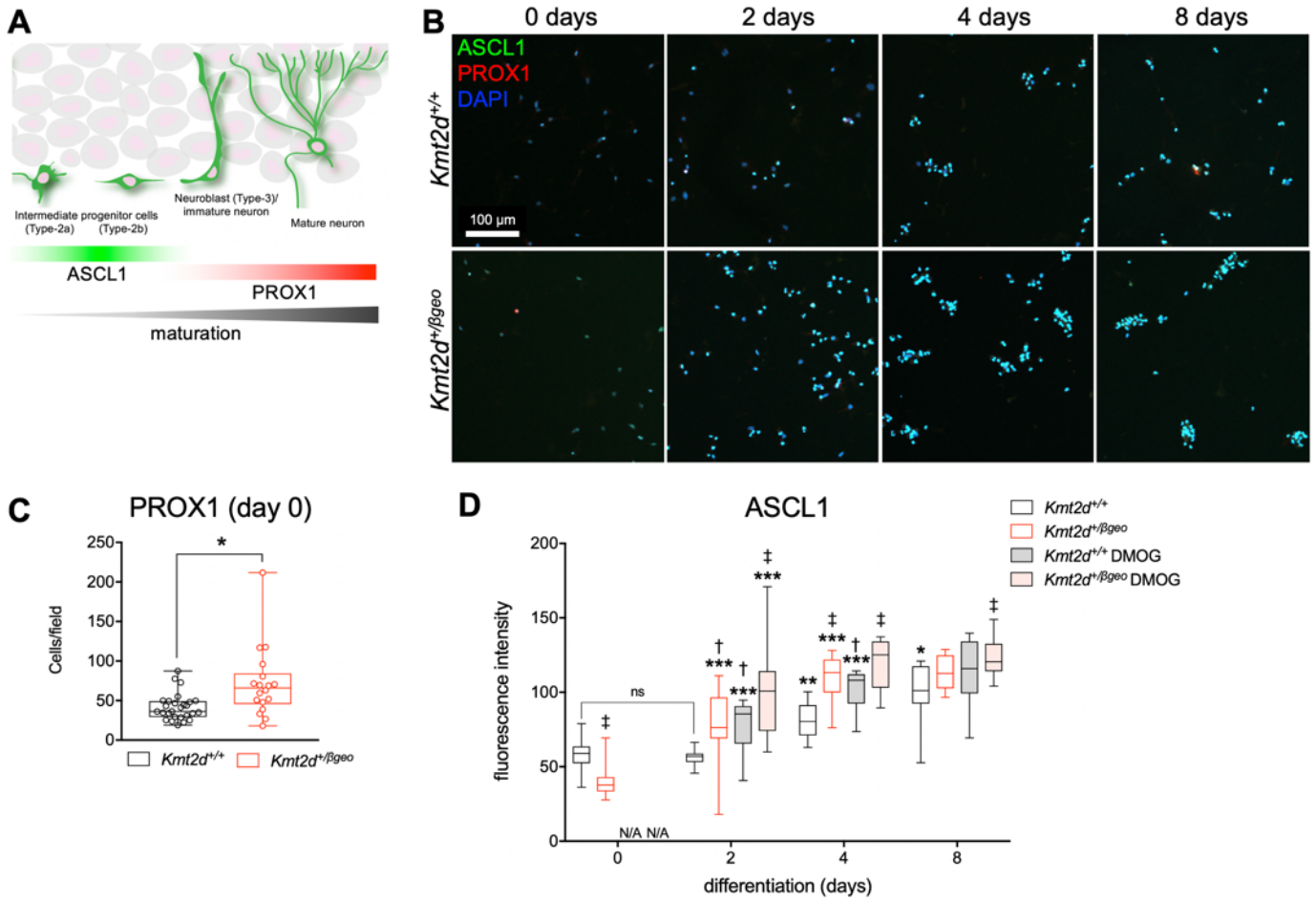

Supplementary Figure 3.10. Precocious in vitro differentiation of primary hippocampal NSPCs. (**A**) Schematic depicting developmental expression of pro-neural transcription factor ASCL1 and maturing neuronal marker PROX1 in adult-born DG neurons. (**B**) Representative confocal images for analysis of NSPCs differentiating between 0 and 8 days in primary hippocampal NSPCs isolated from micro-dissected DG of *Kmt2d*$^{+/+}$ and *Kmt2d*$^{+/\beta geo}$ mice, with quantifications (**C-D**). 22,307 cells analyzed individually across 176 fields of view. Two-way ANOVA with post hoc multiple comparisons. Boxes indicate mean ± interquartile range; whiskers indicate minima and maxima. (significance from previous time point *p<0.05, **p<0.01; ***p<0.001; significance from vehicle-treated wild-type †p<0.05, ‡p<0.01). Scale bar 100 μm.

CHAPTER 4: NEUROGENESIS DEFECTS IN A KS2 MOUSE MODEL

NEUROGENESIS DEFECTS IN A KS2 MOUSE MODEL

Introduction

KDM6A (alternatively known as *UTX*) mutations account for a small fraction of KS patients (KS2), but the resultant physical features (facial profile, fetal fingerpads, postnatal growth retardation) and cognitive delays are clinically indistinguishable from those of *KMT2D*-associated KS1. This was evident prior to the discovery of the first KS gene (*KMT2D*), when these patients were considered the same disease entity. A member of the MLL3-4/COMPASS-like protein complex that includes KMT2D and other proteins, the Jumonji-C (JmjC) domain-containing enzyme KDM6A was initially described as an enhancer-specific H3K27 demethylase, which mediated removal of the H3K27me3 repressive mark (Swigut and Wysocka 2007). Recent studies have elucidated novel, roles for KDM6A which include conversion of inactive enhancers to an active state (via recruitment of KMT2D)and histone acetyltransferase P300/CBP (S.-P. Wang et al. 2017)) as well as oxygen sensing independent of HIF1A (Chakraborty et al. 2019).

Previous studies of a *Kdm6a*-deficient mouse demonstrated spatial memory and learning defects akin to those we observed in $Kmt2d^{+/\beta geo}$ mice, as well as aberrant dendrite development and synapse formation (Tang et al. 2017). Therefore, given that the enzymatic functions of KMT2D and KDM6A both favor open chromatin states and their overlapping clinical phenotypes, we hypothesized that a mouse model of KS2 would also demonstrate a profile of AHN in the DG with NSPC reductions similar to those we found in $Kmt2d^{+/\beta geo}$ mice. We also thought that the similarities in gene expression studies from the two models might identify critical target genes that play a role in the disease pathogenesis. Here, I compare our findings in a KS2 mouse model with those found in the KS1 model. Where applicable, I also reference previous results ($Kmt2d^{+/\beta geo}$ mice) as described in Chapter 3 and in *Carosso et al., 2019*. Briefly, we find that *Kdm6a*-deficient mice, like $Kmt2d^{+/\beta geo}$ mice, exhibit similar depletion of early-stage NSPCs in the DG. In addition, at later stages of neurogenesis,

we find an endophenotypic divergence of AHN between KS1 and KS2 models. Like KS1 models, KS2 models downregulate their cellular metabolism genes regulating glycolysis and mRNA metabolism. Furthermore, because NSPC proliferation is regulated in part by the inhibitory neurotransmitter γ-aminobutyric acid (GABA), we sought to evaluate the effects of GABA inhibition on neurogenesis in KS2 mice.

Our major finding is that KS1 and KS2 models have analogous AHN, cell cycle, and transcriptional abnormalities, implicating these defects in the etiology of KS.

Results

Neurogenesis defects in a KS2 mouse model

To disrupt *Kdm6a* function, we utilized the EUCOMM "knockout first" allele construct (74), in which a hypomorphic *Kdm6a* allele (*Kdm6a*^{tm1a}) can be directly converted to a constitutive null allele (*Kdm6a*^{tm1b}), or converted by flippase to restore wild-type, albeit floxed, *Kdm6a* expression levels (*Kdm6a*^{tm1c}), followed by germline-active CMV-Cre expression to excise the floxed 3rd exon, generating mice with heterozygous loss of *Kdm6a* transcript by nonsense-mediated decay (*Kdm6a*$^{+/tm1d}$ mice); these mice are analogous to either haploinsufficiency or hemizygosity of X-linked KDM6A in male and female KS2 patients, respectively (Supplementary Figure 4.1A). The heterozygous loss of the *Kdm6a* transcript was verified by qRT-PCR (Supplementary Figure 4.1B). As in KS2 patients, adult *Kdm6a*$^{+/tm1d}$ mice exhibit morphological phenotypes including postnatal growth restriction and craniofacial abnormalities compared to wild-type littermates (Supplementary Figure 4.1C-D). Hemizygous male *Kdm6d*$^{tm1d/y}$ mice showed high embryonic lethality, as previously described (Welstead et al. 2012).

To characterize the effects of *Kdm6a* loss on adult neurogenesis, we used confocal microscopy and immunostaining against stage-specific markers (Figure 4.1A-B, Supplementary

Figure 4.1E) to compare abundance of DGC precursors in the SGZ of mice 8-10 weeks old, comparing mutants to sex- and age-matched wild-type littermates. We first verified that *Kmt2d*$^{+/\beta geo}$ mice did not show sex-specific differences confounding comparisons to *Kdm6a*$^{+/tm1d}$ females, and that neurogenic gradients along the septo-temporal axis followed expected patterns (Supplementary Figure 4.1F-G). Quiescent type-1 radial glia-like cells (qRGLs), defined as cells with Nestin-expressing radial morphology but not expressing mini-chromosome replication marker 2 (MCM2) (Nestin$^+$/MCM2$^-$), were less numerous in both *Kmt2d*$^{+/\beta geo}$ and *Kdm6a*$^{+/tm1d}$ mice (38.5% and 40.2%, respectively) compared to respective wild-types (Figure 4.1C-D), thus depletion of the stem cell niche was seen in both KS1 and KS2 mouse models. Activated type-1 RGLs (aRGLs), that is, NSPCs being recruited mitotically toward neurogenesis, were defined as SGZ cells with both Nestin-expressing radial morphology and MCM2$^+$ nuclei (Nestin$^+$/MCM2$^+$), indicating entry into the mitotic cycle, and showed similar reductions of 42.9% and 33.3%, respectively, in *Kmt2d*$^{+/\beta geo}$ and *Kdm6a*$^{+/tm1d}$ mice. Interestingly, while mean RGL activation rates (i.e. % of activated RGLs among total RGLs) did not differ between groups, the variance in rates among individual *Kmt2d*$^{+/\beta geo}$ mice was significantly greater (Bartlett's test, $p<0.05$, n=6-9 per group) (Figure 4.1E), with a coefficient of variation more than double those of wild-type and *Kdm6a*$^{+/tm1d}$ groups.

Unexpectedly, MCM2$^+$ type-2 cells, or Nestin-negative transit-amplifying intermediate progenitor cells (IPCs), showed diametrically opposite trends in representation between models; *Kmt2d*$^{+/\beta geo}$ mice had a ~26% reduction while *Kdm6a*$^{+/tm1d}$ mice had a ~22% increase. In doublecortin (DCX$^+$) Type-3 neuroblasts (NBs), the divergence was even greater: ~28% decrease in *Kmt2d*$^{+/\beta geo}$ and ~36% increase in *Kdm6a*$^{+/tm1d}$. Measurement of NB migration and size yielded additional divergences between *Kmt2d* and *Kdm6a* loss. NBs in *Kmt2d*$^{+/\beta geo}$ mice were located a ~28% greater distance from the SGZ inner boundary, but did not differ in size (Figure 4.1F). In contrast, NB cell bodies in *Kdm6a*$^{+/tm1d}$ mice did not differ in distance, but were found to be marginally smaller (~6%,

$p<0.05$). Thus, despite similar decreases of early NSPC types (activated and quiescent RGL NSPCs) in both KS1 and KS2 mouse models, we observe *Kdm6a*$^{+/tm1d}$-specific increases in IPC and NB stage cells, opposite the effect seen in *Kmt2d*$^{+/\beta geo}$ mice. Moreover, RT-qPCR analysis of the pro-neural factors brain-derived neurotrophic factor (*Bdnf*) and insulin-like growth factor 2 (*Igf2*) demonstrated elevated expression levels in *Kdm6a*$^{+/tm1d}$ mice, again consistent with increased neuronal maturation in the KS2 model (Supplementary Figure 4.1G).

From these results, we conclude that KS1 and KS2 models are phenotypically concordant in their depletion of early-stage NSPCs, i.e. "dormant" cells available for context-dependent recruitment, in the adult DG stem cell niche. Furthermore, we found evidence, by IF and RT-qPCR, consistent with precocious neuronal maturation in *Kdm6a*$^{+/tm1d}$ NSPCs reminiscent of differentiation phenotypes we previously observed in KMT2D-deficient KS1 models.

Cell cycle defects in a KS2 mouse model

NSPC cell cycle is regulated, at least in part by PcG and TrxG enzymes, and influences cell fates in mammalian neurodevelopment (Schuettengruber et al. 2017). This raises the possibility that loss of TrxG activity from KS mutations may impact adult neurogenesis through alterations in cell cycle regulation. To interrogate this, we performed cell cycle analysis in EdU$^+$ DG nuclei by flow cytometry. Nuclei were designated as "early-S" or "late-S/G_2" by virtue of DNA content, and quantified. A "sub-G_1" gate, indicating apoptotic cells, was included as the majority of proliferative precursors undergo apoptosis in healthy animals. Compared to wild-type littermates, *Kdm6a*$^{+/tm1d}$ mice showed fewer cells in early-S and late-S/G_2, and more sub-G_1 cells (Figure 4.2A). Conversely, *Kmt2d*$^{+/\beta geo}$ mice showed opposite trends with more cells in late-S/G_2 and fewer Sub-G_1 cells (Figure 4.2B). Late-S/G_2 arrest showed substantially higher variance among *Kmt2d*$^{+/\beta geo}$ mice compared to all other groups, mirroring their increased variance in RGL activation frequencies (Figure 4.1C).

Thus, we describe analogous cell cycle defects in KS2 and KS1 model systems. Interestingly, *KMT2D* and *KDM6A* gene expression patterns during cell cycle, analyzed among CycleBase data (Santos et al. 2015) appear to be regulated in a temporally complementary manner: specifically, increased expression of KDM6A during a gap of KMT2D expression, observed in late G_1 phase (Supplementary Figure 4.2A).

Gene expression profiling in KS2 NSPCs

Two major obstacles make expression profiling in the adult SGZ niche a challenge: its minute size, as a narrow band only one- to three-cells thick within the GCL, and considerable cell-type heterogeneity. The latter raises a need to profile individual cells to capture distinct molecular profiles among NSPCs, which are scattered along a continuum of activation, proliferation, and differentiation, yet typical methods employ marker-based enrichment that restricts analysis to cells within a defined stage. We therefore adapted a method for unbiased capture of proliferating pulse-labeled cells in the DG (Habib et al. 2016) to interrogate differentially expressed genes (DEGs) in NSPCs of *Kdm6a*-deficient mice using both bulk and single-cell resolution experiments. Total nuclei were purified from EdU-pulsed, micro-dissected DG of 8-week-old mice, and EdU^+ nuclei were sorted using fluorescence-activated cell sorting (FACS) (Figure 4.3A-B) before being subjected to a modified Smart-seq2 protocol (Picelli et al. 2013) for expression profiling by RNA-seq.

To facilitate comparison of overall transcriptional profiles in KS1 and KS2 DG NPCs, we isolated identical numbers of EdU^+ nuclei (n=500) purified from *Kmt2d*$^{+/\beta geo}$ mice (n=3) and wild-type littermates (n=3), and *Kdm6a*$^{+/tm1d}$ mice (n=3) and wild-type littermates (n=3), and first performed bulk RNA-seq. Among 465 genes downregulated in KS1 and 412 genes downregulated in KS2 (Figure 4.3C-D), the 24 shared genes reveal enrichment for mitochondrial membrane and oxidative phosphorylation (fold enrichment 9.9, $p < 6.51 \times 10^{-4}$), DNA damage checkpoint regulation

(fold enrichment >100, $p < 4.31x10^{-3}$), cell cycle progression (fold enrichment >100, $p < 6.46x10^{-3}$), regulation of depolarization (fold enrichment >100, $p < 7.53x10^{-3}$), and ribonucleoprotein complex (fold enrichment >100, $p < 8.60x10^{-3}$). Collectively, RNA-seq experiments in KS1 and KS2 models demonstrate significant dysregulation of cellular metabolism and cell cycle regulating genes shared across both models (Supplementary Figure 4.2B).

The expected breadth of NSPC type heterogeneity comprising the proliferating EdU^+ cell population, prompted us to evaluate gene expression profiles at the single-cell level. EdU^+ nuclei were isolated under identical conditions to the previous bulk experiments, and libraries were prepared from individually-sorted nuclei. Differential expression analysis revealed a greater number of genes downregulated (down, n=769) versus upregulated (up, n=169) (Figure 4.3E). Interestingly in KS2, which exhibited over-proliferation of NPCs, the downregulated gene of highest significance, Nedd4 interacting family protein 1 (*Ndfip1*) ($p < 9.6x10^{-170}$), is a negative regulator of cell proliferation in addition to roles supporting dendritic growth (Howitt et al., 2015). The downregulated gene of second greatest significance was Geminin (*Gmnn*) ($p < 3.3x10^{-160}$), a critical cell fate-determining factor regulating DNA replication timing and genome stability in actively proliferating cells which interacts extensively with PcG and TrxG epigenetic factors (Patmanidi et al., 2016). We next performed over-representation analysis (ORA) among downregulated genes in bulk RNA-seq and scRNA-seq experiments on KS2 EdU+ NSPCs (Figure 4.3F-G), identifying significant enrichment of genes regulating glycolysis, mitochondrial metabolism, and mRNA processing. Notably, these categories were also prominent among downregulated pathways in KS1 mouse and human models (Chapter 3).

Differential response to GABA antagonism in KS2 NSPCs

KS patients exhibit a 10-40% propensity for seizures, therefore the observed enrichment of neuronal depolarization and dendritic growth genes among KS2 DEGs prompted interrogation of NSPC responses *in vivo* to perturbations of neuronal signaling. GABA signaling is traditionally considered for its inhibitory role in neuronal transmission, regulating excitation-inhibition balance in neuronal circuits, but specialized roles have recently been discovered for GABA in regulating early NSPC activation (Song et al. 2013). To determine whether DG NSPCs of a KS2 mouse model respond differentially to local GABA cues *in vivo*, we treated *Kdm6a*$^{+/+}$ and *Kdm6a*$^{+/tm1d}$ mice with the $GABA_A$-R antagonist picrotoxin (PTX) systemically for two weeks. Histological analyses (Figure 4.4A) confirmed previous reports of increased NSPC proliferation by $GABA_A$-R antagonism in wild-types (Tozuka et al. 2005), however type-2 NSPCs of *Kdm6a*$^{+/tm1d}$ mice responded in the opposite direction with reductions in both activated RGLs (Figure 4.4B) and type-2 NSPCs (Figure 4.4C) upon treatment. Thus, DG NSPCs of KS mice showed directionally opposite responses to $GABA_A$-R antagonism, compared to wild-type littermates. These findings demonstrate in vivo perturbation of excitation-inhibition balance mechanisms in *Kdm6a*$^{+/tm1d}$ NSPCs, providing functional support to our detected transcriptional defects in cellular depolarization and synaptic signaling genes in the DG of a KS2 mouse model.

Discussion

Together, results in *Kdm6a*$^{+/tm1d}$ mice reveal genotype-specific differences, relative to wild-type littermates, in phenotypes that differed also in *Kmt2d*$^{+/\beta geo}$ mice, relative to wild-type littermates: namely AHN, cell cycle, and metabolic gene expression. Nonetheless, within these phenotypes, we identified some endophenotypic differences between the *Kdm6a*$^{+/tm1d}$ and *Kmt2d*$^{+/\beta geo}$ contexts. While increased numbers of late-stage NSPCs in *Kdm6a*$^{+/tm1d}$ mice could be consistent with the phenotype of precocious neuronal maturation we previously observed in KMT2D-deficient KS1 models, pulse-

chase experiments will be needed to accurately profile differentiation rates in this KS2 mouse model. Nonetheless, RT-qPCR analysis of pro-neural factors demonstrated elevated expression levels in *Kdm6a*$^{+/tm1d}$ mice, again consistent with increased neuronal maturation in the KS2 model. Most importantly, these experiments demonstrate that the depletion of early NSPCs, i.e. quiescent and activated RGLs, is common to both KS1 and KS2 mouse models. Thus, strategies that favor stem cell maintenance over neuronal maturation could provide therapeutic benefit by replenishing the adult hippocampal niche.

Compared to gene expression profiles in KS1 models (Chapter 3), the present KS2 gene expression profiles implicate perturbation of shared cellular metabolism pathways, namely in glycolysis genes and mRNA metabolism genes. Thus, similar dysregulation of KMT2D and KDM6A metabolic gene targets may underlie the shared KS-associated defects observed in DG neurogenesis and cell cycle phenotypes in NSPCs. Strikingly, it was recently found that the KDM6A enzyme exhibits direct oxygen-sensing properties that are coupled to control of chromatin and cell fate (46), providing a KDM6A-dependent link between hypoxic states and cell differentiation. Because cells undergoing hypoxic responses predominantly favor glycolytic metabolism programs, our findings of disrupted hypoxia responses in KS1, as well as glycolytic disruption in KS2, suggest that dysregulation of hypoxia-responsive cellular states may provide a shared molecular basis for neurodevelopmental defects in KS1 and KS2 etiology.

Emerging relationships between chromatin state-dependent transcription and genome duplication, during S-phase, are found to influence proliferation and lineage commitment in dividing eukaryotic progenitors (Göndör and Ohlsson 2009). In mammalian NSPCs, cell cycle tempo is strictly regulated and regulates cell fate determination during neocortical development. Furthermore, findings that PcG transcriptional repressors govern NSPC cycle tempo, by dynamic modification of chromatin structure during corticogenesis (Pilaz et al. 2016; Hirabayashi et al. 2009), raise the

possibility that loss of TrxG activity, e.g. KMT2D or KDM6A in KS, may impact adult neurogenesis in part through alterations in cell cycle regulation. Here, we found that DG NSPCs of both KS1 and KS2 mouse models exhibit phenotypes of altered S/G_2 phase occupation. Interestingly, S/G_2 phase enrichment was higher in KMT2D-deficient cells, but lower in KDM6A-deficient cells, compared to respective wild-type controls. One interesting hypothesis is that these diametrically-opposing S-phase distributions, in *Kmt2d*$^{+/\beta geo}$ and *Kdm6a*$^{+/tm1d}$ mice, could be linked to the observed divergence late-stage NSPC abundances between KS1 and KS2 mouse models. CycleBase data support this hypothesis, suggesting that KMT2D and KDM6A exhibit a non-overlapping, complementary expression timing during the cell cycle (Supplementary Figure 4.2A), providing rationale for future studies in KS NSPC models.

Recent studies suggest control of NSPC proliferation by neuronal electrochemical signaling and excitation-inhibition balance. In the adult DG, RGL activation and IPC proliferation rates depend in part on GABA signaling, through its influence on S-phase duration (Andäng et al. 2008), and $GABA_A$ receptors are present in DG precursors from early stages (Li et al. 2012). Previous studies in the adult hippocampus demonstrated coupling of neuronal circuitry and neurogenesis, mediated by GABAergic synaptic inputs from parvalbumin (PV)-expressing interneurons on quiescent RGLs in the SGZ (Song et al. 2013), raising the possibility that GABA-coupled cell cycle alterations impact DG neurogenesis under pathological conditions. In fact, the earliest signaling activity in adult-born DG NSPCs occurs via GABA receptors (Ge et al. 2007), whose activity negatively regulates NSPC activation (Song et al. 2013), and indeed inhibition of $GABA_A$ signaling was found to increase proliferation of DG NSPCs in normal mice (Tozuka et al. 2005). In experiments using the GABA antagonist PTX in vivo, we observed opposite effects on NSPC activation and proliferation in *Kdm6a*$^{+/tm1d}$ mice relative to wild-types. Thus, aberrant GABA responses in the KS2 mouse hippocampus provide rationale for future interrogation of DG niche

signaling in NSPCs. Furthermore, because GABA mediates excitation-inhibition balance also in maturing and post-mitotic DG neurons, aberrant GABA response in KS models could alter hippocampal memory circuits on a large scale. Future studies should interrogate the KS1 (*Kmt2d*$^{+/\beta geo}$) mouse model under a similar drug paradigm, as well as electrochemical activity in these circuits.

In summary, this work provides evidence for shared neurodevelopmental defects in KS1 and KS2 that are caused by transcriptional suppression of glycolysis, hypoxia-responsive, and cell cycle gene pathways. Specifically, the depletion of early NSPCs, cell cycle defects, and transcriptomic phenotypes suggests that loss of either KMT2D or KDM6A results in dysregulation of similar gene targets in adult neurogenesis. Given established roles of glycolytic pathways in stem cell maintenance, i.e. preventing mitotic entry of qRGLs, our findings suggest that therapeutic upregulation of glycolysis metabolism in adult hippocampal precursors could rescue the suppressed stem cell maintenance programs and thereby replenish the pool of quiescent NSPCs critical to AHN. Most importantly for KS patients, replenishment of the quiescent NSPC pool may ameliorate KS-associated ID phenotypes by restoring a healthy supply of adult DG precursors that can be recruited for context-dependent learning, and differentiated at a proper rate that fosters normal adaptive and spatial memory despite the presence of underlying causative mutations.

Methods

Animals

All experimental mice were on a fully backcrossed C57BL/6J background and expected Mendelian ratios were observed when bred to wild-type. The *Kdm6a*$^{+/tm1a(EUCOMM)Wtsi}$ allele was generated by the International Knockout Mouse Consortium (IKMC) European Conditional Mouse Mutagenesis Program (EUCOMM) and distributed by the European Mutant Mouse Archive (EMMA). The

targeting construct contains a Frt site-flanked splice acceptor *β-geo* cassette preceding the loxP site-flanked third exon of *Kdm6a*. *Kdm6a*$^{+/tm1a}$ females were crossed with male flippase-expressing mice (B6.Cg-Tg(ACTFLPe)9205Dym/J) (Jackson Laboratories) to remove the *β-geo* cassette, producing the *Kdm6a*$^{+/tm1c}$ conditional allele. Homozygous *Kdm6a*$^{+/tm1c}$ females were crossed with male Cre-expressing mice (B6.C-Tg(CMV-cre)1Cgn/J) (Jackson Laboratories) to excise the loxP-flanked exon. The resulting *Kdm6a*$^{+/tm1d}$ allele was propagated In heterozygosity by crossing females with C57BL/6J males. All experimental animals were on a fully backcrossed C57BL/6J background devoid of Cre and Flp alleles. Animals were housed in a 14 hr light/10 hr dark cycle with free access to food and water. For drug treatments with PTX, mice received 0, 0.1, or 0.5 mg/kg/day PTX by IP injection, and were closely monitored for signs of epileptic activity or distress. All experiments were performed using mouse protocols approved by the Animal Care and Use Committee of Johns Hopkins University School of Medicine and are in accordance with guidelines used by the National Institutes of Health (NIH) for mouse care and handling. All experiments compare mutant mice against age- and sex-matched wild-type littermates.

Immunostaining and confocal imaging

Coronal brain sections (30 μm) through the entire dentate gyrus (every sixth slice) were maintained in serial order. Brains were paraformaldehyde-fixed by transcardial perfusion and post-fixed in 4% PFA overnight at 4°C before cryoprotection by sequential overnight incubations at 4°C with sucrose concentrations of 10%, 20% and 30% in phosphate buffer. Brains were sectioned by cryostat (Leica), directly mounted to charged slides, and stored at -80°C. Antigen retrieval (DakoCytomation, # S1699) was performed at 95°C for 20 minutes. After blocking, overnight incubation at 4°C in primary antibodies (Table S1) was followed by 2 hr room temperature incubation with AlexaFluor-conjugated secondary antibodies at 1:500 dilution. Blocking buffer of 0.1% Triton X-100 in TBS

contained 6% serum matched to the host species of secondary antibody. Tiled, z-stacked images were acquired using an inverted Zeiss LSM780 AxioObserver confocal microscope and Zen software (Zeiss) to encompass the entire GCL area of each section using 10X, 20X, or 40X objective. Images were quantified using Imaris (BitPlane). Cell counts for each GCL slice analyzed were corrected by the total GCL area multiplied by z-thickness of the image, and expressed as cells/mm^3. DCX+ neuroblast migration and size were measured in Fiji (NIH) by experimenters blinded to condition and genotype.

EdU+ nucleus isolation

Mice were injected with 150 mg/kg EdU at experiment-dependent time points prior to sampling. Mouse dentate gyrus (DG) was micro-dissected in ice-cold PBS immediately following sacrifice by halothane inhalation. Total nuclei were purified as described (Rizzardi et al., 2017) with addition of RNAse inhibitor to all buffers (Table S2). Briefly, bilateral DG from individual mice were dounce-homogenized in 1 ml lysis buffer and layered above a sucrose gradient for ultracentrifugation at 28,600 RPM for 2h at 4°C. Supernatant was aspirated and nuclei were resuspended in staining buffer of Click-iT EdU AlexaFluor-488 Flow Cytometry Kit (Invitrogen, #10425) with addition of RNAse inhibitor, and incubated 30 minutes at room temperature. Samples were passed through 40 μm filter, stained with 1 μg/ml DAPI, and kept on ice before sorting. Nuclear lysates processed identically from non-EdU-injected mice served as negative controls for cytometry. Nuclei were sorted using a Beckman Coulter MoFlo Cell Sorter with proper gate settings (Figure S5) into 96-well plates containing Smart-seq 2 lysis buffer (2 μL Smart-Seq2 lysis buffer + RNAase inhibitor, 1 μL oligo-dT primer, and 1 μL dNTPs), briefly spun by tabletop microcentrifuge and snap-frozen on dry ice. Single-nucleus lysates were stored at -80°C until cDNA conversion. Empty wells served as negative control.

Single-nucleus reverse transcription, cDNA library preparation, and sequencing

Individually-sorted nuclei were processed according to a modified Smart-seq2 protocol (Picelli et al., 2013). Briefly, 96-well plates of single nuclei lysates were thawed to 4°C, heated to 72°C for 5 minutes, and immediately placed on ice. Template-switching first-strand cDNA synthesis was performed using a 5'-biotinylated TSO oligo. cDNAs were amplified using 22 cycles of KAPA HiFi PCR and 5'-biotinylated ISPCR primer. Amplified cDNA was cleaned using 1:1 ratio of Ampure XP beads and approximately 250 pg was input to a one-quarter-sized Nextera XT tagmentation reaction. Tagmented fragments were amplified for 20 enrichment cycles and dual indexes were added to each well to uniquely label each library. Concentrations were assessed with Quant-iT PicoGreen dsDNA Reagent (Invitrogen) and samples were diluted to ~2nM and pooled. Pooled libraries were sequenced on the Illumina HiSeq 2500 platform to a target mean depth of ~8 x 10^5 bp paired-end fragments per cycle at the Johns Hopkins Genetics Research Core Facility.

Bulk RNA-seq analysis

For all libraries, paired-end reads were aligned to the mouse reference genome (mm10) using HISAT2 (Kim et al., 2015) with default parameters except: -p 8. Aligned reads from individual samples were quantified against a reference genome (GENCODE vM8) (Mudge et al., 2015). Quantification was performed using cuffquant with default parameters and the following additional arguments: [--no-update-check –p 8]. Normalized expression estimates across all samples were obtained using cuffnorm with default parameters (Trapnell et al., 2012).

Single-nucleus data analysis

Gene-level and isoform-level FPKM (Fragments Per Kilobase of transcript per Million) values produced by cuffquant and the normalized FPKM matrix from cuffnorm were used as input to Monocle (v2.2.0) (Trapnell et al., 2014) in R/Bioconductor (Huber et al., 2015). QC filters based on distributions of total mass, total mRNA number, and total expressed genes per cell were applied before performing principal component analysis (PCA) to identify outliers identified as oligodendrocyte and interneuron precursors, Genes were annotated using GENCODE vM8. A CellDataSet was then created using Monocle (v2.2.0) containing the gene FPKM table, gene annotations, and all available metadata for the sorted nuclei. Negative control and empty wells were discarded. Relative FPKM values for each nucleus were converted to estimates of absolute mRNA counts per cell (RPC) using the Monocle 2 Census Algorithm using the Monocle function "relative2tabs" (Qiu et al., 2017).

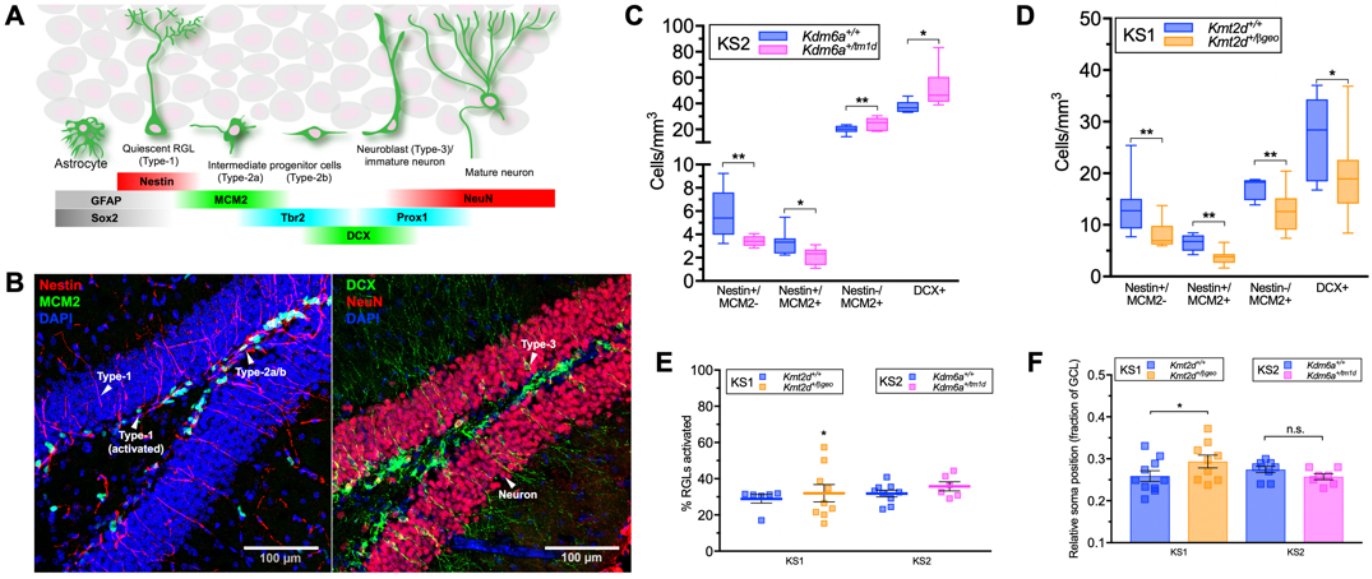

Figure 4.1. Neurogenesis phenotypes in a KS2 mouse model
(**A**) Schematic diagram reflecting the current view of stage-specific markers in adult hippocampal neurogenesis. (**B**) Sample confocal images using immunostaining against cell type-specific markers. Images represent cropped areas from maximum intensity projections of tiled z-stacked images, acquired and stitched using Zen software (~12 z-stacks acquired per mouse using every 6th brain slice maintained in serial order). (**C**) Quantification of neurogenesis stages in *Kdm6a*$^{+/tm1d}$ mice (n=9) and wild-type littermates (n=7). Cell counts for each image corrected by GCL volume, expressed as cells/mm^3. Boxes represent median and interquartile range, and whiskers represent minimum and maximum (**p<0.01; *p<0.05; Student's t-test). (**D**) Quantification of neurogenesis stages in *Kmt2d*$^{+/βgeo}$ mice (n=10) and wild-type littermates (n=9). Cell counts for each image corrected by GCL volume, expressed as cells/mm^3. Boxes represent median and interquartile range, and whiskers represent minimum and maximum (**p<0.01; *p<0.05; Student's t-test). (**E**) Activated RGLs, expressed as percent among total RGLs, analyzed by one-way ANOVA (Bartlett's statistic=9.625, *p=0.022). (**F**) Radial position of DCX+ neuroblasts. The distance of each cell body from inner boundary of GCL, corrected by GCL thickness, is expressed as fraction of GCL. Number of neuroblasts analyzed: Kmt2d$^{+/βgeo}$ (n=3,353) and wildtype littermates (n=3,007); *Kdm6a*$^{+/tm1d}$ (n=3,995) and wild-type littermates (n=3,249). Bars represent mean±SEM (*p<0.05; Student's t-test).

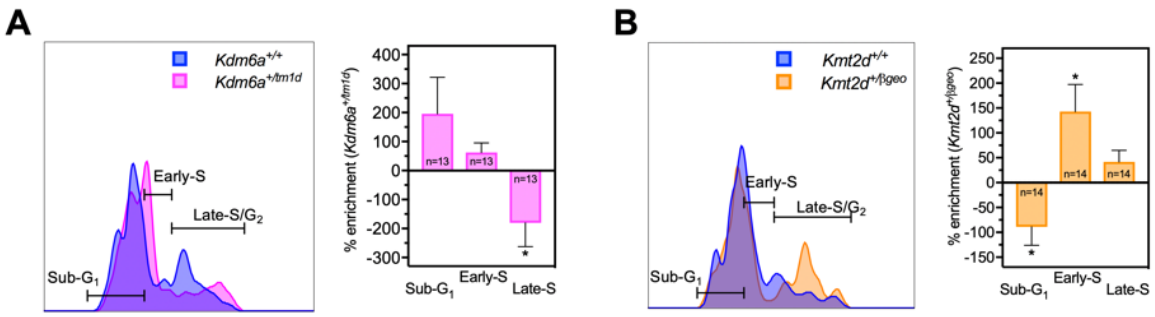

Figure 4.2. Cell cycle phenotypes in a KS2 mouse model
(**A-B**) Sample FACS gating and quantification, analyzed by DAPI fluorescence, of fold enrichment of sub-G_1, early-S, and late-S/G_2 cells in *Kdm6a*$^{+/tm1d}$ mice (**A**) and *Kmt2d*$^{+/\beta geo}$ mice (**B**), compared to wild-type littermates. Bars represent mean±SEM (*$p<0.05$; Student's t-test).

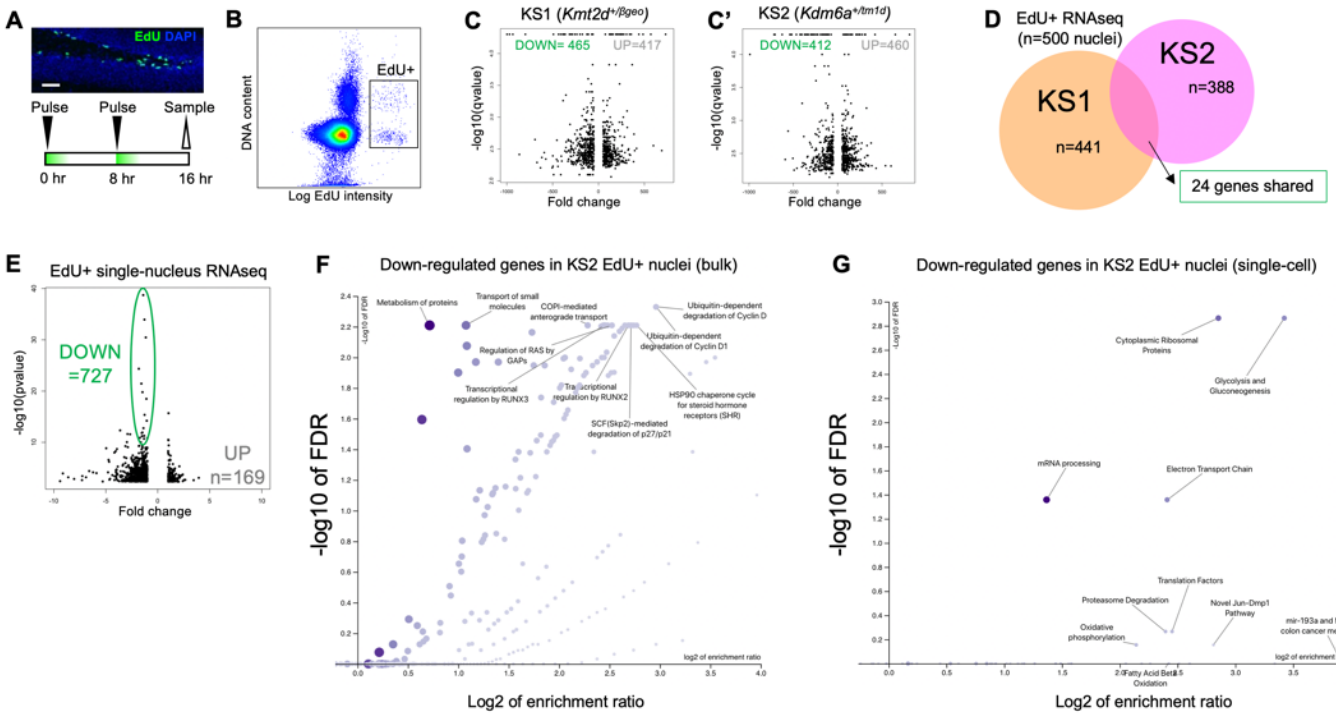

Figure 4.3. Gene expression profiling in KS2 NSPCs

(**A**) Sample confocal image EdU+ DG NPCs and schematic depiction of the EdU pulsing paradigm for sampling of proliferating DG NPCs. (**B**) Sample FACS plot of EdU-pulsed nuclei from micro-dissected DG. Scatter signals guided selection of viable singlets for analysis, and nuclei were gated based on EdU-AlexaFluor-488 intensity. (**C**) Volcano plots representing differentially expressed genes (DEGs) in EdU+ DG precursors (n=500 per group) of *Kmt2d*$^{+/\beta geo}$ mice versus wild-type littermates (**C**) and *Kdm6a*$^{+/tm1d}$ mice versus wild-type littermates (**C'**). (**D**) Intersection of downregulated genes in EdU+ nuclei of *Kmt2d*$^{+/\beta geo}$ (KS1) and *Kdm6a*$^{+/tm1d}$ (KS2) mice. (**E**) Volcano plot representing DEGs genes in EdU+ nuclei in *Kdm6a*$^{+/tm1d}$ mice versus wild-type littermates, as detected by snRNA-seq. (**F-G**) Over-representation analysis (ORA) highlighting gene networks enriched among downregulated genes in KS2 EdU+ nuclei, detected by bulk RNA-seq (**F**) and scRNA-seq (**G**).

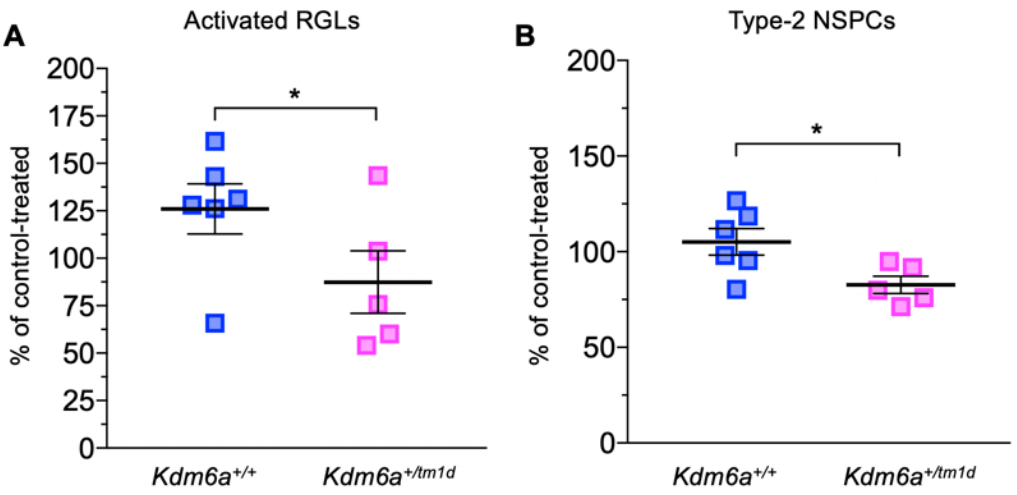

Figure 4.4. Differential response to GABA antagonism in KS2 NSPCs
(**A-B**) Quantification of activated type-1 RGLs (**A**) and type-2 NPCs (**B**) in *Kdm6a*$^{+/+}$ and *Kdm6a*$^{+/tm1d}$ mice treated with GABA antagonist (picrotoxin) by daily IP injection for 2 weeks. Values represent PTX effect compared to vehicle-treated, expressed as % drug-treated/vehicle-treated. (*$p<0.05$; Student's t-test).

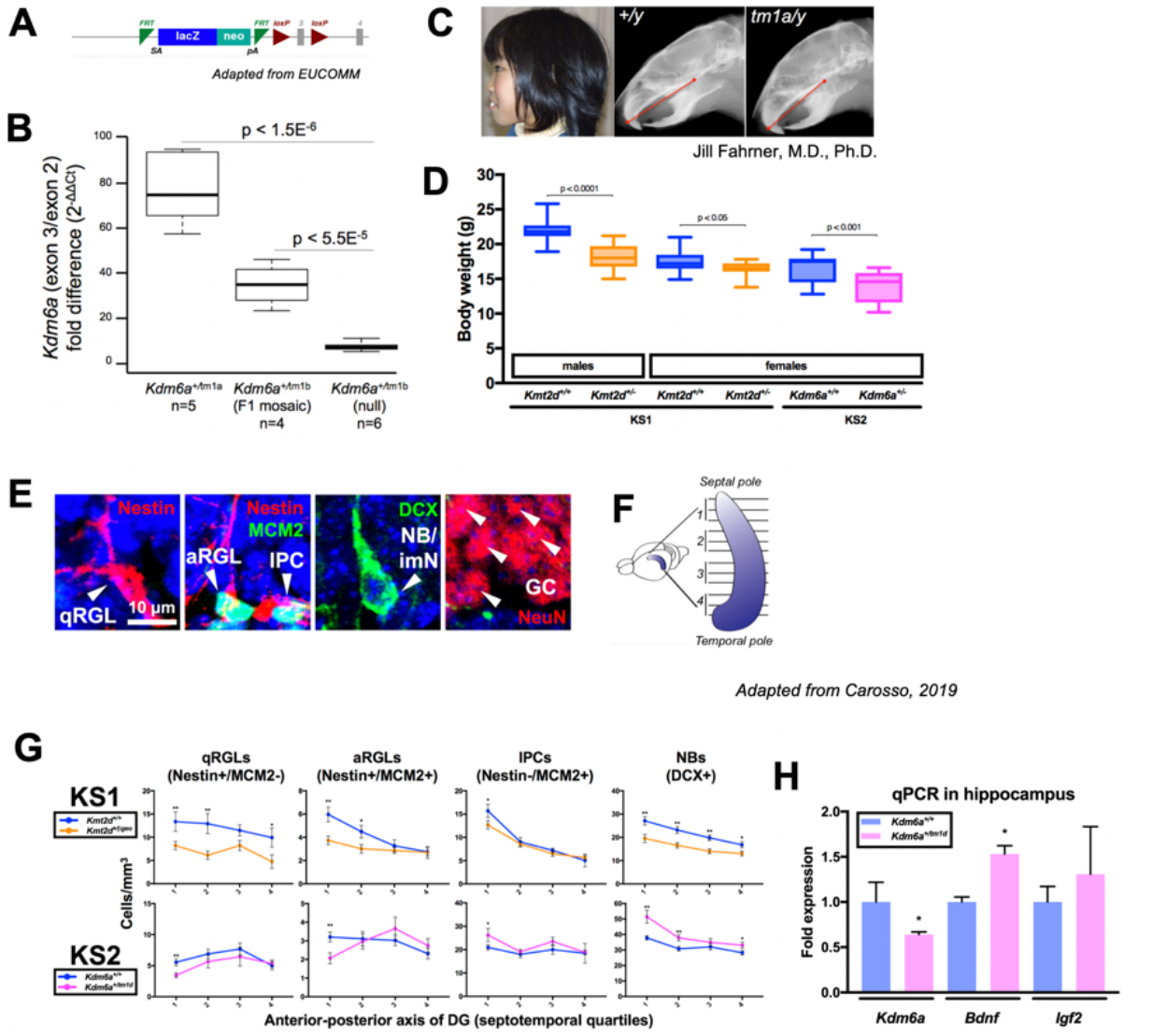

Supplementary Figure 4.1. Supporting data and validations for *Kdm6a*-deficient mice. (**A**) Schematic diagram of EUCOMM *Kdm6a* conditional knock-out allele. (**B**) qRT-PCR of *Kdm6a* knock-out in *Kdm6a*$^{+/tm1b}$ F1 mosaic and null *Kdm6a*$^{+/tm1b}$ mice. (**C**) X-rays depicting craniofacial characteristics in *Kdm6d*$^{tm1a/y}$ mice reminiscent of KS patients. (**D**) Body weights of 2-month old KS1 and KS2 mice, demonstrating growth restriction. Boxes represent median and interquartile range, and whiskers represent minimum and maximum. (**E**) Sample confocal images using immunostaining against cell type-specific markers. Images represent cropped areas from maximum intensity projections of tiled z-stacked images, acquired and stitched using Zen software (~12 z-stacks acquired per mouse using every 6th brain slice maintained in serial order). (**F**) Schematic of tissue slices stratified anatomically along the septo-temporal axis. (**G**) Quantification, stratified anatomically, of neurogenesis stages in *Kmt2d*$^{+/\beta geo}$ mice (n=10) and wild-type littermates (n=9), and *Kdm6a*$^{+/tm1d}$ mice (n=9) and wild-type littermates (n=7). Cell counts for each image corrected by GCL volume, expressed as cells/mm^3. (**p<0.01; *p<0.05; Student's t-test). (**H**) qRT-PCR of *Kdm6a* knock-out and pro-neural gene expression in hippocampus of fully backcrossed *Kdm6a*$^{+/tm1d}$ mice.

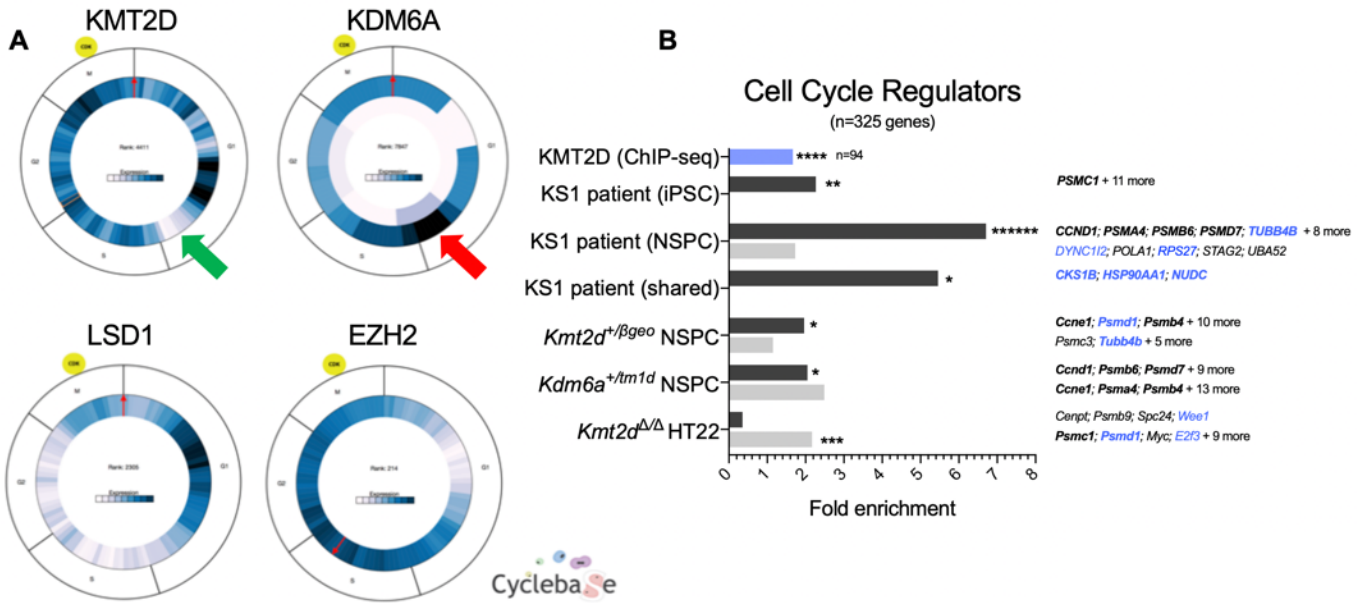

Supplementary Figure 4.2. Complementary expression patterns of KS genes.
(**A**) CycleBase data indicating higher expression of KDM6A during a gap of KMT2D expression in late G_1 phase. Complementary patterns also seen for LSD1 and EZH2. (**B**) Enrichment of cell cycle regulatory genes among KS datasets. Bold indicates genes occurring in >1 model dataset, blue indicates genes that also bind KMT2D in wild-type HT22 cells (Carosso et al., 2019). Fisher's Exact Test (*p<0.05, **p<0.01, ***p<0.001).

CHAPTER 5: FUTURE AVENUES FOR KS INVESTIGATION

FUTURE AVENUES FOR KS INVESTIGATION

Aberrant neurogenesis in the *Kmt2d*$^{+/\beta geo}$ olfactory bulb

Beyond the dentate gyrus (DG), a second major zone of neurogenesis in mammals exists in the subventricular zone (SVZ), which generates neuroblasts (NBs) migrating along the rostral migratory stream (RMS) to reside in the olfactory bulb (OB). These cells are important to adaptive olfactory learning throughout adult life, especially in rodents. Given in vivo defects of adult hippocampal neurogenesis (AHN) observed in the *Kmt2d*$^{+/\beta geo}$ mouse model, we examined doublecortin-positive (DCX$^+$) adult-born neuroblasts (NBs), as well as mature neuronal marker (NeuN$^+$) in the OB of *Kmt2d*$^{+/\beta geo}$ mice and age- and sex-matched littermate controls, using immunofluorescence and confocal microscopy (Figure 5.1, A-C). We found that compared to wild-types, *Kmt2d*$^{+/\beta geo}$ mice demonstrated significantly increased numbers of DCX$^+$ NBs, but modest reductions in total NeuN$^+$ mature neurons in the OB (Figure 5.1, D). Furthermore, the average cell body size was significantly larger in DCX$^+$ NBs of *Kmt2d*$^{+/\beta geo}$ mice (Figure 5.1, E). Quantification by fluorescence of the open chromatin mark H3K4me3 revealed modest differences in *Kmt2d*$^{+/\beta geo}$ mice compared to wild-type littermates, though not reaching statistical significance (Figure 5.1, F).

Altered SVZ-OB neurogenesis in *Kmt2d*$^{+/\beta geo}$ mice suggests that KS-associated neuronal differentiation phenotypes may contribute to neurological abnormalities outside the hippocampus as well. Future studies should determine whether neurodevelopmental phenotypes occur strictly in adult neurogenesis, or whether such defects are observable during embryonic neurodevelopment. Nonetheless, given that KS is most commonly diagnosed at post-natal times, the pursuit of adult neurogenesis research offers the most promise for therapies in KS patients.

Synaptic architecture differences in the *Kmt2d*$^{+/\beta geo}$ hippocampus

Several interesting findings emerged from analyses of classical neurologic phenotypes in the hippocampus of *Kmt2d*$^{+/\beta geo}$ mice. Quantification of electron micrographs revealed no differences in the total number of synapses per field of view; however, the proportion of synapses exhibiting "perforated" morphology was significantly higher in *Kmt2d*$^{+/\beta geo}$ mice (Figure 5.2, A). Perforated synapses are characterized by discontinuous post-synaptic densities and are thought to represent ongoing synaptic turnover, suggesting possible implications for neurotransmitter signaling, and thereby adaptive learning, at the cellular level in KS models. Interestingly, *Kmt2d*$^{+/\beta geo}$ mice also exhibited significantly increased numbers of myelinated axons per field of view (Figure 5.2, A), which could reflect alterations of axon density, axon navigation, or oligodendrocyte-mediated myelinating functions in *Kmt2d*$^{+/\beta geo}$ mice. Within cell bodies imaged in the same electron micrographs, we quantified nucleolus-associated heterochromatin (NAH) complexes, observing significantly higher densities in *Kmt2d*$^{+/\beta geo}$ mice (Figure 5.2, A).

More detailed studies are needed to determine the exact contents of these complexes; because RNA-seq revealed extensive dysregulation of ribosomal genes across several KS1 models in brain and other tissues, one might interrogate ribosomal RNA, DNA, or biogenesis phenotypes.

Neuroinflammatory phenotypes in *Kmt2d*$^{+/\beta geo}$ mice

Neuroinflammation, a major cause of cognitive decline, is characterized by elevated infiltration and activity of microglia and astrocytes in the brain. We therefore quantified the microglial marker IBA1 to estimate relative microglial presence. We also quantified the glial fibrillary acidic protein (GFAP) to estimate the numbers of astrocytes (Figure 5.2, B). Quantification by confocal microscopy revealed significantly increased fluorescence of IBA1 in *Kmt2d*$^{+/\beta geo}$ mice compared to wild-type littermates, as well as a modest, but insignificant, increase in GFAP fluorescence.

Although we found extensive evidence for cell-autonomous mechanisms of neurodevelopmental disruptions in multiple KS1 models (Carosso et al. 2019), the increased microglial and astrocytic activity in the DG of *Kmt2d*$^{+/\beta geo}$ mice suggest that cell-extrinsic, immune-mediated inflammation could contribute to the hippocampal KS1 phenotypes. This hypothesis is worth pursuing, given the immune system defects in KS1. Experiments might include investigating the degradation of the blood-brain barrier in the KS1 brain, in vivo pulse-labeling followed by quantification of microglial engulfment of proliferating NSPCs, or studies of cell type-specific *Kmt2d* loss-of-function in immune, neuronal, and glial cells.

DNA damage phenotypes in KS1 models

Several experiments in KS1 mouse and human models demonstrate that aberrant DNA damage responses correlate with proliferation defects. The pronounced accumulation of Late-S/G_2 cells among Type-2 NPCs of *Kmt2d*$^{+/\beta geo}$ mouse, as well as in iPSCs of a *KMT2D*$^{+/-}$ patient, raises the possibility that stalling at DNA replication checkpoints mediate KS1-related proliferation defects. DNA damage during replication triggers a response characterized by phosphorylation of the histone variant H2AX, yielding γH2AX. This response occurs both upon transcription/elongation stress and DNA damage at stalled replication forks, accumulating progressively during S and G_2 phases and causing mitotic arrest through the p53/p21 pathway (Fernandez-Capetillo et al. 2002). Intriguingly, *Kmt2d* loss was recently shown to elevate γH2AX specifically at sites exhibiting both transcriptional stress and genome instability in oncogenic models (Kantidakis et al. 2016), implicating clashes between RNA polymerase II (RNAPII) transcription apparatus and the replication fork (Bermejo et al. 2012). Specifically, dysregulation of γH2AX was described in mouse embryonic fibroblasts and human colorectal carcinoma cells bearing homozygous *Kmt2d* loss-of-function, with γH2AX

enriched at genomic loci showing the highest levels of transcription stress and genome instability (Kantidakis et al. 2016). Interestingly, KMT2D interacts with RNAPII and the transcription elongation complex RECQL5 (Kantidakis et al. 2016). These loci significantly overlap with known early replicating fragile sites (ERFSs), i.e. regions with recurrent double-strand breaks in oncogenic contexts (Barlow et al. 2013). To interrogate the γH2AX S/G_2 checkpoint pathway in KS1 patient cells, we stained EdU-pulsed KS1 patient and control iPSCs using γH2AX antibody, and we analyzed them by flow cytometry (Figure 5.3A). Because the cells segregated into peaks of high- and low-γH2AX intensity within the EdU^+ population, we used a gating strategy to quantify high and low cells. A characteristic pattern emerged among all lines tested: the proportion of high-γH2AX cells increased progressively from early-S/G_1, through mid-S, to late-S/G_2 (Figure 5.3B), reflecting established γH2AX dynamics (Fragkos et al. 2009). However, KS1 iPSCs showed a two- to three-fold increase in high-γH2AX cells, with decreasing magnitude of difference along S-phase progression: the fold increases of high-γH2AX in KS1 lines among cells in early-S/G_1, mid-S, and late-S/G_2 were ~5.2, ~3.1, and ~1.6, respectively (Figure 5.3B), suggesting that KS-associated γH2AX elevation is most pronounced during early replication. Identical experiments in NSPCs showed opposite γH2AX effects, with 33.3% fewer KS1 NSPCs of high intensity (Figure 5.3C). We then profiled γH2AX intensity in EdU+ Type 2 NSPCs from mice *ex vivo,* and remarkably those of *Kmt2d*$^{+/\beta geo}$ mice mirrored the effects in human NSPCs, with 47.7% fewer high-intensity γH2AX cells (Figure 5.3D).

Our findings of γH2AX phenotypes in KS1 models suggest that DNA damage during replication contributes to KS1-associated proliferation defects. Further studies of different KS1 model systems are needed to interrogate differences in γH2AX phenotypes. Comparing KS1 iPSC findings to that found by Kantidakis et al. supports the notion that DNA damage is increased in KS1. Whereas the γH2AX response indicates DNA damage, the cause of this damage remains to be explored. Previously established mechanisms reveal interaction between replication machinery and transcriptional machinery, raising the possibility that gene expression differences in KS1 could impact DNA synthesis, and vice versa. Interesting experiments would include RNA Pol II occupancy profiling, or sequencing of EdU-incorporated DNA. In the latter experiment, DNA is collected shortly following EdU pulse, which labels replicating DNA in S-phase, purified by fluorescence detection, then sequenced to determine enrichment of replicating regions. Genotype-dependent differences in enriched sequences might reveal replication phenotypes in KS models.

Differential pharmacologic responses in KS1 models

We previously demonstrated *in vivo* rescue of impairments in adult neurogenesis and spatial memory in a KS1 mouse model using HDACi therapy to promote open chromatin (Bjornsson et al. 2014). To test whether HDACi rescues γH2AX levels in KS1 models, we treated iPSCs NSPCs with the HDAC inhibitor AR-42 for 72 hours. Interestingly, AR42 reduced γH2AX levels in KS1 iPSCs in a dose-dependent manner, while having little effect on control lines (Figure 5.4A). In contrast, an opposite effect emerged in NSPCs, with γH2AX levels rising dose-dependently in control lines but having little effect in KS1 lines (Figure 5.4A'). We found that AR42 had negligible effects on proliferation in iPSCs (Figure 5.4B); the control NSPCs cells were markedly less proliferative at high

dose, but KS1 cells did not appreciably change (Figure 5.4B'). AR42 had no effect on levels of the H3K4me3 open chromatin mark in iPSCs, while in NSPCs, H3K4me3 levels were elevated, dose-dependently as expected in control lines (Figure 5.4C) but not in KS1 lines (Figure 5.4C').

Proteostasis defects and NMD in KS1 models

Proteostatic mechanisms are critical to neuronal function, and their breakdown is known to be a contributing factor in multiple neurological pathologies including Alzheimer's disease (AD), via accumulation of toxic protein aggregates. RNA-seq analysis of proliferating DG nuclei in *Kdm6a*$^{+/tm1d}$ mice and *Kmt2d*$^{+/\beta geo}$ revealed differential expression of proteasome-related genes in both models. In fact, the gene showing greatest down-regulation in EdU^{+} nuclei of both *Kdm6a*$^{+/tm1d}$ mice and *Kmt2d*$^{+/\beta geo}$ was proteasome maturation protein (*Pomp*). Furthermore, a number of enzymes pertinent to KS pathology are known to regulate autophagy, including KDM6A and LSD1. *LSD1* loss-of-function was found to disrupt oxidative phosphorylation, hinder neuronal differentiation, and fatten mice (opposite effects to KMT2D loss-of-function). However, what is common in models of both LSD1 and KMT2D deficiency is the aberrant cytoplasmic sequestration of LSD1 and KMT2D, as well as their association with protein aggregates(Figure 5.5A) (Ambrosio et al. 2019; Engstrom et al. 2019). The known autophagy-regulating functions of LSD1 and KDM6A raise the tantalizing possibility of a novel role for KMT2D in these same processes.

We therefore used confocal microscopy and flow cytometry to evaluate accumulation of protein aggregates in a KMT2D-deficient hippocampal neuronal model (HT22), as well as patient-derived fibroblasts from KS1 patients and healthy controls, by measuring fluorescence of Proteostat, a marker binding to characteristic pleated-sheet conformations of toxic protein aggregates. We observed increased Proteostat fluorescence in both models, i.e. mouse-derived KMT2D-deficient HT22 cells, as well as KS1 patient-derived fibroblasts, relative to respective healthy controls (Figure

5.5, A, D-E). Careful regulation of protein synthesis and degradation is increasingly recognized as a factor in the onset of neuronal differentiation (Baser et al. 2019), therefore further investigation of proteostatic mechanisms could shed light on additional factors contributing to precocious neuronal maturation in KS models. Nonsense-mediated decay (NMD) pathways were enriched in KS1 DEGs in several model systems. Upon evaluation of transcripts known to undergo regulation by NMD (Hurt et al. 2013), we indeed observed significant enrichment among our DEGs of NMD-regulated transcripts, as well as genes directly targeted by UPF1 for NMD degradation (Figure 5.5B-C).

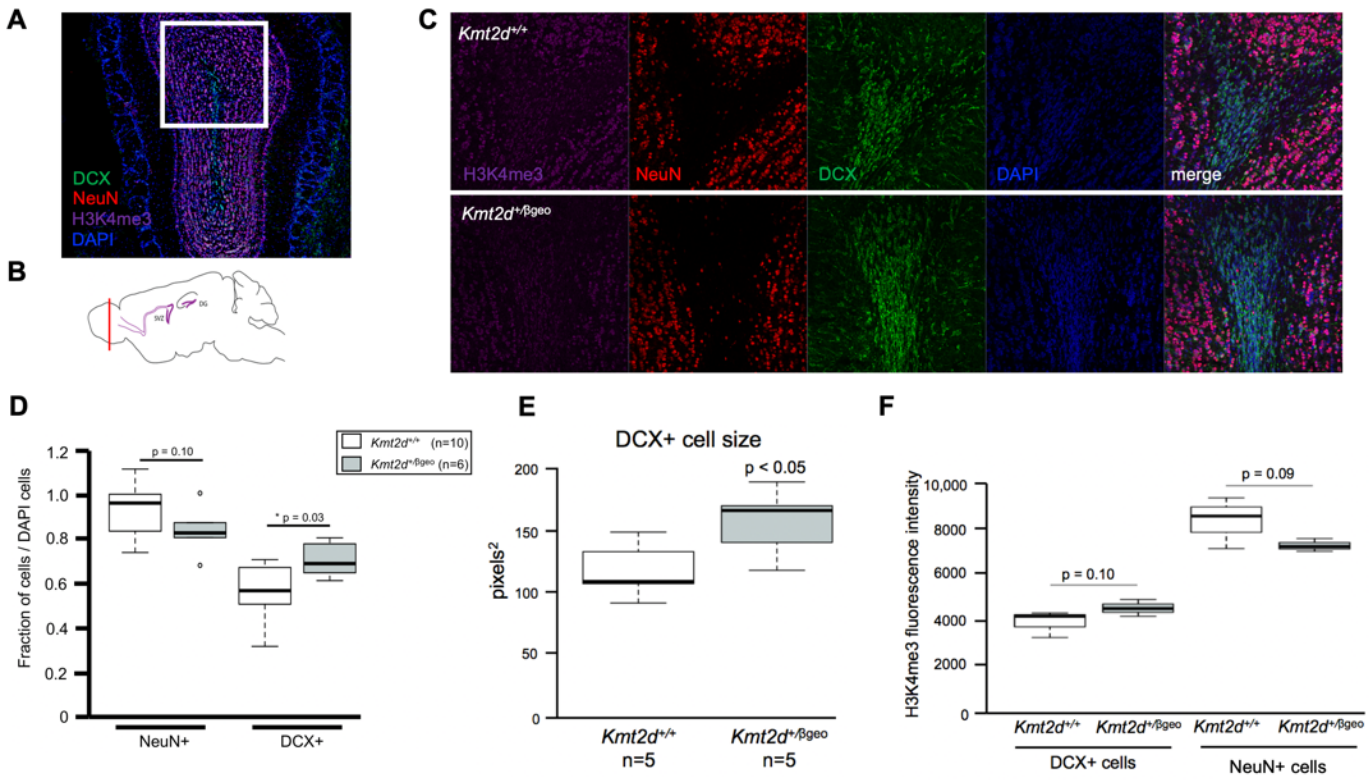

Figure 5.1. Aberrant neurogenesis in the *Kmt2d*$^{+/\beta geo}$ olfactory bulb
(**A-B**) Confocal image and schematic depicting the olfactory bulb (OB) region sampled for neurogenesis studies. (**C**) Representative confocal images of OB in KS1 and wild-type mice for neurogenesis profiling. (**D-F**) Quantification of (**D**) numbers of mature neurons (NeuN) and neuroblasts (DCX) in the OB, neuroblast size (**E**), and H3K4me3 fluorescence intensity in neurons and neuroblasts (**F**). Boxes represent median and interquartile range, and whiskers represent minimum and maximum (**p<0.01; *p<0.05; Student's t-test).

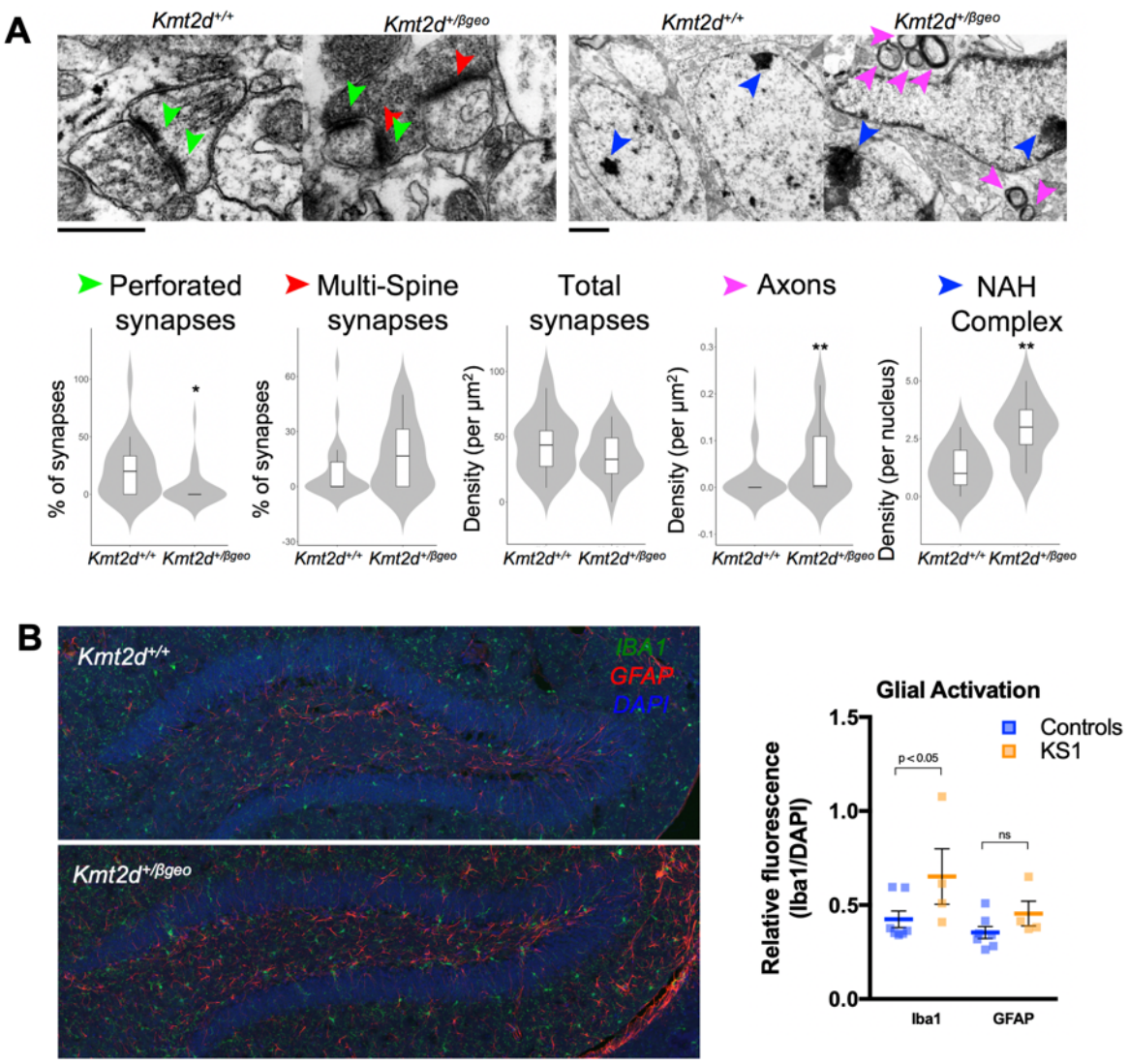

Figure 5.2. Synaptic architecture differences in the *Kmt2d*$^{+/\beta geo}$ hippocampus
(**A**) Electron micrographs of KS1 and wild-type mouse hippocampus, annotated with arrows indicating features quantified below in violin plots: perforated synapses, multi-spine synapses, total synapses, axons, and NAH complexes. (**B**) Sample confocal images used for analysis of microglia (Iba1) and astrocytes (GFAP) in mouse hippocampus, with quantification of fluorescence intensity.

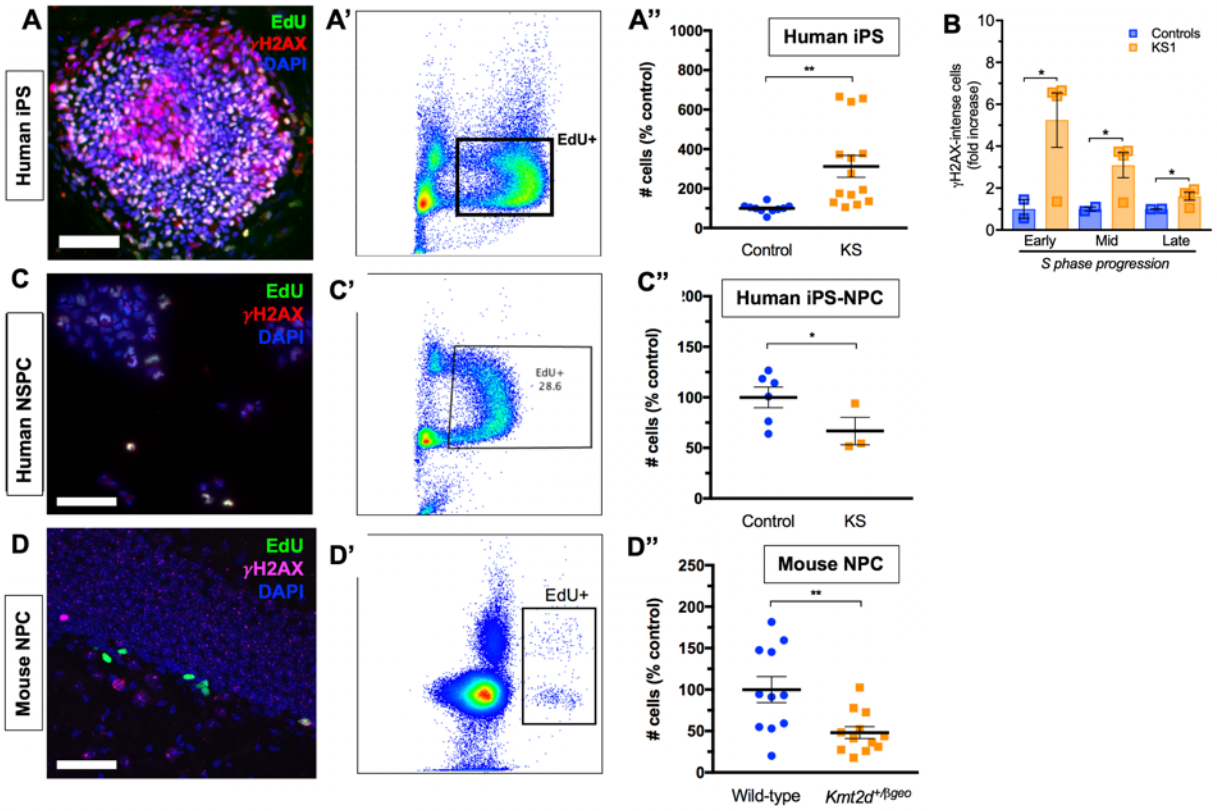

Figure 5.3. DNA damage phenotypes in KS1 models

(**A**) Sample immunostaining of γH2AX and EdU in iPSCs, subjected to FACS analysis (**A'**) for quantification of highly γH2AX-intense cells (**A''**). Bars represent mean±SEM (*p<0.05; Student's t-test). (**B**) Analysis of γH2AX-intense IPSCs, stratified by S-phase progression by gating based on DNA content. (**C**) Sample immunostaining of γH2AX and EdU in iPS-NPCs, subjected to FACS analysis (**C'**) for quantification of highly γH2AX-intense cells (**C''**). Bars represent mean±SEM (*p<0.05; Student's t-test). (**D**) Sample immunostaining of γH2AX and EdU in mouse DG, subjected to FACS analysis (**D'**) for quantification of highly γH2AX-intense cells (**D''**). Bars represent mean±SEM (**p<0.01; Student's t-test).

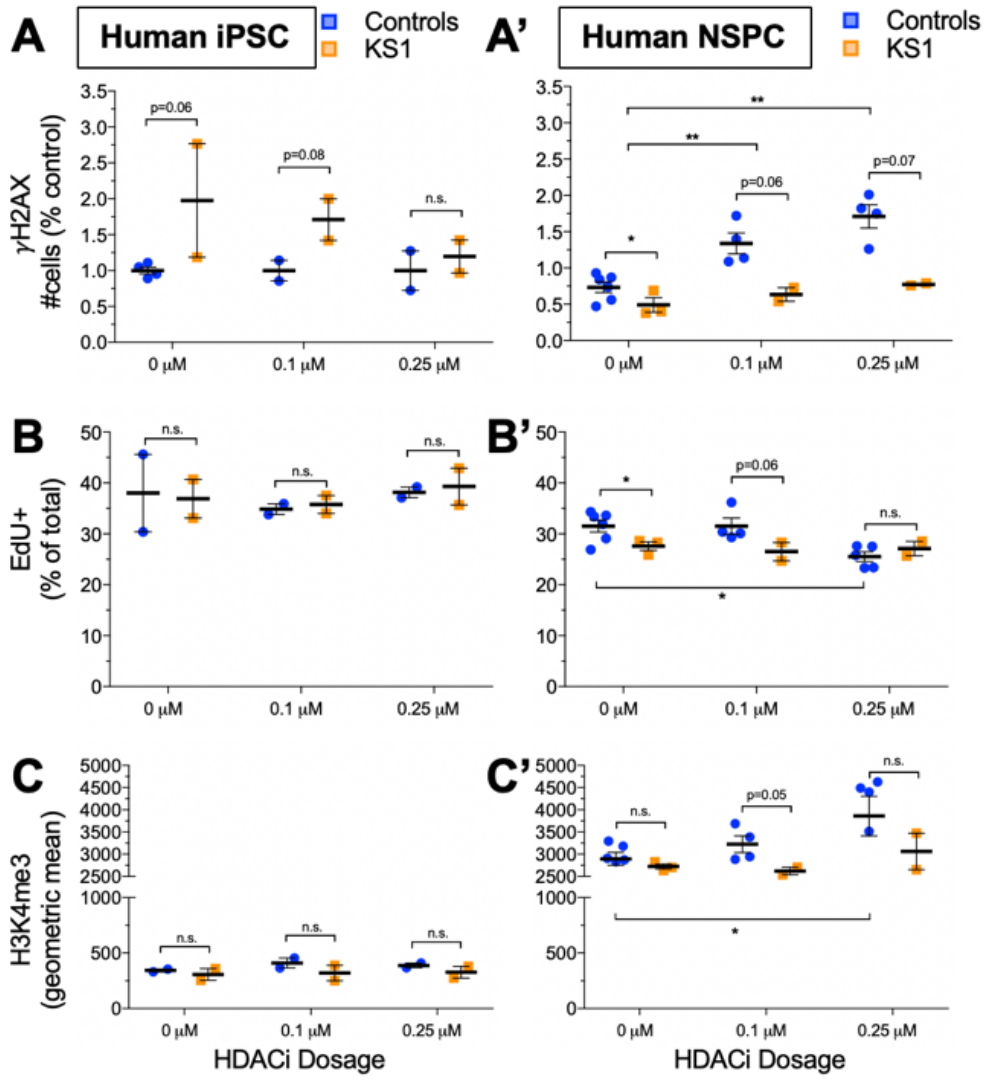

Figure 5.4. Differential pharmacologic responses in KS1 models

(**A**) Quantification of highly γH2AX-intense cells in iPSCs and iPS-NPCs after HDACi (AR42) treatment for 72 hours. (**B**) Quantification of EdU+ cells in iPSCs and iPS-NPCs after HDACi (AR42) treatment for 72 hours. (**C**) Quantification of H3K4me3 intensity in iPSCs and iPS-NPCs after HDACi (AR42) treatment for 72 hours.

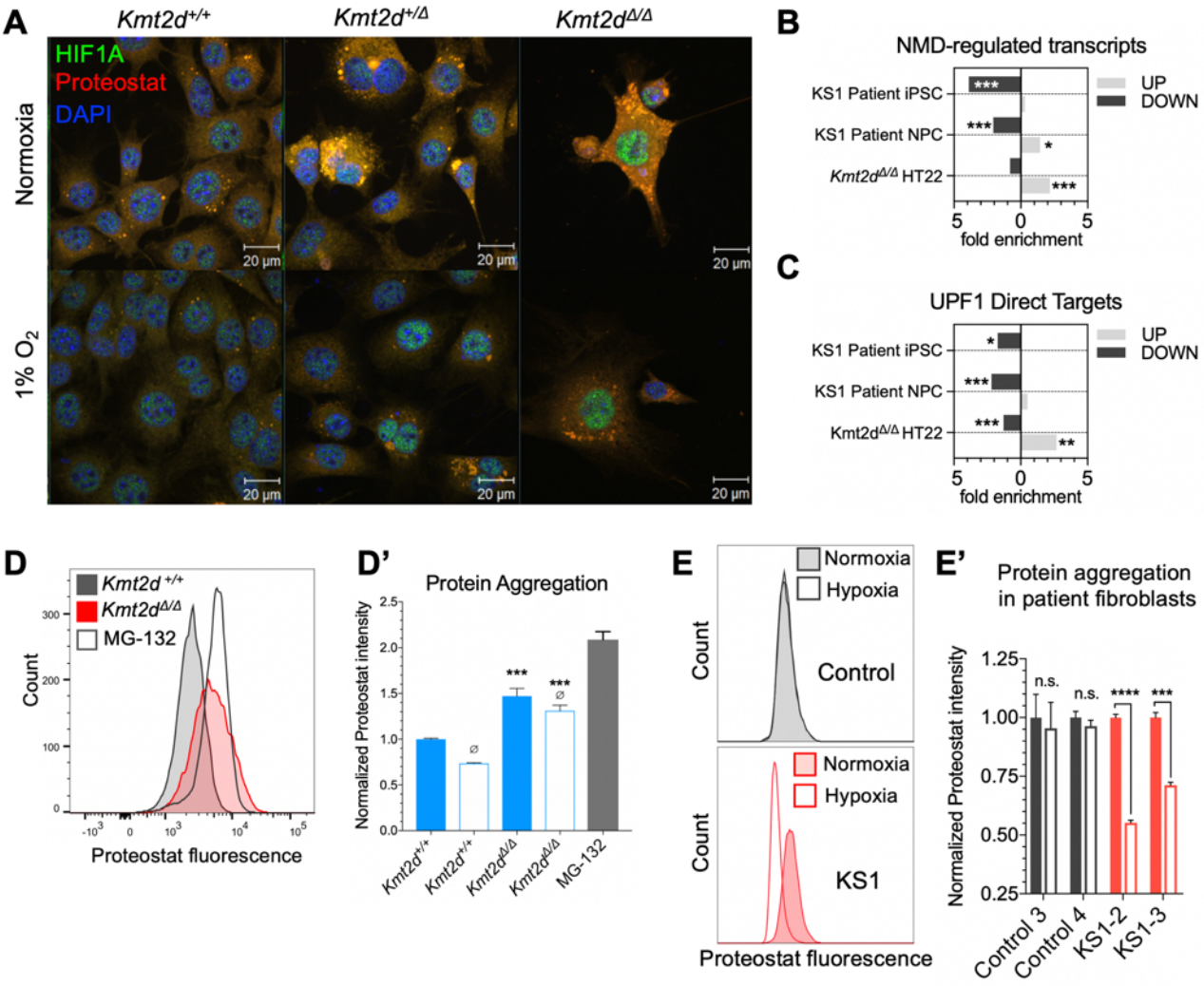

Figure 5.5. Proteostasis and NMD defects in KS1 models

A) Representative confocal images of *Kmt2d*$^{+/\Delta}$, *Kmt2d*$^{\Delta/\Delta}$, and wild-type HT22 cells in normoxic and hypoxic (72 hours with 1% O_2) conditions. Immunofluorescence against HIF1A for nuclear localization studies and Proteostat for analysis of misfolded protein aggregates. (**B-C**) Significant enrichment of NMD-regulated transcripts (Hurt et al. 2013) (**B**) and direct UPF1 targets (**C**) among observed DEGs in patient-derived cells and HT22 cells. Fisher's Exact Test (*p<0.05, **p<0.01, ***p<0.001). (**D-E**) Flow cytometric analysis of Proteostat fluorescence under normoxic or hypoxic conditions, with quantification, in HT22 cells (2 clones per genotype, each in technical triplicate) (**D**) and patient fibroblasts (each in technical triplicate) (**E**). Bars indicate mean ± SEM. Asterisks indicate significance from wild-type mean for each condition, student's t-test (*p<0.05, **p<0.01, ***p<0.001). Empty set symbol indicates significance from normoxic condition for each genotype, student's t-test (ø<0.05, øø<0.01).

CHAPTER 6: CONCLUSIONS

CONCLUSIONS

The studies described here help to establish several principles for the study of KS. Principle 1: KS is a treatable cause of intellectual disability (Chapter 2). Phenotypic rescue by HDAC inhibition, through administration of a ketogenic diet, validates prior findings using small molecule therapy and supports the idea that KS has a treatment window in postnatal life. Principle 2: KS leads to metabolic disruption (Chapter 2, Chapter 3, and Chapter 5). While the first hints of metabolic phenotypes emerged during ketogenic diet studies, with observations of NADH imbalance in KS mice (Chapter 2), we then learned through extensive profiling of several KS model systems (Chapter 3) that the pathways most strongly suppressed were those regulating key metabolic responses including hypoxia response and glycolysis. Principle 3: Neuronal differentiation rates are significantly accelerated in KS1 models, and appear to be increased as well in our KS2 mouse model. Along with findings of precocious maturation in chondrocytes and other cell types, these results reveal common developmental defects among KS models.

In summary, we present novel insights into the cellular and molecular basis of neurogenesis defects in KS, identifying metabolic dysregulation as a common mechanism of etiology in multiple model systems for KS1 and KS2. These findings suggest that epigenetic modulation maybe a plausible strategy for postnatal rescue of ID phenotypes in KS.

Bibliography

Alarcón, J.M., Malleret, G., Touzani, K., Vronskaya, S., Ishii, S., Kandel, E.R. and Barco, A. 2004. Chromatin acetylation, memory, and LTP are impaired in CBP+/- mice: a model for the cognitive deficit in Rubinstein-Taybi syndrome and its amelioration. *Neuron* 42(6), pp. 947–959.
Ambrosio, S., Ballabio, A. and Majello, B. 2019. Histone methyl-transferases and demethylases in the autophagy regulatory network: the emerging role of KDM1A/LSD1 demethylase. *Autophagy* 15(2), pp. 187–196.
Amemiya, H.M., Kundaje, A. and Boyle, A.P. 2019. The ENCODE blacklist: identification of problematic regions of the genome. *Scientific Reports* 9(1), p. 9354.
Andäng, M., Hjerling-Leffler, J., Moliner, A., Lundgren, T.K., Castelo-Branco, G., Nanou, E., Pozas, E., Bryja, V., Halliez, S., Nishimaru, H., Wilbertz, J., Arenas, E., Koltzenburg, M., Charnay, P., El Manira, A., Ibañez, C.F. and Ernfors, P. 2008. Histone H2AX-dependent GABA(A) receptor regulation of stem cell proliferation. *Nature* 451(7177), pp. 460–464.
Ang, S.-Y., Uebersohn, A., Spencer, C.I., Huang, Y., Lee, J.-E., Ge, K. and Bruneau, B.G. 2016. KMT2D regulates specific programs in heart development via histone H3 lysine 4 di-methylation. *Development* 143(5), pp. 810–821.
Barlow, J.H., Faryabi, R.B., Callén, E., Wong, N., Malhowski, A., Chen, H.T., Gutierrez-Cruz, G., Sun, H.-W., McKinnon, P., Wright, G., Casellas, R., Robbiani, D.F., Staudt, L., Fernandez-Capetillo, O. and Nussenzweig, A. 2013. Identification of early replicating fragile sites that contribute to genome instability. *Cell* 152(3), pp. 620–632.
Baser, A., Skabkin, M., Kleber, S., Dang, Y., Gülcüler Balta, G.S., Kalamakis, G., Göpferich, M., Ibañez, D.C., Schefzik, R., Lopez, A.S., Bobadilla, E.L., Schultz, C., Fischer, B. and Martin-Villalba, A. 2019. Onset of differentiation is post-transcriptionally controlled in adult neural stem cells. *Nature* 566(7742), pp. 100–104.
Batie, M., Frost, J., Frost, M., Wilson, J.W., Schofield, P. and Rocha, S. 2019. Hypoxia induces rapid changes to histone methylation and reprograms chromatin. *Science* 363(6432), pp. 1222–1226.
Benita, Y., Kikuchi, H., Smith, A.D., Zhang, M.Q., Chung, D.C. and Xavier, R.J. 2009. An integrative genomics approach identifies Hypoxia Inducible Factor-1 (HIF-1)-target genes that form the core response to hypoxia. *Nucleic Acids Research* 37(14), pp. 4587–4602.
Benjamin, J.S., Pilarowski, G.O., Carosso, G.A., Zhang, L., Huso, D.L., Goff, L.A., Vernon, H.J., Hansen, K.D. and Bjornsson, H.T. 2017. A ketogenic diet rescues hippocampal memory defects in a mouse model of Kabuki syndrome. *Proceedings of the National Academy of Sciences of the United States of America* 114(1), pp. 125–130.
Berg, D.A., Su, Y., Jimenez-Cyrus, D., Patel, A., Huang, N., Morizet, D., Lee, S., Shah, R., Ringeling, F.R., Jain, R., Epstein, J.A., Wu, Q.-F., Canzar, S., Ming, G.-L., Song, H. and Bond, A.M. 2019. A common embryonic origin of stem cells drives developmental and adult neurogenesis. *Cell* 177(3), p. 654–668.e15.
Bermejo, R., Lai, M.S. and Foiani, M. 2012. Preventing replication stress to maintain genome stability: resolving conflicts between replication and transcription. *Molecular Cell* 45(6), pp. 710–718.
Bernas, S., Leiter, O., Walker, T. and Kempermann, G. 2017. Isolation, culture and differentiation of adult hippocampal precursor cells. *Bio-protocol* 7(21).
Bjornsson, H.T. 2015. The Mendelian disorders of the epigenetic machinery. *Genome Research* 25(10), pp. 1473–1481.

Bjornsson, H.T., Benjamin, J.S., Zhang, L., Weissman, J., Gerber, E.E., Chen, Y.-C., Vaurio, R.G., Potter, M.C., Hansen, K.D. and Dietz, H.C. 2014. Histone deacetylase inhibition rescues structural and functional brain deficits in a mouse model of Kabuki syndrome. *Science Translational Medicine* 6(256), p. 256ra135.
Boisgontier, J., Tacchella, J.M., Lemaître, H., Lehman, N., Saitovitch, A., Gatinois, V., Boursier, G., Sanchez, E., Rechtman, E., Fillon, L., Lyonnet, S., Le Quang Sang, K.-H., Baujat, G., Rio, M., Boute, O., Faivre, L., Schaefer, E., Sanlaville, D., Zilbovicius, M., Grévent, D., Geneviève, D. and Boddaert, N. 2018. Anatomical and functional abnormalities on MRI in kabuki syndrome. *NeuroImage. Clinical*.
Carosso, G.A., Boukas, L., Augustin, J.J., Nguyen, H.N., Winer, B.L., Cannon, G.H., Robertson, J.D., Zhang, L., Hansen, K.D., Goff, L.A. and Bjornsson, H.T. 2019. Precocious neuronal differentiation and disrupted oxygen responses in Kabuki syndrome. *JCI Insight*.
Castonguay, Z., Auger, C., Thomas, S.C., Chahma, M. and Appanna, V.D. 2014. Nuclear lactate dehydrogenase modulates histone modification in human hepatocytes. *Biochemical and Biophysical Research Communications* 454(1), pp. 172–177.
Chakraborty, A.A., Laukka, T., Myllykoski, M., Ringel, A.E., Booker, M.A., Tolstorukov, M.Y., Meng, Y.J., Meier, S.R., Jennings, R.B., Creech, A.L., Herbert, Z.T., McBrayer, S.K., Olenchock, B.A., Jaffe, J.D., Haigis, M.C., Beroukhim, R., Signoretti, S., Koivunen, P. and Kaelin, W.G. 2019. Histone demethylase KDM6A directly senses oxygen to control chromatin and cell fate. *Science* 363(6432), pp. 1217–1222.
Chatzi, C., Schnell, E. and Westbrook, G.L. 2015. Localized hypoxia within the subgranular zone determines the early survival of newborn hippocampal granule cells. *eLife* 4, p. e08722.
Chen, Y., Sprung, R., Tang, Y., Ball, H., Sangras, B., Kim, S.C., Falck, J.R., Peng, J., Gu, W. and Zhao, Y. 2007. Lysine propionylation and butyrylation are novel post-translational modifications in histones. *Molecular & Cellular Proteomics* 6(5), pp. 812–819.
Clarke, K., Tchabanenko, K., Pawlosky, R., Carter, E., Todd King, M., Musa-Veloso, K., Ho, M., Roberts, A., Robertson, J., Vanitallie, T.B. and Veech, R.L. 2012. Kinetics, safety and tolerability of (R)-3-hydroxybutyl (R)-3-hydroxybutyrate in healthy adult subjects. *Regulatory Toxicology and Pharmacology* 63(3), pp. 401–408.
Courcet, J.-B., Faivre, L., Michot, C., Burguet, A., Perez-Martin, S., Alix, E., Amiel, J., Baumann, C., Cordier, M.-P., Cormier-Daire, V., Delrue, M.A., Gilbert-Dussardier, B., Goldenberg, A., Jacquemont, M.-L., Jaquette, A., Kayirangwa, H., Lacombe, D., Le Merrer, M., Toutain, A., Odent, S., Moncla, A., Pelet, A., Philip, N., Pinson, L., Poisson, S., Kim-Han, L.Q.S., Roume, J., Sanchez, E., Willems, M., Till, M., Vincent-Delorme, C., Mousson, C., Vinault, S., Binquet, C., Huet, F., Sarda, P., Salomon, R., Lyonnet, S., Sanlaville, D. and Geneviève, D. 2013. Clinical and molecular spectrum of renal malformations in Kabuki syndrome. *The Journal of Pediatrics* 163(3), pp. 742–746.
Danielson, N.B., Kaifosh, P., Zaremba, J.D., Lovett-Barron, M., Tsai, J., Denny, C.A., Balough, E.M., Goldberg, A.R., Drew, L.J., Hen, R., Losonczy, A. and Kheirbek, M.A. 2016. Distinct Contribution of Adult-Born Hippocampal Granule Cells to Context Encoding. *Neuron* 90(1), pp. 101–112.
Doetsch, F., Caillé, I., Lim, D.A., García-Verdugo, J.M. and Alvarez-Buylla, A. 1999. Subventricular zone astrocytes are neural stem cells in the adult mammalian brain. *Cell* 97(6), pp. 703–716.
During, M.J., Cao, L., Zuzga, D.S., Francis, J.S., Fitzsimons, H.L., Jiao, X., Bland, R.J., Klugmann, M., Banks, W.A., Drucker, D.J. and Haile, C.N. 2003. Glucagon-like peptide-1

receptor is involved in learning and neuroprotection. *Nature Medicine* 9(9), pp. 1173–1179.
Engstrom, A.K., Walker, A.C., Moudgal, R.A., Myrick, D.A., Kyle, S.M. and Katz, D.J. 2019. Pathological tau induces neurodegeneration by sequestering and inhibiting LSD1. *BioRxiv*.
Ervin, D.A. and Merrick, J. 2014. Intellectual and developmental disability: healthcare financing. *Frontiers in public health* 2, p. 160.
Fernandez-Capetillo, O., Chen, H.-T., Celeste, A., Ward, I., Romanienko, P.J., Morales, J.C., Naka, K., Xia, Z., Camerini-Otero, R.D., Motoyama, N., Carpenter, P.B., Bonner, W.M., Chen, J. and Nussenzweig, A. 2002. DNA damage-induced G2-M checkpoint activation by histone H2AX and 53BP1. *Nature Cell Biology* 4(12), pp. 993–997.
Fragkos, M., Jurvansuu, J. and Beard, P. 2009. H2AX is required for cell cycle arrest via the p53/p21 pathway. *Molecular and Cellular Biology* 29(10), pp. 2828–2840.
Freeman, J.M., Vining, E.P., Pillas, D.J., Pyzik, P.L., Casey, J.C. and Kelly, L.M. 1998. The efficacy of the ketogenic diet-1998: a prospective evaluation of intervention in 150 children. *Pediatrics* 102(6), pp. 1358–1363.
Froimchuk, E., Jang, Y. and Ge, K. 2017. Histone H3 lysine 4 methyltransferase KMT2D. *Gene* 627, pp. 337–342.
Garthe, A. and Kempermann, G. 2013. An old test for new neurons: refining the Morris water maze to study the functional relevance of adult hippocampal neurogenesis. *Frontiers in Neuroscience* 7, p. 63.
Ge, S., Yang, C.-H., Hsu, K.-S., Ming, G.-L. and Song, H. 2007. A critical period for enhanced synaptic plasticity in newly generated neurons of the adult brain. *Neuron* 54(4), pp. 559–566.
Gentleman, R.C., Carey, V.J., Bates, D.M., Bolstad, B., Dettling, M., Dudoit, S., Ellis, B., Gautier, L., Ge, Y., Gentry, J., Hornik, K., Hothorn, T., Huber, W., Iacus, S., Irizarry, R., Leisch, F., Li, C., Maechler, M., Rossini, A.J., Sawitzki, G., Smith, C., Smyth, G., Tierney, L., Yang, J.Y.H. and Zhang, J. 2004. Bioconductor: open software development for computational biology and bioinformatics. *Genome Biology* 5(10), p. R80.
Giner, G. and Smyth, G.K. 2016. Statmod: probability calculations for the inverse Gaussian distribution. *arXiv preprint arXiv:1603.06687*.
Gonçalves, J.T., Schafer, S.T. and Gage, F.H. 2016. Adult neurogenesis in the hippocampus: from stem cells to behavior. *Cell* 167(4), pp. 897–914.
Göndör, A. and Ohlsson, R. 2009. Replication timing and epigenetic reprogramming of gene expression: a two-way relationship? *Nature Reviews. Genetics* 10(4), pp. 269–276.
Guimarães-Camboa, N., Stowe, J., Aneas, I., Sakabe, N., Cattaneo, P., Henderson, L., Kilberg, M.S., Johnson, R.S., Chen, J., McCulloch, A.D., Nobrega, M.A., Evans, S.M. and Zambon, A.C. 2015. Hif1α represses cell stress pathways to allow proliferation of hypoxic fetal cardiomyocytes. *Developmental Cell* 33(5), pp. 507–521.
Guo, C., Chang, C.-C., Wortham, M., Chen, L.H., Kernagis, D.N., Qin, X., Cho, Y.-W., Chi, J.-T., Grant, G.A., McLendon, R.E., Yan, H., Ge, K., Papadopoulos, N., Bigner, D.D. and He, Y. 2012. Global identification of MLL2-targeted loci reveals MLL2's role in diverse signaling pathways. *Proceedings of the National Academy of Sciences of the United States of America* 109(43), pp. 17603–17608.
Habib, N., Li, Y., Heidenreich, M., Swiech, L., Avraham-Davidi, I., Trombetta, J.J., Hession, C., Zhang, F. and Regev, A. 2016. Div-Seq: Single-nucleus RNA-Seq reveals dynamics of rare adult newborn neurons. *Science* 353(6302), pp. 925–928.
Hannibal, M.C., Buckingham, K.J., Ng, S.B., Ming, J.E., Beck, A.E., McMillin, M.J., Gildersleeve, H.I., Bigham, A.W., Tabor, H.K., Mefford, H.C., Cook, J., Yoshiura, K.,

Matsumoto, T., Matsumoto, N., Miyake, N., Tonoki, H., Naritomi, K., Kaname, T., Nagai, T., Ohashi, H., Kurosawa, K., Hou, J.-W., Ohta, T., Liang, D., Sudo, A., Morris, C.A., Banka, S., Black, G.C., Clayton-Smith, J., Nickerson, D.A., Zackai, E.H., Shaikh, T.H., Donnai, D., Niikawa, N., Shendure, J. and Bamshad, M.J. 2011. Spectrum of MLL2 (ALR) mutations in 110 cases of Kabuki syndrome. *American Journal of Medical Genetics. Part A* 155A(7), pp. 1511–1516.
Hasselbalch, S.G., Knudsen, G.M., Jakobsen, J., Hageman, L.P., Holm, S. and Paulson, O.B. 1995. Blood-brain barrier permeability of glucose and ketone bodies during short-term starvation in humans. *The American Journal of Physiology* 268(6 Pt 1), pp. E1161-6.
Hirabayashi, Y., Suzki, N., Tsuboi, M., Endo, T.A., Toyoda, T., Shinga, J., Koseki, H., Vidal, M. and Gotoh, Y. 2009. Polycomb limits the neurogenic competence of neural precursor cells to promote astrogenic fate transition. *Neuron* 63(5), pp. 600–613.
Huang, P.-H., Plass, C. and Chen, C.-S. 2011. Effects of Histone Deacetylase Inhibitors on Modulating H3K4 Methylation Marks - A Novel Cross-Talk Mechanism between Histone-Modifying Enzymes. *Molecular and cellular pharmacology* 3(2), pp. 39–43.
Huber, W., Carey, V.J., Gentleman, R., Anders, S., Carlson, M., Carvalho, B.S., Bravo, H.C., Davis, S., Gatto, L., Girke, T., Gottardo, R., Hahne, F., Hansen, K.D., Irizarry, R.A., Lawrence, M., Love, M.I., MacDonald, J., Obenchain, V., Oleś, A.K., Pagès, H., Reyes, A., Shannon, P., Smyth, G.K., Tenenbaum, D., Waldron, L. and Morgan, M. 2015. Orchestrating high-throughput genomic analysis with Bioconductor. *Nature Methods* 12(2), pp. 115–121.
Hurt, J.A., Robertson, A.D. and Burge, C.B. 2013. Global analyses of UPF1 binding and function reveal expanded scope of nonsense-mediated mRNA decay. *Genome Research* 23(10), pp. 1636–1650.
Irizarry, R.A., Bolstad, B.M., Collin, F., Cope, L.M., Hobbs, B. and Speed, T.P. 2003. Summaries of Affymetrix GeneChip probe level data. *Nucleic Acids Research* 31(4), p. e15.
Kantidakis, T., Saponaro, M., Mitter, R., Horswell, S., Kranz, A., Boeing, S., Aygün, O., Kelly, G.P., Matthews, N., Stewart, A., Stewart, A.F. and Svejstrup, J.Q. 2016. Mutation of cancer driver MLL2 results in transcription stress and genome instability. *Genes & Development* 30(4), pp. 408–420.
Kim, D., Langmead, B. and Salzberg, S.L. 2015. HISAT: a fast spliced aligner with low memory requirements. *Nature Methods* 12(4), pp. 357–360.
Kim, D.-H., Rhee, J.C., Yeo, S., Shen, R., Lee, S.-K., Lee, J.W. and Lee, S. 2015. Crucial roles of mixed-lineage leukemia 3 and 4 as epigenetic switches of the hepatic circadian clock controlling bile acid homeostasis in mice. *Hepatology* 61(3), pp. 1012–1023.
Kim, D.Y., Vallejo, J. and Rho, J.M. 2010. Ketones prevent synaptic dysfunction induced by mitochondrial respiratory complex inhibitors. *Journal of Neurochemistry* 114(1), pp. 130–141.
Kung, A.L., Rebel, V.I., Bronson, R.T., Ch'ng, L.E., Sieff, C.A., Livingston, D.M. and Yao, T.P. 2000. Gene dose-dependent control of hematopoiesis and hematologic tumor suppression by CBP. *Genes & Development* 14(3), pp. 272–277.
Kurdistani, S.K. 2014. Chromatin: a capacitor of acetate for integrated regulation of gene expression and cell physiology. *Current Opinion in Genetics & Development* 26, pp. 53–58.
Landt, S.G., Marinov, G.K., Kundaje, A., Kheradpour, P., Pauli, F., Batzoglou, S., Bernstein, B.E., Bickel, P., Brown, J.B., Cayting, P., Chen, Y., DeSalvo, G., Epstein, C., Fisher-Aylor, K.I., Euskirchen, G., Gerstein, M., Gertz, J., Hartemink, A.J., Hoffman, M.M., Iyer, V.R., Jung, Y.L., Karmakar, S., Kellis, M., Kharchenko, P.V., Li, Q., Liu, T., Liu, X.S., Ma, L., Milosavljevic, A., Myers, R.M., Park, P.J., Pazin, M.J., Perry, M.D., Raha, D., Reddy, T.E., Rozowsky, J., Shoresh,

N., Sidow, A., Slattery, M., Stamatoyannopoulos, J.A., Tolstorukov, M.Y., White, K.P., Xi, S., Farnham, P.J., Lieb, J.D., Wold, B.J. and Snyder, M. 2012. ChIP-seq guidelines and practices of the ENCODE and modENCODE consortia. *Genome Research* 22(9), pp. 1813–1831.
Langmead, B. and Salzberg, S.L. 2012. Fast gapped-read alignment with Bowtie 2. *Nature Methods* 9(4), pp. 357–359.
Lawrence, M., Huber, W., Pagès, H., Aboyoun, P., Carlson, M., Gentleman, R., Morgan, M.T. and Carey, V.J. 2013. Software for computing and annotating genomic ranges. *PLoS Computational Biology* 9(8), p. e1003118.
Lederer, D., Grisart, B., Digilio, M.C., Benoit, V., Crespin, M., Ghariani, S.C., Maystadt, I., Dallapiccola, B. and Verellen-Dumoulin, C. 2012. Deletion of KDM6A, a histone demethylase interacting with MLL2, in three patients with Kabuki syndrome. *American Journal of Human Genetics* 90(1), pp. 119–124.
Lee, J.-E., Wang, C., Xu, S., Cho, Y.-W., Wang, L., Feng, X., Baldridge, A., Sartorelli, V., Zhuang, L., Peng, W. and Ge, K. 2013. H3K4 mono- and di-methyltransferase MLL4 is required for enhancer activation during cell differentiation. *eLife* 2, p. e01503.
Lee, M.G., Wynder, C., Bochar, D.A., Hakimi, M.-A., Cooch, N. and Shiekhattar, R. 2006. Functional interplay between histone demethylase and deacetylase enzymes. *Molecular and Cellular Biology* 26(17), pp. 6395–6402.
Leek, J.T., Johnson, W.E., Parker, H.S., Jaffe, A.E. and Storey, J.D. 2012. The sva package for removing batch effects and other unwanted variation in high-throughput experiments. *Bioinformatics* 28(6), pp. 882–883.
Leek, J.T. and Storey, J.D. 2007. Capturing heterogeneity in gene expression studies by surrogate variable analysis. *PLoS Genetics* 3(9), pp. 1724–1735.
Leonard, H. and Wen, X. 2002. The epidemiology of mental retardation: challenges and opportunities in the new millennium. *Mental retardation and developmental disabilities research reviews* 8(3), pp. 117–134.
Li, W., Sun, W., Zhang, Y., Wei, W., Ambasudhan, R., Xia, P., Talantova, M., Lin, T., Kim, J., Wang, X., Kim, W.R., Lipton, S.A., Zhang, K. and Ding, S. 2011. Rapid induction and long-term self-renewal of primitive neural precursors from human embryonic stem cells by small molecule inhibitors. *Proceedings of the National Academy of Sciences of the United States of America* 108(20), pp. 8299–8304.
Li, Y., Aimone, J.B., Xu, X., Callaway, E.M. and Gage, F.H. 2012. Development of GABAergic inputs controls the contribution of maturing neurons to the adult hippocampal network. *Proceedings of the National Academy of Sciences of the United States of America* 109(11), pp. 4290–4295.
Liao, Y., Smyth, G.K. and Shi, W. 2019. The R package Rsubread is easier, faster, cheaper and better for alignment and quantification of RNA sequencing reads. *Nucleic Acids Research* 47(8), p. e47.
Lim, S., Chesser, A.S., Grima, J.C., Rappold, P.M., Blum, D., Przedborski, S. and Tieu, K. 2011. D-β-hydroxybutyrate is protective in mouse models of Huntington's disease. *Plos One* 6(9), p. e24620.
Lin-Shiao, E., Lan, Y., Coradin, M., Anderson, A., Donahue, G., Simpson, C.L., Sen, P., Saffie, R., Busino, L., Garcia, B.A., Berger, S.L. and Capell, B.C. 2018. KMT2D regulates p63 target enhancers to coordinate epithelial homeostasis. *Genes & Development* 32(2), pp. 181–193.
Love, M.I., Huber, W. and Anders, S. 2014. Moderated estimation of fold change and dispersion for RNA-seq data with DESeq2. *Genome Biology* 15(12), p. 550.

Lun, A.T.L., McCarthy, D.J. and Marioni, J.C. 2016. A step-by-step workflow for low-level analysis of single-cell RNA-seq data with Bioconductor. [version 2; peer review: 3 approved, 2 approved with reservations]. *F1000Research* 5, p. 2122.
Luo, W. and Wang, Y. 2018. Epigenetic regulators: multifunctional proteins modulating hypoxia-inducible factor-α protein stability and activity. *Cellular and Molecular Life Sciences* 75(6), pp. 1043–1056.
Mazumdar, J., O'Brien, W.T., Johnson, R.S., LaManna, J.C., Chavez, J.C., Klein, P.S. and Simon, M.C. 2010. O2 regulates stem cells through Wnt/β-catenin signalling. *Nature Cell Biology* 12(10), pp. 1007–1013.
McAvoy, K.M., Scobie, K.N., Berger, S., Russo, C., Guo, N., Decharatanachart, P., Vega-Ramirez, H., Miake-Lye, S., Whalen, M., Nelson, M., Bergami, M., Bartsch, D., Hen, R., Berninger, B. and Sahay, A. 2016. Modulating neuronal competition dynamics in the dentate gyrus to rejuvenate aging memory circuits. *Neuron* 91(6), pp. 1356–1373.
McCarthy, D.J., Chen, Y. and Smyth, G.K. 2012. Differential expression analysis of multifactor RNA-Seq experiments with respect to biological variation. *Nucleic Acids Research* 40(10), pp. 4288–4297.
McInnes, L., Healy, J., Saul, N. and Großberger, L. 2018. UMAP: uniform manifold approximation and projection. *The Journal of Open Source Software* 3(29), p. 861.
Ming, G.-L. and Song, H. 2011. Adult neurogenesis in the mammalian brain: significant answers and significant questions. *Neuron* 70(4), pp. 687–702.
Miyake, N., Mizuno, S., Okamoto, N., Ohashi, H., Shiina, M., Ogata, K., Tsurusaki, Y., Nakashima, M., Saitsu, H., Niikawa, N. and Matsumoto, N. 2013. KDM 6 A Point Mutations Cause K abuki Syndrome. *Human mutation* 34(1), pp. 108–110.
Moreno-Jiménez, E.P., Flor-García, M., Terreros-Roncal, J., Rábano, A., Cafini, F., Pallas-Bazarra, N., Ávila, J. and Llorens-Martín, M. 2019. Adult hippocampal neurogenesis is abundant in neurologically healthy subjects and drops sharply in patients with Alzheimer's disease. *Nature Medicine* 25(4), pp. 554–560.
Morimoto, B.H. and Koshland, D.E. 1990. Induction and expression of long- and short-term neurosecretory potentiation in a neural cell line. *Neuron* 5(6), pp. 875–880.
Morris, A.M., Churchwell, J.C., Kesner, R.P. and Gilbert, P.E. 2012. Selective lesions of the dentate gyrus produce disruptions in place learning for adjacent spatial locations. *Neurobiology of Learning and Memory* 97(3), pp. 326–331.
Mudge, J.M. and Harrow, J. 2015. Creating reference gene annotation for the mouse C57BL6/J genome assembly. *Mammalian Genome* 26(9–10), pp. 366–378.
Ng, S.B., Bigham, A.W., Buckingham, K.J., Hannibal, M.C., McMillin, M.J., Gildersleeve, H.I., Beck, A.E., Tabor, H.K., Cooper, G.M., Mefford, H.C., Lee, C., Turner, E.H., Smith, J.D., Rieder, M.J., Yoshiura, K.-I., Matsumoto, N., Ohta, T., Niikawa, N., Nickerson, D.A., Bamshad, M.J. and Shendure, J. 2010. Exome sequencing identifies MLL2 mutations as a cause of Kabuki syndrome. *Nature Genetics* 42(9), pp. 790–793.
Ortega-Molina, A., Boss, I.W., Canela, A., Pan, H., Jiang, Y., Zhao, C., Jiang, M., Hu, D., Agirre, X., Niesvizky, I., Lee, J.-E., Chen, H.-T., Ennishi, D., Scott, D.W., Mottok, A., Hother, C., Liu, S., Cao, X.-J., Tam, W., Shaknovich, R., Garcia, B.A., Gascoyne, R.D., Ge, K., Shilatifard, A., Elemento, O., Nussenzweig, A., Melnick, A.M. and Wendel, H.-G. 2015. The histone lysine methyltransferase KMT2D sustains a gene expression program that represses B cell lymphoma development. *Nature Medicine* 21(10), pp. 1199–1208.
Patro, R., Duggal, G., Love, M.I., Irizarry, R.A. and Kingsford, C. 2017. Salmon provides fast

and bias-aware quantification of transcript expression. *Nature Methods* 14(4), pp. 417–419.
Picelli, S., Björklund, Å.K., Faridani, O.R., Sagasser, S., Winberg, G. and Sandberg, R. 2013. Smart-seq2 for sensitive full-length transcriptome profiling in single cells. *Nature Methods* 10(11), pp. 1096–1098.
Pilaz, L.-J., McMahon, J.J., Miller, E.E., Lennox, A.L., Suzuki, A., Salmon, E. and Silver, D.L. 2016. Prolonged mitosis of neural progenitors alters cell fate in the developing brain. *Neuron* 89(1), pp. 83–99.
Rainer 2017. EnsDb.Mmusculus.v79: Ensembl based annotation package. *R package version 2.99.0.*
Ritchie, M.E., Phipson, B., Wu, D., Hu, Y., Law, C.W., Shi, W. and Smyth, G.K. 2015. limma powers differential expression analyses for RNA-sequencing and microarray studies. *Nucleic Acids Research* 43(7), p. e47.
Rizzardi, L.F., Hickey, P.F., Rodriguez DiBlasi, V., Tryggvadóttir, R., Callahan, C.M., Idrizi, A., Hansen, K.D. and Feinberg, A.P. 2019. Neuronal brain-region-specific DNA methylation and chromatin accessibility are associated with neuropsychiatric trait heritability. *Nature Neuroscience* 22(2), pp. 307–316.
Robinson, M.D., McCarthy, D.J. and Smyth, G.K. 2010. edgeR: a Bioconductor package for differential expression analysis of digital gene expression data. *Bioinformatics* 26(1), pp. 139–140.
Sahay, A., Scobie, K.N., Hill, A.S., O'Carroll, C.M., Kheirbek, M.A., Burghardt, N.S., Fenton, A.A., Dranovsky, A. and Hen, R. 2011. Increasing adult hippocampal neurogenesis is sufficient to improve pattern separation. *Nature* 472(7344), pp. 466–470.
Santos, A., Wernersson, R. and Jensen, L.J. 2015. Cyclebase 3.0: a multi-organism database on cell-cycle regulation and phenotypes. *Nucleic Acids Research* 43(Database issue), pp. D1140-4.
Sanz, J.H., Lipkin, P., Rosenbaum, K. and Mahone, E.M. 2010. Developmental profile and trajectory of neuropsychological skills in a child with Kabuki syndrome: implications for assessment of syndromes associated with intellectual disability. *The Clinical Neuropsychologist* 24(7), pp. 1181–1192.
Schuettengruber, B., Bourbon, H.-M., Di Croce, L. and Cavalli, G. 2017. Genome regulation by polycomb and trithorax: 70 years and counting. *Cell* 171(1), pp. 34–57.
Schuettengruber, B., Chourrout, D., Vervoort, M., Leblanc, B. and Cavalli, G. 2007. Genome regulation by polycomb and trithorax proteins. *Cell* 128(4), pp. 735–745.
Semenza, G.L. 2000. HIF-1: mediator of physiological and pathophysiological responses to hypoxia. *Journal of Applied Physiology* 88(4), pp. 1474–1480.
Shimazu, T., Hirschey, M.D., Newman, J., He, W., Shirakawa, K., Le Moan, N., Grueter, C.A., Lim, H., Saunders, L.R., Stevens, R.D., Newgard, C.B., Farese, R.V., de Cabo, R., Ulrich, S., Akassoglou, K. and Verdin, E. 2013. Suppression of oxidative stress by β-hydroxybutyrate, an endogenous histone deacetylase inhibitor. *Science* 339(6116), pp. 211–214.
Sleiman, S.F., Henry, J., Al-Haddad, R., El Hayek, L., Abou Haidar, E., Stringer, T., Ulja, D., Karuppagounder, S.S., Holson, E.B., Ratan, R.R., Ninan, I. and Chao, M.V. 2016. Exercise promotes the expression of brain derived neurotrophic factor (BDNF) through the action of the ketone body β-hydroxybutyrate. *eLife* 5.
Snyder, J.S. 2019. Recalibrating the relevance of adult neurogenesis. *Trends in Neurosciences* 42(3), pp. 164–178.
Soneson, C., Love, M.I. and Robinson, M.D. 2015. Differential analyses for RNA-seq: transcript-level estimates improve gene-level inferences. [version 2; peer review: 2 approved].

F1000Research 4, p. 1521.
Song, J., Sun, J., Moss, J., Wen, Z., Sun, G.J., Hsu, D., Zhong, C., Davoudi, H., Christian, K.M., Toni, N., Ming, G.-L. and Song, H. 2013. Parvalbumin interneurons mediate neuronal circuitry-neurogenesis coupling in the adult hippocampus. *Nature Neuroscience* 16(12), pp. 1728–1730.
Sorrells, S.F., Paredes, M.F., Cebrian-Silla, A., Sandoval, K., Qi, D., Kelley, K.W., James, D., Mayer, S., Chang, J., Auguste, K.I., Chang, E.F., Gutierrez, A.J., Kriegstein, A.R., Mathern, G.W., Oldham, M.C., Huang, E.J., Garcia-Verdugo, J.M., Yang, Z. and Alvarez-Buylla, A. 2018. Human hippocampal neurogenesis drops sharply in children to undetectable levels in adults. *Nature* 555(7696), pp. 377–381.
Swigut, T. and Wysocka, J. 2007. H3K27 demethylases, at long last. *Cell* 131(1), pp. 29–32.
Tang, G.-B., Zeng, Y.-Q., Liu, P.-P., Mi, T.-W., Zhang, S.-F., Dai, S.-K., Tang, Q.-Y., Yang, L., Xu, Y.-J., Yan, H.-L., Du, H.-Z., Teng, Z.-Q., Zhou, F.-Q. and Liu, C.-M. 2017. The histone H3K27 demethylase UTX regulates synaptic plasticity and cognitive behaviors in mice. *Frontiers in Molecular Neuroscience* 10, p. 267.
Tobin, M.K., Musaraca, K., Disouky, A., Shetti, A., Bheri, A., Honer, W.G., Kim, N., Dawe, R.J., Bennett, D.A., Arfanakis, K. and Lazarov, O. 2019. Human hippocampal neurogenesis persists in aged adults and alzheimer's disease patients. *Cell Stem Cell* 24(6), p. 974–982.e3.
Tozuka, Y., Fukuda, S., Namba, T., Seki, T. and Hisatsune, T. 2005. GABAergic excitation promotes neuronal differentiation in adult hippocampal progenitor cells. *Neuron* 47(6), pp. 803–815.
Trapnell, C., Cacchiarelli, D., Grimsby, J., Pokharel, P., Li, S., Morse, M., Lennon, N.J., Livak, K.J., Mikkelsen, T.S. and Rinn, J.L. 2014. The dynamics and regulators of cell fate decisions are revealed by pseudotemporal ordering of single cells. *Nature Biotechnology* 32(4), pp. 381–386.
Trapnell, C., Roberts, A., Goff, L., Pertea, G., Kim, D., Kelley, D.R., Pimentel, H., Salzberg, S.L., Rinn, J.L. and Pachter, L. 2012. Differential gene and transcript expression analysis of RNA-seq experiments with TopHat and Cufflinks. *Nature Protocols* 7(3), pp. 562–578.
Vissers, L.E.L.M., Gilissen, C. and Veltman, J.A. 2016. Genetic studies in intellectual disability and related disorders. *Nature Reviews. Genetics* 17(1), pp. 9–18.
Wang, J., Vasaikar, S., Shi, Z., Greer, M. and Zhang, B. 2017. WebGestalt 2017: a more comprehensive, powerful, flexible and interactive gene set enrichment analysis toolkit. *Nucleic Acids Research* 45(W1), pp. W130–W137.
Wang, S.-P., Tang, Z., Chen, C.-W., Shimada, M., Koche, R.P., Wang, L.-H., Nakadai, T., Chramiec, A., Krivtsov, A.V., Armstrong, S.A. and Roeder, R.G. 2017. A UTX-MLL4-p300 Transcriptional Regulatory Network Coordinately Shapes Active Enhancer Landscapes for Eliciting Transcription. *Molecular Cell* 67(2), p. 308–321.e6.
Welstead, G.G., Creyghton, M.P., Bilodeau, S., Cheng, A.W., Markoulaki, S., Young, R.A. and Jaenisch, R. 2012. X-linked H3K27me3 demethylase Utx is required for embryonic development in a sex-specific manner. *Proceedings of the National Academy of Sciences of the United States of America* 109(32), pp. 13004–13009.
Wen, Z., Nguyen, H.N., Guo, Z., Lalli, M.A., Wang, X., Su, Y., Kim, N.-S., Yoon, K.-J., Shin, J., Zhang, C., Makri, G., Nauen, D., Yu, H., Guzman, E., Chiang, C.-H., Yoritomo, N., Kaibuchi, K., Zou, J., Christian, K.M., Cheng, L., Ross, C.A., Margolis, R.L., Chen, G., Kosik, K.S., Song, H. and Ming, G. 2014. Synaptic dysregulation in a human iPS cell model of mental disorders. *Nature* 515(7527), pp. 414–418.
Zhang, J., Dominguez-Sola, D., Hussein, S., Lee, J.-E., Holmes, A.B., Bansal, M., Vlasevska, S., Mo, T., Tang, H., Basso, K., Ge, K., Dalla-Favera, R. and Pasqualucci, L. 2015. Disruption of

KMT2D perturbs germinal center B cell development and promotes lymphomagenesis. *Nature Medicine* 21(10), pp. 1190–1198.
Zhang, Y., Liu, T., Meyer, C.A., Eeckhoute, J., Johnson, D.S., Bernstein, B.E., Nusbaum, C., Myers, R.M., Brown, M., Li, W. and Liu, X.S. 2008. Model-based analysis of ChIP-Seq (MACS). *Genome Biology* 9(9), p. R137.
Zheng, X., Boyer, L., Jin, M., Mertens, J., Kim, Y., Ma, L., Ma, L., Hamm, M., Gage, F.H. and Hunter, T. 2016. Metabolic reprogramming during neuronal differentiation from aerobic glycolysis to neuronal oxidative phosphorylation. *eLife* 5.
Zhu, L.-L., Zhao, T., huang, X., Liu, Z., Wu, L., Wu, K. and Fan, M. 2011. Gene expression profiles and metabolic changes in embryonic neural progenitor cells under low oxygen. *Cellular reprogramming* 13(2), pp. 113–120.
Zhuo, J.-M., Tseng, H.-A., Desai, M., Bucklin, M.E., Mohammed, A.I., Robinson, N.T., Boyden, E.S., Rangel, L.M., Jasanoff, A.P., Gritton, H.J. and Han, X. 2016. Young adult born neurons enhance hippocampal dependent performance via influences on bilateral networks. *eLife* 5.

CURRICULUM VITAE

Giovanni A. Carosso

@gcarosso giovannicarosso

Predoctoral Training Program in Human Genetics
McKusick-Nathans Institute of Genetic Medicine
Johns Hopkins University School of Medicine
gcaross1@jhmi.edu

Edward D. Miller Research Building, 426
733 N Broadway
Baltimore, MD 21205
(+1) 703-850-4272

EDUCATION

2019
Johns Hopkins University School of Medicine, Baltimore, MD
Ph.D., Human Genetics & Molecular Biology
Thesis: "New insights into the basis of neurogenesis defects in Kabuki syndrome"
Advisor: Hans T. Bjornsson, M.D., Ph.D.
Committee: Hal Dietz, M.D. (Chair), David Valle, M.D., Loyal Goff, Ph.D., Winston Timp, Ph.D., Hongjun Song, Ph.D.

2010
University of California, Santa Barbara, Santa Barbara, CA
B.Sc., Biopsychology, Department of Psychological & Brain Sciences
UCSB Alpine Racing Team

RESEARCH

2013-2019
Ph.D. Candidate, Johns Hopkins University School of Medicine, Baltimore, MD
-Drove a 4-lab, multi-omics project in epigenetic target discovery toward reversal of intellectual disability in Kabuki syndrome, discovering novel roles for chromatin modifier KMT2D in neural differentiation: specifically, molecular defects in oxygen response mediating adult hippocampal neurogenesis.
-Executed project end-to-end from conception to experimentation, iteration, data analysis, and publication.
-Co-wrote a successfully funded grant award of $150K from NASA (1st year rotation).
-Developed, instructed, and published STEM education reforms for college-aged youth in Bolivia.

2010-2013
Research Assistant, Children's National Medical Center, Washington, D.C.
Center for Genetic Medicine Research, Children's Research Institute

-Performed critical experiments in discovery of causal *POLR3A* mutations in pediatric leukodystrophy.
-Curated an international leukodystrophy patient bio-registry and transgenic mouse models.
-Invited Member, Children's National CEO Connection Coalition

2007-2010
Undergraduate Research Assistant, University of California, Santa Barbara, CA
Behavioral Pharmacology Laboratory, Department of Psychological & Brain Sciences
-Characterized neuroadaptations in the mesolimbic reward pathway in animal models of compulsive stimulant abuse, finding progressive changes in glutamate and dopamine function in the medial prefrontal cortex.

TECHNICAL
Computational: R-based statistical programming and analysis of RNA-seq, ChIP-seq, scRNA-seq, exome; quantitative fluorescence imaging and cytometry (Imaris, Zen, FIJI, FlowJo).

Wet lab (*in vitro*): vector-based cellular reprogramming/patient-derived iPSCs and neural differentiation; CRISPR-Cas9; adult neural stem cell isolation and culture; immunofluorescence and confocal microscopy; flow cytometry; patient bio-registries; library preparation for scRNA-seq, RNA-seq, ChIP-seq.

Animal models (*in vivo*): mouse & rat behavioral phenotyping; stereotaxic surgery and jugular catheterization; operant conditioning chambers; drug trials and tissue preparation.
Articulation: scientific writing; data visualization; multi-lab team management; public speaking; teaching.

TEACHING
2017-present
Clubes de Ciencia Bolivia, Santa Cruz de la Sierra, Bolivia
"Neurociencia Regenerativa"
-As Instructor, designed & taught intensive 5-day/40-hour laboratory courses in neuroscience to university students in Spanish. Consistently among top-requested courses.
-Secured funding via competitive grant awards.
-Published low-cost, scalable STEM education techniques in *Nature* family journals.
2015
Johns Hopkins University School of Medicine, Baltimore, MD
"Pathobiology: Basic Mechanisms of Disease, CNS Anatomy & Physiology"
As TA, delivered graduate-level lectures on CNS disorders to JHU SoM students.

LANGUAGES

English, Italian (native); French, Spanish (professional working proficiency)
Le Grand Concours, National French Contest of the American Association of Teachers of French
- National Rank 6th (gold medal), 95th percentile, 2006
- National Rank 11th (silver medal), 90th percentile, 2005
- National Rank 4th (gold medal), 95th percentile, 2004

FUNDING

2019
-Global Advocacy Initiative Seed Grant, International Brain Research Organization (IBRO), € 2,700 in support of Regenerative Neuroscience course for Clubes de Ciencia Bolivia.
-Mindfire Foundation, Davos, Switzerland; € 2,000 awarded in support of neurobiology-based insights for development of artificial general intelligence (AGI) systems by Swiss non-profit Mindfire Global.

2017
-Graduate Student Association Travel Award, Johns Hopkins University School of Medicine; in support of international conference presentations.

2014
-National Aeronautics and Space Administration (NASA), NNJ13ZSA002N-TWINS "Comprehensive whole genome analysis of differential epigenetic effects of space travel on monozygotic twins." Proposed, designed, and co-written with P.I. Andrew P. Feinberg, M.D., M.P.H. One of 10 awards forming the International Space Station Twins Study Consortium under $1.5M grant.

WORKSHOPS

2016
Practical Genomics: From Biology to Statistics; 16-18 August, Johns Hopkins Center for Computational Genomics; Baltimore, MD. Unix- and R-based analysis of ChIP-seq and RNA-seq datasets.

2014
National Institutes of Health: High-Risk, High-Reward Research Symposium; 15-17 November, Bethesda, MD.

55th Annual Short Course on Medical and Experimental Mammalian Genetics; 20 July - 1 August, The Jackson Laboratory, Bar Harbor, ME. Two-week survey in heredity, disease, molecular genetics, and ethics in diagnosis and treatment of inherited disorders, co-sponsored by JAX Labs and JHU.

1st Twins Investigators' Working Group Meeting; 2-3 April, NASA Johnson Space Center, Houston, TX.

-Developed initial protocols for in-flight biological sampling aboard the ISS, ground-based experiments, data analysis, publication/attribution, and genetic privacy authorizations for astronauts Scott and Mark Kelly during Scott's year aboard the International Space Station.

TALKS

2019

Gordon Research Seminar, Dynamics of Epigenetic Regulation: Mechanisms and Beyond; Holderness, NH.
Discussion Leader, session "Regulation of Dynamic DNA/RNA Methylation."

Johns Hopkins Chromatin and Chromosomes Workshop; 20 May, Johns Hopkins University, Baltimore, MD. "Precocious neuronal differentiation and disrupted hypoxia responses in Kabuki syndrome."

Simposio CdeCBo; 8 January, Santa Cruz de la Sierra, Bolivia
"Mar para Bolivia" discussing genomic profiling of marine biodiversity by Project Ocean Watch, hosted by Cámara de la Industria, Comercio, Turismo y Desarrollo (CAINCO).

2018

Conéctate Con el Mundo; 8 January, Santa Cruz de la Sierra, Bolivia
"Regeneración en el Cerebro" on adult neurogenesis and developmental syndromes, hosted by Cámara de la Industria, Comercio, Turismo y Desarrollo (CAINCO).

COMPETITIONS

2014

Yale Graduate Student Consulting Club Case Competition, 4 April, New Haven, CT
Competed among 27 teams from Yale, Harvard, Johns Hopkins, and Duke in developing real-world business strategy for Dish Network Corp. in response to pending merger between Comcast and Time Warner Cable. Group Rank: Overall: 2nd; Logic: 3rd; Analysis: 1st; Presentation: 2nd

PUBLICATIONS

Carosso, G.A., Boukas, L., Augustin, J.J., Nguyen, H.N., Winer, B.L., Cannon, G.H., Robertson, J.D., Zhang, L., Hansen, K.D., Goff, L.A. and Bjornsson, H.T., 2019. Precocious neuronal differentiation and disrupted oxygen responses in Kabuki syndrome. *JCI Insight*, 4(20).

Carosso, G.A., Ferreira, L.M., Mostajo Radji, M.A. 2019. Scientists as Non-State Actors of Public Diplomacy. *Nature Human Behaviour*, 1(2).

Carosso, G.A., Ferreira, L.M., Mostajo Radji, M.A. 2019. Developing brains, developing nations. *Frontiers in Education,* 4(95).

Ferreira, L.M., **Carosso, G.A.**, Lopez-Videla, B., Diez, G.V., Rivera-Betancourt, L.I., Rodriguez, Y., Ordonez, D.G., Duran, N.M., Alatriste-Gonzalez, D.K., Vacaflores, A., Bohorquez, S., Gonzalez Auza, L., Schuetz, C., Alexander-Savino, C., Gandarilla Cuellar, O., Mostajo Radji, M.A., 2019. Effective participatory science education in a diverse Latin American population. *Palgrave Communications*, 5(1), p.11.

Benjamin, J.S., Pilarowski, G.O., **Carosso, G.A.**, Zhang, L., Huso, D.L., Goff, L.A., Vernon, H.J., Hansen, K.D. and Bjornsson, H.T., 2017. A ketogenic diet rescues hippocampal memory defects in a mouse model of Kabuki syndrome. *Proceedings of the National Academy of Sciences*, 114(1), pp.125-130.

Vanderver, A., Tonduti, D., Bernard, G., Lai, J., Rossi, C., **Carosso, G.A.**, Quezado, M., Wong, K. and Schiffmann, R., 2013. More than hypomyelination in Pol-III disorder. *Journal of Neuropathology & Experimental Neurology*, 72(1), pp.67-75.

Ben-Shahar, O. M., Szumlinski, K. K., Lominac, K. D., Cohen, A., Gordon, E., Ploense, K. L., DeMartini, J., Bernstein, N., Rudy, N. M., Nabhan, A. N., Sacramento, A., Pagano, K., **Carosso, G.A.**, and Woodward, N., 2012. Extended access to cocaine self-administration results in reduced glutamate function within the medial prefrontal cortex. *Addiction Biology*, 17: 746–757.

Bernard, G., Chouery, E., Putorti, M.L., Tétreault, M., Takanohashi, A., **Carosso, G.A.**, Clément, I., Boespflug-Tanguy, O., Rodriguez, D., Delague, V. and Ghoch, J.A., 2011. Mutations of POLR3A encoding a catalytic subunit of RNA polymerase Pol III cause a recessive hypomyelinating leukodystrophy. *The American Journal of Human Genetics*, 89(3), pp.415-423.

CONFERENCE PRESENTATIONS

2019

Gordon Research Conference, Epigenetics; 21-26 July, Holderness, NH.
Carosso, G.A., Boukas, L., Augustin, J.J., Nguyen, H.N., Winer, B.L., Cannon, G.H., Robertson, J.D., Zhang, L., Hansen, K.D., Goff, L.A. and Bjornsson, H.T. "Precocious neuronal differentiation and disrupted oxygen responses in Kabuki syndrome."

Johns Hopkins Chromatin and Chromosomes Workshop; 20 May, Johns Hopkins University, Baltimore, MD.
Carosso, G.A., Boukas, L., Augustin, J.J., Nguyen, H.N., Winer, B.L., Cannon, G.H., Robertson, J.D., Zhang, L., Hansen, K.D., Goff, L.A. and Bjornsson, H.T. "Precocious neuronal differentiation and disrupted oxygen responses in Kabuki syndrome."

2018
Maryland Technology Development Corporation (TEDCO) Entrepreneur Expo & Stem Cell Symposium, 30 October, College Park, MD.
Carosso, G.A., Boukas, L., Augustin, J.J., Nguyen, H.N., Winer, B.L., Cannon, G.H., Robertson, J.D., Zhang, L., Hansen, K.D., Goff, L.A. and Bjornsson, H.T. "Transcriptional suppression upon KMT2D loss in patient-derived neural stem cells and mouse models of neurodevelopment"

2017
American Society of Human Genetics, 17-21 October, Orlando, FL .
Goff L.A., **Carosso, G.A.** et al. (**Plenary Session**) "Cell-type-specific responses in genetic disorders: Single cell reconstruction of neurogenesis defects in Kabuki syndrome 1"

EMBO: Gene Regulatory Mechanisms of Neural Fate Decisions, 7-10 September, Alicante, Spain
Carosso, G.A., Weissman, JR, Cannon, GH, Zhang, L, Goff, L.A., Bjornsson, H.T. "Divergent trajectories of adult neurogenesis in Kabuki syndrome"

EMBO: Advances in Stem Cells and Regenerative Medicine, 23-26 May, Heidelberg, Germany
Carosso, G.A., Weissman, JR, Cannon, GH, Zhang, L, Goff, L.A., Bjornsson, H.T. "Divergent trajectories of adult neurogenesis in Kabuki syndrome"

Cortical Development: Neural Stem Cells to Neural Circuits, 17-20 May, Chaniá, Crete, Greece
Carosso, G.A., Weissman, JR, Cannon, GH, Zhang, L, Goff, L.A., Bjornsson, H.T. "Divergent trajectories of adult neurogenesis in Kabuki syndrome"

2016
American Society of Human Genetics, 18-22 October, Vancouver, British Columbia, Canada
Carosso, G.A., Weissman, JR, Cannon, GH, Zhang, L, Goff, L.A., Bjornsson, H.T. "Defects of adult hippocampal neurogenesis unify genetically distinct forms of Kabuki syndrome"

2012
American Society of Human Genetics, 6-10 November, San Francisco, CA
Vanderver, A., Schmidt, J., **Carosso, G.A.**, Tonduti, D. Bernard, G., Lai, J., Rossi, C., Quezado, M., Wong, K., Schiffmann, R. "Neuropathology in POL-III related disorders: Myelin loss in 4H syndrome"

Children's National Research Week, 24-28 April, Washington, D.C.
Carosso, G.A., Bernard, G., Takanohashi, A., Rossi, C., Schiffman, R., Quezado, M., Vanderver, A. "Immune Pathology in 4H Syndrome (hypomyelination with hypogonadotropic hypogonadism and hypodontia)"

American Society for Neurochemistry, 3-7 March, Baltimore, MD
Carosso, G.A., Bernard, G., Takanohashi, A., Rossi, C., Schiffman, R., Quezado, M., Vanderver, A. "Type-I interferon mechanisms in the RNA polymerase III (PolIII)-related hypomyelinating disorder 4H Syndrome"

2011
Society for Neuroscience, 12-16 November, Washington, D.C.
Carosso, G.A., Bernard, G., Takanohashi, A., Rossi, C., Schiffman, R., Quezado, M., Vanderver, A. "Immune Pathology in 4H Syndrome (hypomyelination with hypogonadotropic hypogonadism and hypodontia)"

American Society of Human Genetics, 11-15 October, Montreal, Canada
Bernard, G., Chouery, E., Putorti, M.L., Tétreault, M., Takanohashi, A., **Carosso, G.A.**, Clément, I., Choquet, K., Fribourg, S., Teichmann, M., Megarbane, A., Schiffmann, R., Vanderver, A., Brais, B. "Tremor-Ataxia with Central Hypomyelination (TACH), leukodystrophy with oligodontia (LO) and 4H syndrome (hypomyelinating leukodystrophy with hypodontia and hypogonadotropic hypogonadism) are allelic disorders caused by mutations in the same gene"

American College of Medical Genetics, 16-20 March, Vancouver, British Columbia, Canada
Prust, M., Loewenstein, J., **Carosso, G.A.**, Vanderver, A. "The Myelin Disorders Bioregistry Project"

2008
Society for Neuroscience, 15-19 November, Washington, D.C.
Ben-Shahar, O., Szumlinski, K., Lominac, K., Cohen, A., Gordon, E., Ploense, K., DeMartini, J., Bernstein, N., Rudy, N., Nabhan, A., Sacramento, A., Pagano, K., **Carosso, G.A.**, Woodward, N. "Extended access to cocaine self-administration results in reduced glutamate function within the medial prefrontal cortex"